Transport mechanisms of bacterial membrane proteins analyzed by advanced fluorescence microscopy

Dissertation
zur
Erlangung des Doktorgrades (Dr. rer. nat.)
der
Mathematisch-Naturwissenschaftlichen Fakultät
der
Rheinischen Friedrich-Wilhelms-Universität Bonn

vorgelegt von
Annika Marie Krüger
aus
Bonn

Bonn
2026

Angefertigt mit Genehmigung der Mathematisch-Naturwissenschaftlichen Fakultät
der Rheinischen Friedrich-Wilhelms-Universität Bonn

Gutachter/Betreuer: Prof. Dr. Ulrich Kubitscheck
Gutachter: PD Dr. Gregor Hagelüken

Tag der Promotion: 26.06.2026
Erscheinungsjahr: 2026

Acknowledgements

First, I want to thank my supervisor Prof. Dr. Ulrich Kubitscheck. I am extremely thankful for the trust and encouragement he offered throughout the years. His scientific insight and willingness to discuss my, sometimes very ambitious, ideas have shaped not only this thesis but also the way I think as a scientist. I am immensely grateful for having such a supportive supervisor who allowed me to find and define my own path.
I would also like to thank my second examiner and collaboration partner Dr. Gregor Hagelüken for providing his generous support and extensive expertise throughout this project. I deeply appreciate the time he invested in our discussions and the supportive way in which he helped to guide this project forward.
Thank you very much to Prof. Dr. Arne Lützen and Prof. Dr. Jonathan Schmid-Burgk for agreeing to be a part of my doctoral committee.

I would also like to sincerely thank Dr. Jan Peter Siebrasse, whose support and expertise have been immensely important throughout my PhD. I would also like to apologize for scaring him on multiple occasions when I came into his office to ask questions and discuss my ideas with him.
Next, I would like to thank Philipp Hendricks for purifying the TRAP transporter proteins and several mutants. Also, I would like to thank him for teaching me his methods, when our confocal microscope broke down.
I also want to thank Prof. Dr. Tanja Schneider and Dr. Anna Müller who provided materials and their invaluable expertise. Thank you to Mara Bingel for providing the purified proteins for the MurJ project.
To my colleagues, past and present: I am beyond grateful for being lucky enough to have had you next to me every step of the way. I always knew that I could count on you in tough times. Thank you for the laughter, the coffees, the conversations, and the constant encouragement.

Last but not least, I would like to thank my parents who always taught me that I could do anything I would set my mind to. And although this has brought quite some challenges with it (evidence no. 1: this thesis): I am beyond grateful for you believing in me.
Finally, I would also like to thank my boyfriend for his unwavering support and his patience when the thesis stress got to me. You're the calm to my storm.

Abstract

Transporter proteins are integral membrane proteins and enable the translocation of hydro- or amphiphilic substrates over cell membranes. This study focuses on two such systems: The lipid II flippase and the tripartite adensosine triphosphate (ATP)-independent periplasmic (TRAP) transporters.
The lipid II flippase is essential for cell wall synthesis in bacteria, as this protein mediates the translocation of the cell wall precursor lipid II from cyto- to periplasm. However, the exact identity of this protein remains a topic of discussion.
TRAP transporters scavenge and import substrates from host cells and, thereby, contribute to the virulence of different pathogens. These transporters consist of a substrate binding protein (SBP), also called P-domain, and two transmembrane domains (Q- and M-domain). The SBP diffuses freely in the bacterial periplasm and delivers the substrate to the transmembrane domains.
The complexity of biological membranes makes it difficult to study single proteins, however, membrane proteins need to be in hydrophobic environments to be active. Therefore, advanced fluorescence microscopy was used to investigate both processes in artificial membranes. To this end, a modified formation pathway for giant unilamellar vesicles (GUVs) was developed, which enabled a high GUV yield in physiological salt concentration (∼150 mM total monovalent ions) solutions while allowing a simultaneous reconstitution of membrane proteins. Subsequently, GUVs and large unilamellar vesicles (LUVs) were characterized as model systems.
The putative lipid II flippases MurJ, RodA and FtsW from *Staphylococcus aureus* (Sa) were tested for their lipid II flipping activity in presence and absence of a membrane potential. MurJ was found to exhibit lipid II flipping, in contrast to the other tested proteins. MurJ's activity was increased in presence of a membrane potential.
Sialic acid import by SiaPQM from *Haemophilus influenzae* (Hi) was visualized in alternating-laser excitation (ALEX) single-molecule (sm) Förster resonance energy transfer (FRET) measurements as well as in ensemble FRET measurements. Both import assays revealed that the SBP is strictly required for successful import. Furthemore, a sodium gradient proved to be essential as a driving force for the import. If no sodium was present, binding between HiSiaP and HiSiaQM was attenuated. Finally, important regions in HiSiaPQM were identified that were necessary for substrate import. One of these regions was a periplasmic loop of HiSiaQM which could potentially be utilized to trigger a "push-to-release"-mechanism in HiSiaP, mediating successful substrate transfer.

Contents

1 Introduction **1**

1.1 Membrane model systems . . . 3

1.1.1 Spherical model systems . . . 3

1.1.2 Membrane protein reconstitution . . . 5

1.2 Transporter proteins . . . 7

1.2.1 Lipid II flippase . . . 8

1.2.2 Tripartite ATP-independent periplasmic transporters . . . 12

1.3 Motivation . . . 15

2 Results **16**

2.1 Modification and characterization of membrane model systems . . . 16

2.1.1 Giant unilamellar vesicles . . . 16

2.1.2 Large unilamellar vesicles . . . 27

2.1.3 Vesicle fusion . . . 33

2.2 Construction of a two-color smFRET microscope from a single-channel setup . . . 36

2.2.1 FRET evaluation . . . 37

2.2.2 smFRET control measurements . . . 38

2.3 Functional analysis of membrane transporter proteins . . . 41

2.3.1 The Lipid II flippase . . . 41

2.3.2 TRAP transporters . . . 45

3 Discussion **67**

3.1 Model system optimization and characterization . . . 67

3.1.1 Giant unilamellar vesicles . . . 67

3.1.2 Large unilamellar vesicles . . . 68

3.2 The lipid II flippase . . . 69

3.2.1 MurJ shows lipid II flipping activity . . . 70

3.3 TRAP transporters . . . 72

3.3.1 Two FRET sensors can detect Neu5Ac . . . 72

3.3.2 HiSiaP-QM complex formation . . . 73

3.3.3 Neu5Ac import can be visualized via ALEX smFRET . . . 74

3.3.4 Neu5Ac import can be observed via ensemble FRET in GUVs . . . 75

4 Conclusion and Outlook **81**

5 Materials **83**

5.1 Chemicals . . . 83

5.2 Instruments and optical devices . . . 85

5.3 Special laboratory consumables 86
5.4 Software 86

6 Methods **87**
6.1 Detergent-mediated proteo-GUV swelling 87
6.2 LUV preparation via lipid film hydration and extrusion 87
6.3 LUV immobilization via BioBSA-NAv 88
6.4 LUV immobilization via agarose 88
6.5 Dithionite quenching assay 88
6.6 Membrane potential establishment and measurement 90
6.7 Dynamic light scattering 90
6.8 Preparation of positively charged LUVs for vesicle fusion 91
6.9 Protein purification and labeling 91
6.9.1 Protein labeling with NHS-ester conjugated dye 93
6.9.2 SDS-PAGE 93
6.10 Lipid labeling 94
6.11 Stimulated emission depletion microscopy 95
6.12 Single-molecule imaging 95
6.12.1 Single-molecule HiSiaP-AF647 LUV binding assay 95
6.12.2 Single-molecule FRET calibration measurement 96
6.12.3 ALEX single molecule FRET measurements 96
6.13 Ensemble FRET measurements in solutions 97
6.14 Ensemble FRET measurements in GUVs 97

7 Appendix **108**

Abbreviations

AA	acrylamide
ABC	adenosine triphosphate binding cassette
ABD	7-amino-2,1,3-benzoxadiazol-4-yl
AF	AlexaFluor
ALEX	alternating-laser excitation
ATP	adenosine triphosphate
BA	bisacrylamide
Bio	biotin
BSA	bovine serum albumine
CDFI	chlorophenyl-dimethylbenzylpiperidinyl-fluoro-indole
CF	carboxyfluorescein
CD	cyclodextrin
CMC	critical micelle concentration
ComD	compound D
Cryo-EM	Cyro-electronmicroscopy
DNA	desoxyribonucleic acid
DDM	n-Dodecyl-β-D-maltoside
DLS	Dynamic Light Scattering
DOPC	1,2-dioleoyl-sn-glycero-3-phosphocholine
DOTAP	1,2-dioleoyl-3-trimethylammonium-propane
DOTM	n-dodecyl-β-D-thiomaltopyranoside
FITC	fluoresceinisothiocyanate
FRET	Förster resonance energy transfer
GUV	giant unilamellar vesicle
HEPES	4-(2-hydroxyethyl)-1-piperazineethanesulfonic acid
Hi	*Haemophilus influenzae*
IFS	inward facing state
KCl	potassium chloride
LUV	large unilamellar vesicle
MATE	multidrug and toxic compound extrusion
MOP	multidrug/oligosaccharidyl-lipid polysaccharide

NA	numerical aperture
NaV	neutravidin
Nb	nanobody
NBD	7-nitro-2,1,3-benzoxadiazol-4-yl
Neu5Ac	N-acetylneuramic acid
NHS ester	N-hydroxysuccinimidylester
OFS	outward facing state
PBP	penicilin binding protein
PC	phosphatidylcholine
PE	phosphatidylethanolamine
PMA	phosphomolybdic acid
PL	Polar lipid extract
POPC	1-palmitoyl-2-oleoyl-sn-glycero-3-phosphocholine
POPG	1-palmitoyl-2-oleoyl-sn-glycero-3-phosphoglycerol
ROI	region of interest
Saf	safranine
SBP	substrate binding protein
SDS PAGE	sodium dodecyl sulfate polyacrylamide gel electrophoresis
SEDS	shape, elogation, division and sporulation
sm	single molecule
SNARE	SNAP receptors
STED	Stimulated Emission Depletion
SUV	small unilamellar vesicles
TG	transglycosylation
TIRF	Total Internal Reflection Fluorescence
TP	transpeptidation
TRAP	tripartite-ATP-idependent periplasmic
UDP	uridine diphosphate
Val	valinomycin
Vc	*Vibrio cholerae*
VHH	variable domain of the H-chain of heavy chain only antibodies
wt	wildtype

One letter amino acid abbreviations

A	alanine
R	arginine
N	asparagine
D	aspartic acid
C	cysteine
Q	glutamine
E	glutamic acid
G	glycine
H	histidine
I	isoleucine
L	leucine
K	lysine
M	methionine
F	phenylalanine
P	proline
S	serine
T	threonine
W	tryptophan
Y	tyrosine
V	valine

1 Introduction

Embedded in the lipid bilayer, membrane proteins orchestrate core processes of cellular life, including transport, signaling and energy conversion. In pathogenic bacteria, specific membrane proteins serve as virulence factors, mediating invasion and immune evasion [55]. The medical significance of membrane proteins is underscored by the fact that over 60% of all current drugs target them [104] [66], although they make up for only about 30% of the proteome of higher organisms [99]. Despite their medical relevance, these proteins are under-characterized and -analyzed, when compared to soluble proteins. As of January 2021, membrane proteins only made up for less than 2.6% of all structures in the Protein Data Bank [41]. The reason for this lies in the amphiphilic nature of membrane proteins, which makes them difficult to purify and study. Most membrane proteins require a hydrophobic environment to maintain their active conformation [62]. Artificial membranes allow *in vitro* investigation of membrane proteins under controlled conditions, enabling the mechanistic dissection of their function, dynamics and interaction with substrates or inhibitors [82]. This thesis is focused on investigating two different membrane transport processes *in vitro*.

One protein central to this study is the bacterial lipid II flippase. Lipid II is a membrane-anchored cell wall precursor. Its translocation from cyto- to periplasm is required for cell wall synthesis, which is a highly conserved process and strictly required for growth of bacteria with a cell wall [86]. This important process must be mediated by a flippase [79]. However, the identity of the lipid II flippase remains under discussion. It is crucial to investigate the lipid II flipping ability of the three most likely candidates MurJ, FtsW and RodA to understand cell wall synthesis [56] [15]. Clarifying the individual roles of these membrane proteins could not only resolve long-standing controversies in the field but also identify potential targets for the development of new antibiotics.

Also central to this study are tripartite-ATP-independent periplasmic (TRAP) transporters. They constitute a class of secondary active transporters which are found in bacteria and archaea, including human pathogens, causing cholera and meningitis [70]. TRAP transporters mediate nutrient uptake in pathogens, especially in nutrient-limited environments like a host [33]. *Haemophilus influenzae* (Hi) and *Vibrio cholerae* (Vc) use TRAP transporters to import sialic acids, which aid in immune evasion and, thus, promote host colonization. The absence of TRAP transporters in humans opens up the possibility to target this system for medical treatment. TRAP transporters rely on a periplasmic substrate-binding protein (SBP) to deliver the substrate to the membrane-inserted part of the protein complex [61]. While structural insights are emerging, we

still lack a full understanding of how the SBP interacts exactly with the membrane domain and how the ion coupled substrate import is orchestrated.

1.1 Membrane model systems

Membrane model systems are of high importance to investigate membrane protein activity under controlled conditions. They reduce the complexity of biological membranes and, thus, provide a reproducible and accessible platform to study physical and functional properties of biological membranes [82]. They are essential in uncovering fundamental membrane processes, such as: Lipid-protein interactions, membrane fusion and fission, membrane dynamics, phase separation, domain formation and drug delivery [10]. There is a multitude of different model systems with different advantages and disadvantages. Generally, they can be classified into planar and spherical systems. In this work only spherical systems were used. Therefore, the following sections focus exclusively on these model systems.

1.1.1 Spherical model systems

Spherical membrane model systems are artificial vesicles that constitute a closed system. The vesicle lumen and environment are separated by the membrane. Passive passage of most charged, hydrophilic molecules through intact membranes is negligible without specific ion channels or transporters [103]. This is why they are of high interest to study membrane protein regulated transport processes [10]. Additionally, vesicles can be used to trap polar substances in their lumen as cargo. A schematic representation can be seen in figure 1.

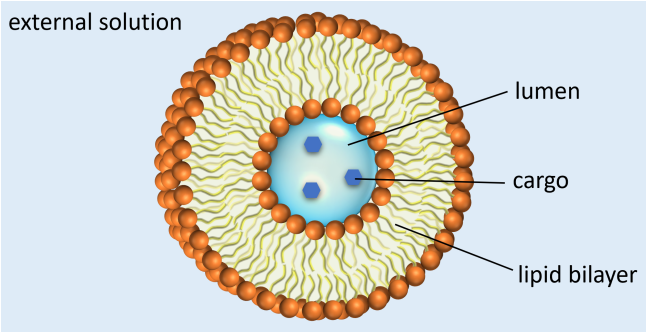


Figure 1: Vesicle structure. Schematic representation of a unilamellar vesicle with its lipid bilayer separating the lumen and the surrounding external solution. Cargo molecules are shown in the vesicle lumen.

Vesicles can be categorized by size into three different classes. Vesicles of diameters between about 30 to 50 nm are commonly called small unilamellar vesicles (SUVs) [29], vesicles exhibiting diameters between 50 nm and 1 µm are called large unilamellar vesicles (LUVs) [74] [64], while vesicles with diameters larger than 1 µm are named giant unilamellar vesicles (GUVs) [4]. SUVs and most LUVs range in size below the resolution limit of diffraction-limited light microscopy. This makes it impossible to resolve the membrane surrounding the vesicle lumen with these techniques. Their

small size, however, allows the observation of far more single vesicles within the field of view, when compared to GUVs. This enables high-throughput assays. Generally, LUVs and SUVs are also more stable than GUVs, which have a higher surface area, making them more susceptible to mechanical stress or rupture [58]. Depending on the desired diameter, different preparation methods must be used. A graphical overview of the different formation methods is depicted in figure 2.

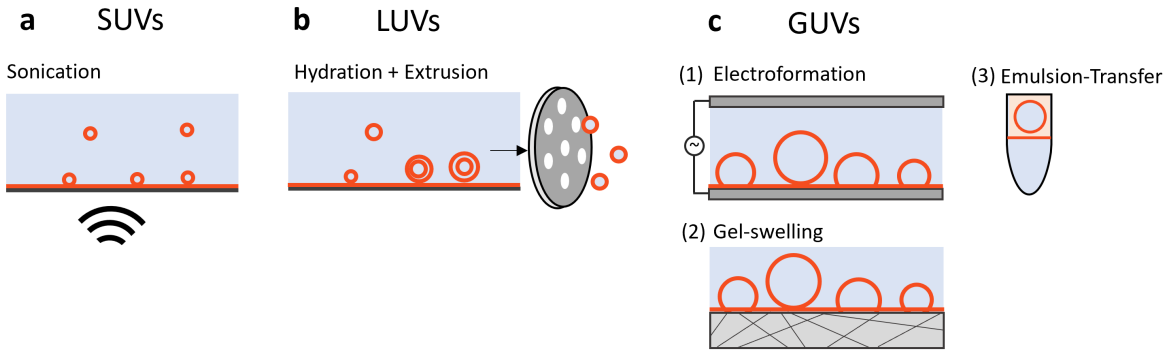


Figure 2: Vesicle formation methods. Schematic comparison of frequently used vesicle formation methods with lipids depicted in red, aqueous solutions in blue and organic solutions depicted in orange.

SUVs are usually prepared via sonication of a lipid film topped with aqueous solutions [29]. LUVs can be formed by hydration of a lipid film with aqueous solutions, followed by extrusion to achieve better size homogeneity and to break down multilamellar vesicles [64]. GUVs are most often prepared via electroformation [4]. In this method, lipids in an organic solvent are deposited onto electrodes. After chloroform evaporation, a thin lipid film remains. When this film is hydrated in an aqueous solution and subjected to an alternating electric field, the electrical stimulation induces the swelling and separation of the lipid layers, resulting in the formation of GUVs [4]. Electroformation could originally only be used in ion-free solutions. Li *et al.* showed in 2016, that the method can also be carefully adapted for salt-containing solutions [43], however, this method still poses a significant challenge. In 2009, Horger *et al.* described a method to prepare GUVs by depositing a lipid film on dried agarose. When hydrated, this method results in GUV swelling [28]. Lira *et al.*, 2014 found that this leads to incorporation of small amounts of agarose into the vesicles, which affects their properties [45]. In 2020, Parigoris *et al.* presented a GUV preparation method substituting the agarose by polyacrylamide gels, which allowed them to reach higher GUV yields and more unilamellar GUVs [67]. As an alternative to swelling-based methods, emulsion-transfer has been proposed for GUV formation [68]. In this method, water-in-oil emulsions, coated with lipids, are transferred through an oil-water interface to produce GUVs [68]. This preparation method, however, can lead to residual oil in the formed GUVs, which can result in membrane destabilization [40].

1.1.2 Membrane protein reconstitution

Membrane proteins are usually extracted out of biological membranes by employing detergent solutions. The amphiphilic detergent molecules self-assemble in aqueous solutions to form micelles, if used in concentrations higher than the critical micelle concentration (CMC) [7]. The micelles' hydrophobic cores can then shield hydrophobic domains of the membrane proteins from the surrounding water molecules and, thereby, stabilize them. The non-ionic detergent dodecyl-β-D-maltoside (DDM) was found to be well-suited for this purpose and is, therefore, widely used for membrane protein purification.

Reintroducing the membrane proteins into artificial lipid bilayers is often challenging and most commonly performed on small vesicles (SUVs and LUVs) [3]. It requires the permeabilization of the vesicles with detergent molecules, so that the protein-detergent micelles can merge with the membrane and form vesicles that contain membrane proteins [17]. In the following, these vesicles will be called proteo-vesicles. The resulting protein orientation in the membrane depends on a multitude of parameters. The most influential factors, however, are charge or hydrophilic domain asymmetry of the membrane proteins. These properties can induce a preferred insertion direction [96] [102]. After protein insertion, the detergent molecules have to be removed from the membrane, often by using hydrophobic beads, cyclodextrins or dialysis [17]. The hydrophobic beads possess a large surface area and strong hydrophobic character, enabling them to effectively adsorb detergents from aqueous solutions [75]. Cyclodextrins, on the other hand, are cyclic oligosaccharides characterized by a hydrophilic exterior and a hydrophobic central cavity. Cyclodextrins bind detergents through inclusion complex formation, where the hydrophobic part of the detergent molecule is inserted into the hydrophobic cavity of the cyclodextrin, while the hydrophilic parts remain exposed to the aqueous environment [13]. This interaction is highly selective and efficient: Cyclodextrins have a much higher affinity for detergents than for bilayer-forming lipids, enabling them to selectively extract detergent molecules from vesicles without removing membrane-forming lipids [13].

The reconstitution into more fragile model systems like GUVs is extremely challenging, as they react very sensitively to detergent molecule presence. At higher detergent concentrations, the membrane can reach a critical point, resulting in the rupture of the vesicle [35]. Despite this, usually a detergent concentration above the CMC is necessary to stabilize membrane proteins in detergent micelles. There are three different methods which are commonly used for the formation of proteo-GUVs [20]. These are schematically demonstrated in figure 3.

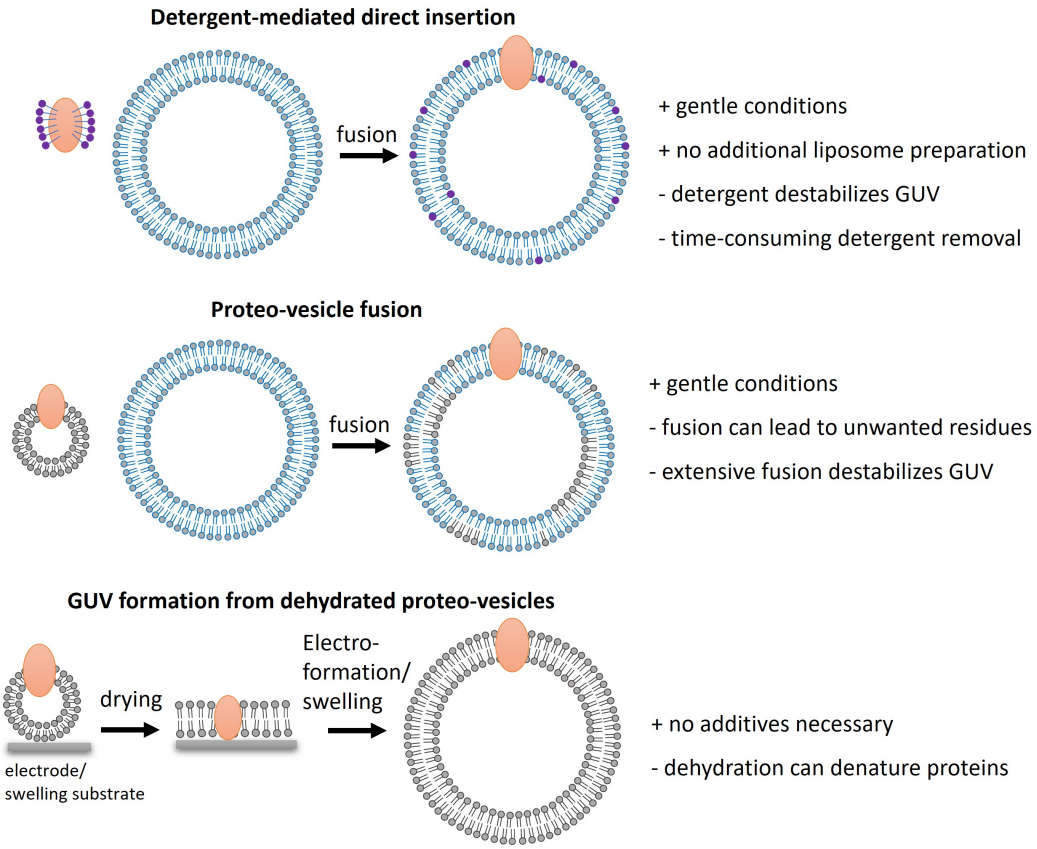


Figure 3: Membrane protein reconstitution in GUVs. Three different membrane protein reconstitution pathways for GUVs with their advantages and disadvantages. Image based on [20] and [44].

The first possible method is the detergent-mediated direct insertion of membrane proteins. This requires the exact adjustment of the detergent concentration to be high enough to stabilize the membrane proteins, but low enough to not destroy the GUVs [14]. As this optimal point is hard to achieve, often other methods are are employed. An alternative method is the fusion of small target protein containing vesicles to GUVs. The small proteo-vesicles can be formed as described earlier. Fusion from the donor to the target membrane can happen charge-mediated, if donor and acceptor membranes carry opposite charges [44]. Another possibility is the usage of polyethylene glycol (PEG) in combination with small amounts of amphipathic perturbant molecules in the membrane [50]. Finally, fusion can also be caused by using v- and t-soluble N-ethylmaleimide-sensitive factor attachment receptor (SNARE) proteins. When target and donor membrane come into proximity, the t- and the v-SNARE proteins zip together which brings the two membranes into tight contact [93]. Vesicle fusion allows a controlled delivery of proteins into pre-formed GUVs while preserving protein functionality and orientation, as the fusion usually happens under gentle non-denaturing conditions [44]. A disadvantage with this method is the necessity to use agents that support the fusion process. This will lead to residues of these substances

in the membrane. Another alternative membrane-protein reconstitution method also utilizes small proteo-vesicles. These are then dehydrated, either on an electrode surface for electroformation, or on a swelling substrate for gel-assisted swelling [20]. The dehydration process can lead to protein denaturation. In addition to that, the starting salt concentrations must be low, as they increase strongly during dehydration. This may also be harmful to the protein [20].

Finally, an overview of advantages and disadvantages of the presented spherical model systems is shown in table 1.

Table 1: Advantages and disadvantages of spherical unilamellar membrane model systems

Model	Advantages (+)	Disadvantages (-)
GUVs	+ resolvable with light microscopy + easy single-vesicle analysis	- difficult cargo encapsulation - fragile - hard to form in salt solutions - big size variability - difficult membrane protein reconstitution
LUVs	+ good for high-throughput assays + easy cargo encapsulation + easy membrane protein reconstitution + stable	- not resolvable with standard light microscopy - limited size variability
SUVs	+ uniform size + easy membrane protein reconstitution + good for high-throughput assays + stable	- very high curvature - not resolvable with standard light microscopy

1.2 Transporter proteins

An important function of integral membrane proteins is the transport of substances over the membrane, which cannot pass through the membrane by simple passive diffusion. This can be accomplished via different mechanisms.
Generally, active and passive import can be differentiated, dependent on whether an energy input is required for the process or not [89]. One example for passive transport is facilitated diffusion along a concentration gradient. Unlike simple diffusion, it

requires a specific transporter protein, but does not need an energy input [89]. Active transports can be subdivided into primary and secondary transport. In the first case, energy is generated from ATP hydrolysis. Among the protein systems that rely on this mechanism, ATP-binding cassette (ABC) transporters are a well-characterized example [89]. Secondary active transport utilizes energy stored in form of membrane potential ($\Delta\psi$) and ion gradients (Δion) to move substrates. Ions are co-transported in this case along their electrochemical gradient to gain energy. In secondary active transporters, sym- and antiport can be differentiated. A process is called symport, if the co-transported ion moves in the same direction as the substrate. A process is called an antiport if the co-transport happens in the opposite direction as the substrate transport [89]. In addition to proteins that transport water-soluble substrates, also lipid transporter proteins exist. These proteins faciliate lipid flip-flop through membranes [81]. Flip- and floppases use ATP or electrochemical gradients as energy source to transport very specific lipids in a unidirectional manner. Scramblases mediate bidirectional, energy-independent movement and are usually able to transport a variety of different phospholipids [81]. A schematic representation can be seen in figure 4.

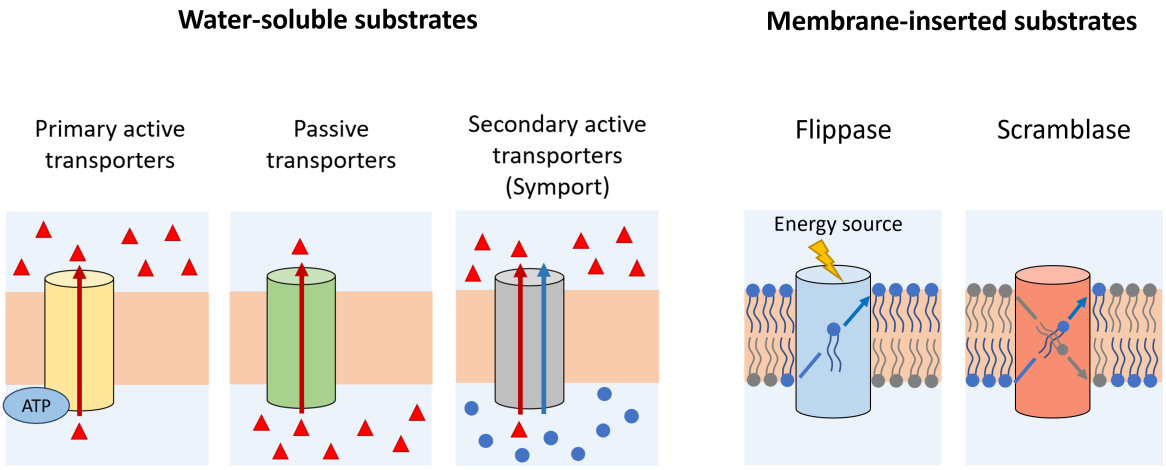


Figure 4: Mechanisms of transporter proteins. Schematic representation of different types of membrane transporter proteins. Transporters of water-soluble substrates are shown on the left. The substrate is depicted as red triangle. Transporters of membrane-inserted substrates are shown on the right. Substrate movement is indicated with arrows. Image based on [89] and [81].

1.2.1 Lipid II flippase

Most bacteria are surrounded by a cell wall, consisting of peptidoglycan, a mesh-like polymer, made of alternating interconnected polysaccharide chains. This cell wall is necessary in bacteria to balance for their high turgor pressure [86]. Peptidoglycan synthesis is indispensable for bacterial cell growth. This is why it is used as a point of attack for many antibacterial substances. Briefly, peptidoglycan synthesis starts

in the cytoplasm. Here, uridine diphosphate (UDP)-N-acetylmuramyl-pentapeptide is synthesized. This molecule is coupled by MraY to undecaprenylphosphate, which acts as a membrane anchor in order to form lipid I. Subsequently, MurG couples UDP-N-acetylglucosamine to lipid I, which yields lipid II. In the following, lipid II is translocated by a lipid flippase through the membrane. Transglycosylation and transpeptidation, executed by the penicillin-binding-proteins (PBPs), then lead to cross-linking of the peptidoglycan layer [47]. Here, PBPs of class A (aPBPs) and PBPs of class B (bPBPs) can be differentiated. While aPBPs possess a transglycosylase (TG) domain and a transpeptidase (TP) domain, bPBPs usually only possess a TP domain [53]. A schematic overview of these steps and of the lipid II structure is shown in figure 5.

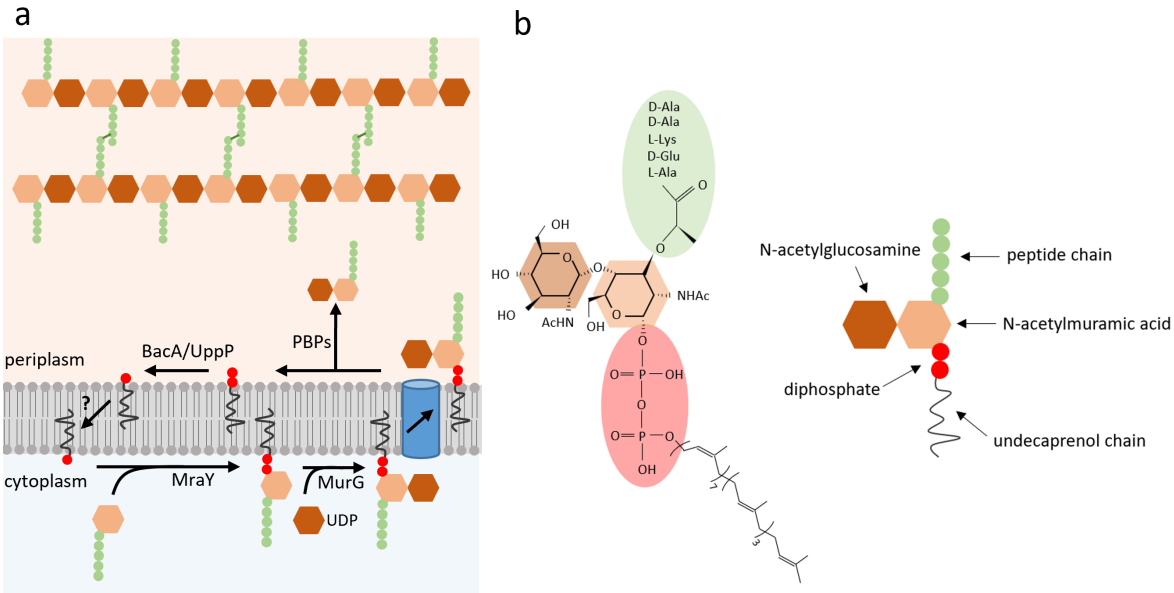


Figure 5: Cell wall biosynthesis. a: Schematic depiction of the cell wall synthesis steps which are executed in the membrane. **b:** Lys-lipid II with important structural components highlighted. Image based on [47].

One of the most crucial processes in the peptidoglycan synthesis is still under discussion, since the molecular details of the lipid II membrane translocation remain unclear. Currently, three different candidates are under discussion to be acting as the lipid II flippase: MurJ, a member of the multidrug/oligosaccharidyl-lipid polysaccharide (MOP) exporter family, and the shape, elongation, division and sporulation (SEDS) proteins RodA and FtsW, which are well known as integral components of the elongasome and divisome, respectively [38] [56] [79].

MurJ

First evidence pointing towards MurJ as lipid II flippase were gained from a reductionist bioinformatics search that identified MurJ as most likely flippase, due to its conservation among species which possess peptidoglycan and its absence in species that do

not produce peptidoglycan [78]. MurJ belongs to the MOP exporter superfamily [31] and shows a structural resemblance to the well studied multidrug and toxic compound extrusion (MATE) family [79]. MATE transporters presumably utilize an antiport mechanism to transport amphiphilic molecules from the cytoplasm to the periplasm via an alternating-access mechanism. The substrate transport is accompanied by a counter ion that is imported into the cytoplasm. Therefore, the electrochemical gradient of cations across the membrane has been proposed as energy source for this process [79] [49] [92]. In 2014, Sham *et al.* showed that MurJ inhibition via cysteine-linking *in vivo* leads to the build up of untranslocated lipid II and is lethal in *E. coli* [85]. FtsW inhibition in a Δ*rodA* strain did not lead to attenuation of lipid II flipping [85]. Furthermore, it was shown that membrane potential dissipation led to inhibition of the flipping process, confirming the electrochemical gradient as an energy source for the translocation [77]. Structure-guided cystein crosslinking coupled with proteolysis gel-analysis studies were able to detect inward- and outward-facing states of MurJ, confirming an alternating-access mechanism [38]. Interestingly, membrane potential disruption reduced the prevalence of the inward-open, but not the outward-open conformation [38]. The cumulated knowledge points towards a mechanism, proposed by Kumar *et al.*, 2019 [38], which is schematically depicted in figure 6.

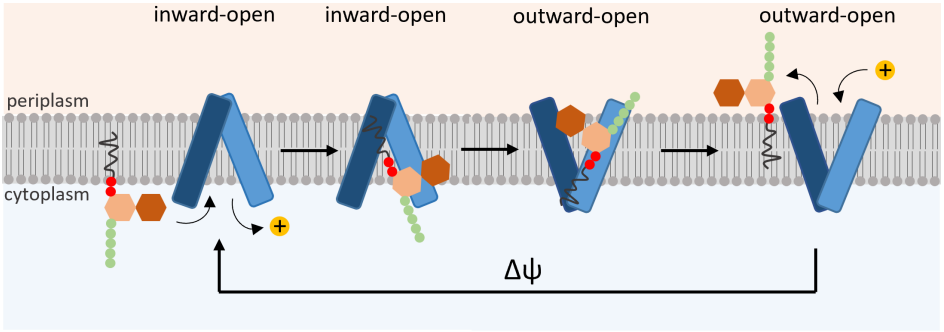


Figure 6: Proposed model of MurJ flipping. Schmematic representation of how the putative lipid II flippase MurJ flips lipid II via an alternating-access antiport mechanism as proposed by Kumar *et al.*, 2019. The membrane potential is indicated as $\Delta\psi$. Image based on [38].

Presumably, the translocation starts by inward-open MurJ binding to lipid II. Then, via an alternating access mechanism, lipid II gets flipped from the cytoplasmic side of the membrane to the periplasm. Simultaneously, MurJ transitions into an outward-open conformation. Subsequently, lipid II is released on the periplasmic side of the membrane. Exploiting the membrane potential, MurJ resets back into the inward-open conformation, by shuttling a cation along its gradient from peri- to cytoplasm [38].

FtsW and RodA

FtsW and RodA exhibit a high structural resemblance. Both proteins were found to be part of the SEDS proteins. SEDS proteins have been shown to interact with bPBPs, together they can perform transglycosylation and transpeptidation [53] [91]. While RodA is part of the cell elongation complex in rod-shaped bacteria, FtsW is part of the cell divisome and presumably responsible for cell wall synthesis at the division site [91].

In 2011, Mohammadi *et al.* performed *in vitro* lipid II flipping assays by using 7-Nitro-2,1,3-benzoxadiazol-4-yl-labeled lipid II (lipid II-NBD) and FtsW reconstituted in LUVs. Sodium dithionite quenching of the outer leaflet lipid II-NBD revealed lipid II translocation by FtsW in absence of a membrane potential [56]. The assay was also performed with reconstituted MurJ, which did not show any translocation activity. However, no membrane potential was implemented into any of their experiments [56]. Later on, Mohammadi *et al.* tested for the specificity of the FtsW translocation and found that FtsW transports lipid II and phospholipids presumably through different mechanisms of facilitated diffusion, rather than a lipid II specific mechanism [57]. In 2025, Englehart *et al.* created a *B. subtilis* strain that is viable without MurJ, indicating that MurJ is at least not the sole lipid II flippase in *B. subtilis* [15]. They suggested a dual pathway for peptidoglycan synthesis. One that involves MurJ as flippase, providing lipid II for aPBPs, and an alternate lipid II flipping mechanism carried out by RodA/FtsW in complex with bPBPs in which this complex performs flipping and peptidoglycan synthesis [15]. The proposed pathways are depicted in figure 7.

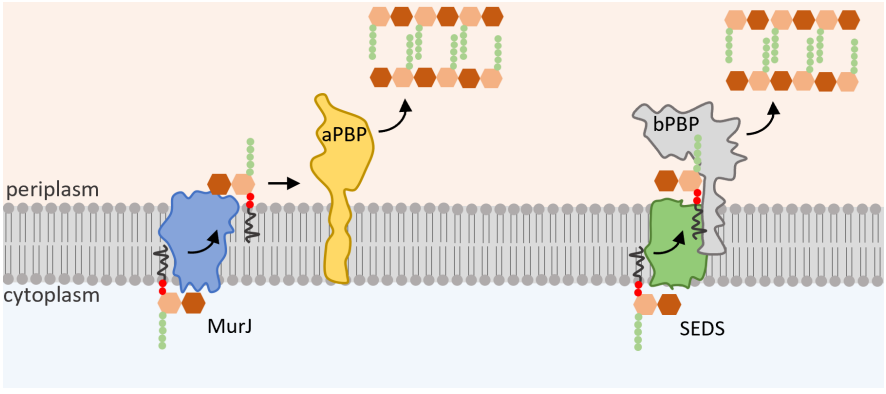


Figure 7: Proposed dual peptidoglycan synthesis pathway. Schematical depiction of two independent peptidoglycan synthesis pathways as suggested by Englehart *et al.*, 2025. Image based on [15].

1.2.2 Tripartite ATP-independent periplasmic transporters

Tripartite-ATP-independent periplasmic (TRAP) transporters were discovered in the laboratory of David J. Kelly [33]. While absent in eukaryotic cells, bacteria and archaea use TRAP transporters to import different substrates [33]. The TRAP protein complex is made of a water-soluble high-affinity substrate-binding protein (SBP), named P-domain, and a smaller (Q-) and a bigger (M-) membrane-inserted domain. Q- and M-domain can be fused into a single polypeptide chain or expressed as individual proteins that form a tight complex in the membrane [60] [61]. The P-domain diffuses freely through the periplasm of Gram-negative bacteria and can bind the substrate with high affinity. This leads to its transition from P_{open} to P_{closed}, as SBPs were found to have a conserved architecture of two globular domains connected by a hinge, which can close around the substrate [69].

Mechanistically, TRAP transporters can be described as SBP-dependent secondary active transporters [70]. This means that unlike other secondary-active transporters, which can accept substrates directly from the environment, TRAP transporters can only accept substrates delivered from the P-subunit [61]. Furthermore, it was shown that substrate import was ATP-independent, but did require a sodium gradient as energy source [61]. The most studied TRAP transporters are HiSiaPQM and VcSiaPQM from *Haemophilus influenzae* (Hi) and *Vibrio cholerae* (Vc) respectively, both of which transport sialic acids. The general structure of sialic acids and the structure of N-acetylneuramic acid (Neu5Ac) is shown in figure 8. In humans, Neu5Ac is the most prevalent sialic acid, carrying a negative charge at physiological pH. Bacteria, like *H. influenzae*, cannot synthesize sialic acid themselves and, therefore, developed the ability to metabolize sialic acids from the host [12]. Additionally, sialic acids can be incorporated into their cell walls, enabling them to evade the host immune system by molecular mimicry [2]. This is possible due to the fact that eukaryotes use sialic acids as terminal residues on glycoproteins and glycolipids. There, they often serve as ligands for immune receptors like sialic acid-binding immunoglobulin-like lectins, which transmit inhibitory signals to dampen immune activation [34].

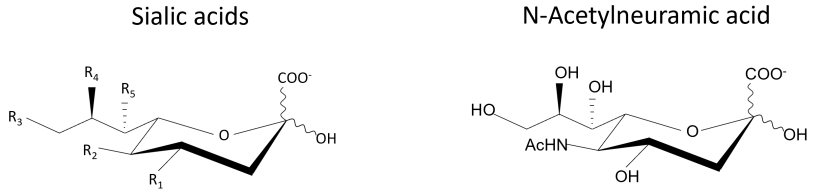


Figure 8: Structure of sialic acids. Left: General structure of sialic acids, **Right:** Structure of N-acetylneuramic acid (Neu5Ac).

Substrate import, executed by HiSiaPQM into LUVs was demonstrated by Mulligan

et al. in 2009. Purified HiSiaQM was reconstituted into proteo-LUVs and used in radiolabeled sialic-acid uptake assays [61]. Mulligan *et al.*, 2009 were able to show that HiSiaQM could only accept substrate from the SBP and did show increased activity in presence of a membrane potential, additional to a sodium gradient [61]. In 2022, Peter *et al.* revealed the structure of HiSiaQM via cryo-electronmicroscopy (Cryo-EM) and found that its structure suggests that TRAP transporters function as monomeric elevator-type transporters, in contrast to many other elevator-type transporters that operate as oligomers. The Q-subunit was proposed to form an essential part of the structural scaffold and to support the movement of the elevator-domain [70]. Based on an AlphaFold model prediction of the tripartite complex, they identified important regions and selectively introduced mutations, which were tested for their influence via growth assays. Furthermore, single-molecule microscopy was used to probe the interaction between HiSiaP and HiSiaQM. These experiments revealed that the substrate-bound SBP interacts more frequently with membrane-inserted HiSiaQM than the unbound SBP [70]. In 2024, Currie *et al.* identified the precise binding sites of two symported Na^+-ions and the substrate-binding site in HiSiaQM [12]. Overall, the available structural and biochemical evidence supports a transport mechanism, proposed by Peter *et al.* in 2022. The mechanism is depicted in figure 9 [70].

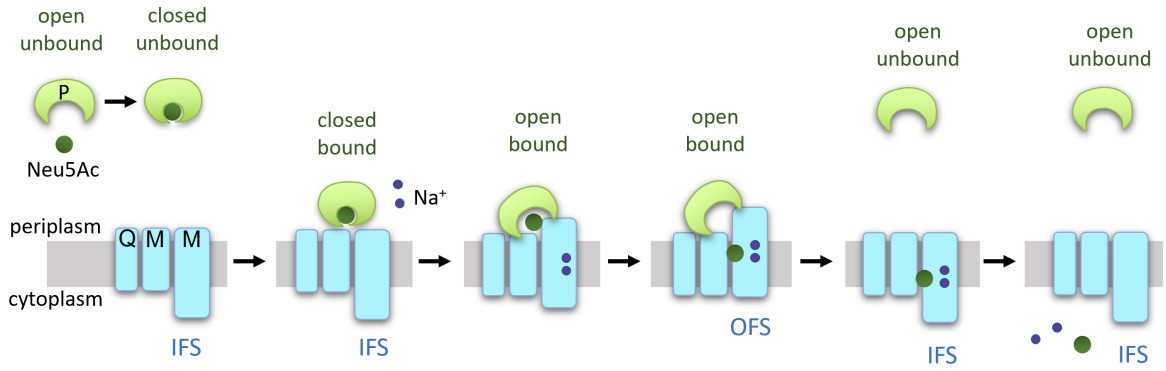


Figure 9: Proposed import mechanism for HiSiaPQM. Schematic depiction of Neu5Ac import. The QM-domain transitions from the inward-facing state (IFS) to the outward-facing state (OFS) and back. Image based on [70].

To initiate import, the substrate-carrying P-domain binds to the transporter in its inward facing resting state (IFS). Upon P-domain binding, the elevator domain likely moves upward into the outward-facing state (OFS), causing the P-domain to open and transfer its ligand to the QM-domain. The exact mechanism how this is executed remains unclear. Peter *et al*, 2022 hypothesized a "scoop loop", similar to the scoop-motif found in ABC-transporters, that mediates the substrate transfer from the SBP to the membrane-inserted protein subunit [70] [63] [42]. Further indications for this theory were found when Schneberger *et al.*, 2024 identified a variable domain of the H-chain of heavy chain only antibodies (VHH) that could trigger allosteric substrate

release by binding to a hydrophobic surface pocket of VcSiaP [84]. Schneberger *et al.* hypothesized that this effect could possibly be used by the QM-domain to mediate substrate transfer [84]. However, this theory could not be proven yet. As HiSiaPQM acts as a sodium symporter, sodium ions should be bound either before, during or directly after this process. Dissociation of P_{open} presumably then triggers the down-movement of the elevator domain back into the IFS. This process would release the sodium ions, as well as the substrate, into the cytosol [70]. The proposed mechanism is supported by additional experiments of Peter *et al.*, 2024 showing a conformational coupling between the IFS state of HiSiaQM and P_{closed}, as well as the OFS state of HiSiaQM and P_{open} [71].

1.3 Motivation

Active transport of hydro- or amphiphilic substrates across bacterial membranes is central to almost all aspects of bacterial cell growth. Therefore, these processes are of great interest for medical treatment against pathogenic bacteria, especially if the same systems are not found in eukaryotic cells. In this thesis two membrane transport systems were studied.

Lipid II flippase

The translocation of lipid II is one of the key steps for bacterial cell wall synthesis. Despite its relevance, the identity of the protein executing this task is still under discussion. Over the years, mainly three candidates have emerged as putative flippases: MurJ, FtsW and RodA. MurJ has been shown to perform lipid II flipping *in vivo*, if a membrane potential was present [77]. *In vitro* measurements have failed to show any flipping activity for MurJ [56]. However, it must be noted that these experiments have been performed in absence of a membrane potential [56]. FtsW's lipid II translocation activity, on the other hand, has been demonstrated, although in this case no *in vivo* activity could be proven yet. The goal of this thesis was to test all three putative flippase candidates for their flipping activity in biomimetic membrane systems that exhibit an electrochemical membrane potential to identify the flippase under conditions that mimic a real bacterial membrane as closely as possible.

TRAP transporter

TRAP transporters, like VcSiaPQM and HiSiaPQM, enable substrate uptake that aids pathogenic bacteria to evade the human immune system [70]. While the already existing structural and biochemical data provides a good foundation for hypotheses [61] [70], some mechanistic questions remain open. The aim of this work was to develop an *in vitro* FRET assay in biomimetic vesicles that enables HiSiaPQM activity observation for the first time directly in real-time. This assay can then be used to test the influence of environmental changes, like the presence of a membrane potential or the absence of a sodium gradient on the substrate import. Also, strategically placed point mutations can help to identify critical domains within the TRAP complex. Of special interest, in this regard, is the question whether substrate transfer from P to QM is really mediated by a mechanism similar to a "scoop-motif" [70].

2 Results

2.1 Modification and characterization of membrane model systems

To investigate membrane-transport processes under controlled conditions, GUVs and LUVs were used as model systems. While GUVs provide direct access to membrane morphology, as they allow distinction of lumen and membrane via fluorescence microscopy, LUVs offer an accessible system that is especially well suited for high-throughput biophysical assays [88]. In this work, the complementary strengths of both, GUVs and LUVs, were exploited. However, the model systems had to fulfill certain conditions to enable functional protein observation:

(1) High yield formation of vesicles in physiological salt solutions

(2) Vesicle immobilization to enable long-term observation

(3) Non-denatured membrane protein reconstituted

(4) Cargo encapsulation into vesicle lumen

(5) Defect-free membranes that enable functional sealing

(6) Majority of vesicles must be unilamellar

(7) Establishment of a membrane potential

To accomplish all these requirements fully, already existing methods for model system formation had to be modified. The following section presents the methodological developments implemented, along with a characterization of the model systems, employed in this thesis. Detailed protocols are provided at the end of the thesis in section 6.

2.1.1 Giant unilamellar vesicles

In this work, gel-assisted swelling was optimized as a formation route for GUVs [28]. The advantages of gel-assisted swelling include that it is more compatible with physiological salt-solutions (∼150 mM total monovalent ions) than electroformation [88]. It does not require specialized equipment and provides gentle formation conditions. However, gel-assisted swelling can impede encapsulation of proteins or large molecules into the vesicle lumen due to the steric hindrance, provided by the gel crosslinking. Furthermore, the most frequently used method for membrane protein reconstitution in gel-assisted swelling approaches is the dehydration of small proteo-vesicles on the gel substrate prior to the swelling [20]. This can harm sensitive membrane proteins [72].

To overcome the challenges described above, the following preparation procedure was developed in this work: Acryl-/Bisacrylamide (AA/BA) gels were chosen over agarose to avoid residual gel in the GUV lumen and membrane, as it was found for agarose-assisted swelling [45]. Variation of the BA to AA ratio was used to widen the pore size to allow for optimized cargo encapsulation. Gentle protein reconstitution was enabled by a direct insertion approach, meaning that the membrane proteins were transferred directly from detergent micelles into the GUV membrane. To prevent membrane protein aggregation, a detergent concentration above the CMC had to be maintained until the proteins were membrane-inserted [101]. This concentration was hardly tolerated by already formed GUVs, presumably due to asymmetric occupation of the outer leaflet by detergent molecules. Dodecyl-β-D-thiomaltoside (DOTM) was chosen as a detergent due to its low CMC in comparison to other, more often used, non-ionic detergents, like DDM [14]. To prevent GUV collapse from asymmetric detergent insertion, GUV formation was directly performed in presence of DOTM. Electroformation in presence of detergent has been demonstrated to work in 2013 by Dezi *et al.* [14]. Now this strategy was adopted to gel-assisted swelling. However, it has been shown that detergent molecules in the membrane increase the membrane permeability drastically [14]. To avoid leakiness of the produced GUVs, the detergent was complexed via cyclodextrin (CD) addition, and, therefore, removed from the membranes, before GUV formation was finalized. This complete process was named "Detergent-mediated swelling of proteo-GUVs" and is depicted schematically in figure 10.

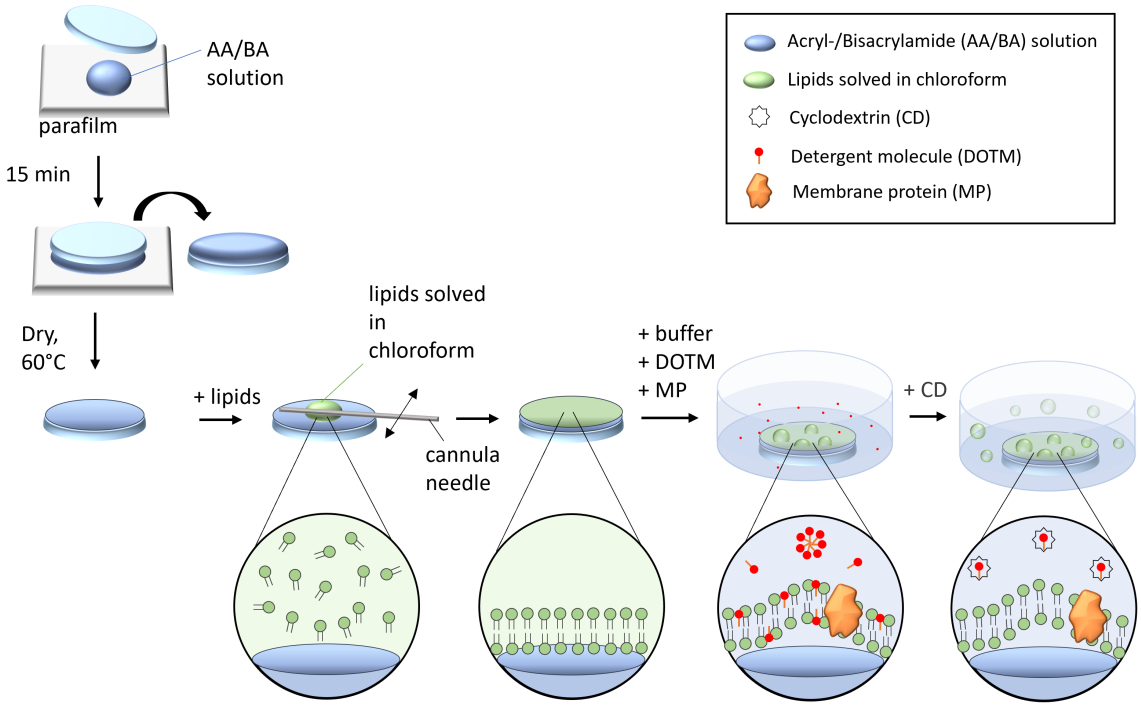


Figure 10: Detergent-mediated swelling of proteo-GUVs. AA/BA solution is applied onto a parafilm and covered with a coverslip. After the polymerization, the gel was dried for 30 minutes at 60°C. Then, chloroform-solved lipids were applied and spread on the gel with a cannula needle. To initiate the swelling, buffer was added after chloroform evaporation. DOTM was supplemented into the swelling buffer together with the membrane protein of interest. Detergent removal was carried out after 25 minutes of swelling via cyclodextrin addition.

In the following, it had to be validated whether this approach really fulfilled all the aforementioned criteria.

Detergent mediated swelling of GUVs

The process of detergent-mediated swelling could be followed via brightfield microscopy in real-time. An image taken after 40 minutes of swelling in 150 mM KCl/5mM HEPES/50 mM sucrose (pH 7.2) solution, supplemented with 0.25 mM DOTM, is shown in figure 11. CD had been added to a concentration of 0.7 mM after 25 minutes of swelling. In the shown image, the GUVs have nearly reached their final size, before detachment starts. Following the detachment, the GUV containing solution was removed from the gel-substrate and stored for further usage. The method successfully produced GUVs in physiological salt concentrations with a high yield.

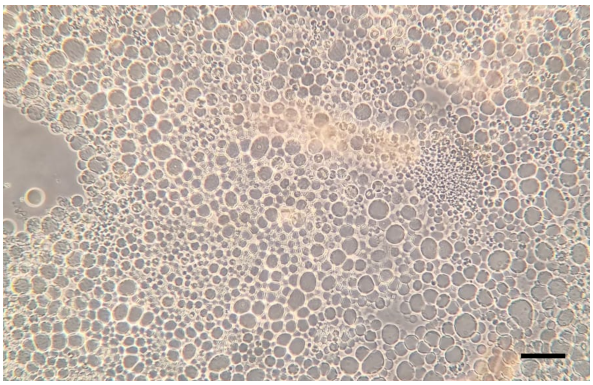


Figure 11: GUV swelling on AA/BA substrate. *E. coli* Polar Lipid Extract (PL)/POPC (3:1) GUVs formed in 150 mM KCl/5 mM HEPES/50 mM sucrose solution and imaged via brightfield microscopy, scale bar 50 µm, after 40 min of swelling.

Supplementation of the swelling buffer with sucrose led to a sedimentation of GUVs to the bottom of the coverslip, if the GUV solution was diluted in an equimolar glucose solution. This resulted in an effective immobilization of the GUVs. The average diameter of *E. coli* PL/POPC/TopFluorPC (3:1:0.01) GUVs was determined to be 12 ± 6 µm. A size histogram is is shown in the Appendix (App. 10).

Membrane protein reconstitution

Next, membrane protein reconstitution was tested. MurJ, FtsW, RodA and HiSiaQM were labeled with either AlexaFluor (AF) 647 or AF488. The strong hydrophilicity of both dyes minimized the likelihood of dye-driven membrane insertion [105]. Successful labeling of the proteins was tested via SDS-PAGE. The corresponding data is shown in the Appendix. Figure 12 shows membrane-localization of the fluorescent membrane proteins after reconstitution, using confocal laser scanning microscopy. None of the proteins showed visible aggregations in the membrane, which would point towards protein denaturation or a hydrophobic mismatch between membrane and protein [1].

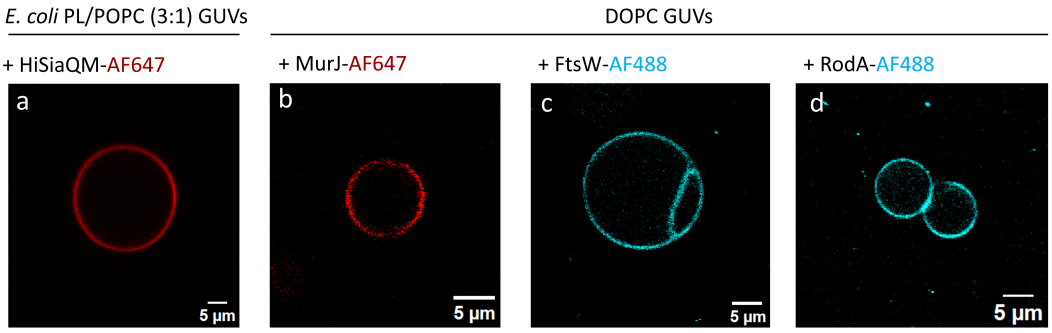


Figure 12: Membrane protein reconstitution in GUVs. a: *E. coli* PL/POPC (3:1) GUVs with HiSiaQM-AF647 reconstituted in a protein:lipid ratio of 1:1000, **b:** DOPC GUVs with MurJ-AF647 reconstituted in a protein:lipid ratio of 1:2500, **c:** DOPC GUVs with FtsW-AF488 reconstituted in a protein:lipid ratio of 1:2500, **d:** DOPC GUVs with RodA-AF488 reconstituted in a protein:lipid ratio of 1:2500.

To check whether HiSiaQM retains its natural conformation after membrane reconstitution, a VHH antibody, also called nanobody (Nb), labeled with AF647 (SDS-PAGE in App. 2), was added to HiSiaQM-containing GUVs in a concentration of 0.5 µM (figure 13). This test could not be performed for the other used membrane proteins, since no Nb or antibody was available. The $Nb_{HiSiaQM}$-AF647 signal colocalized with the lipid labels (TopFluorPC) in the GUV membrane, if HiSiaQM was present, indicating successful recognition and membrane insertion of HiSiaQM.

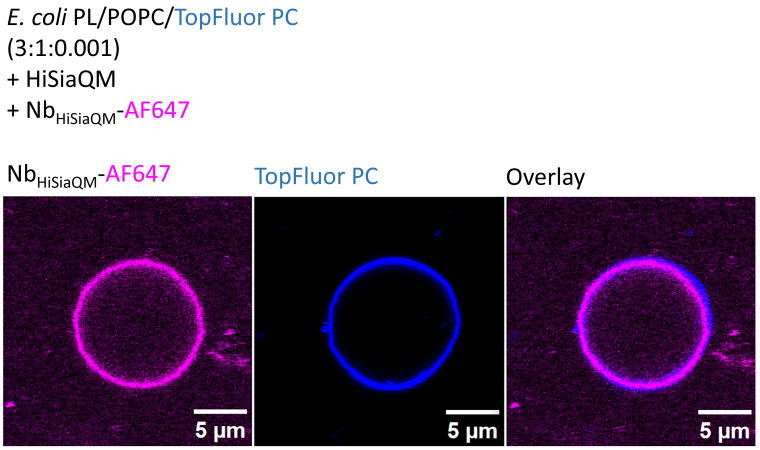


Figure 13: Reconstituted HiSiaQM is recognized by Nb. $Nb_{HiSiaQM}$-AF647 binding to HiSiaQM containing *E. coli* PL/POPC/TopFluor PC (3:1:0.001) GUVs.

Using membrane reconstituted HiSiaQM-NBD, the efficiency of the membrane protein reconstitution was tested by determining the average protein to lipid ratio in the GUV membrane via fluorescence microscopy. Detailed results are provided in the Appendix (App. 8). The average protein to lipid ratio in the GUV membrane was found to be about 1:2000, when the swelling buffer was supplemented with HiSiaQM-NBD in a protein to lipid ratio of 1:1000.

Cargo encapsulation

To functionalize vesicles, it is highly beneficial, if the vesicle lumen can be loaded with specific cargo. For this work, it was our goal to place a sensor protein inside the lumen. Therefore, the used polyacrylamide gel was adjusted to exhibit a large pore size. Then, it was tested whether the created GUVs could encapsulate cargo effectively, as well as maintain their membrane integrity to prevent cargo leakage.

It was tested whether fluorescein isothiocyanate (FITC) dextrans of different molecular sizes could be encapsulated by *E. coli* PL/POPC (3:1) GUVs. To this end, 10 kDa, 40 kDa and 500 kDa FITC dextran were added in a concentration of 1 µM into the GUV swelling buffer. The encapsulation efficiency for the different FITC dextrans was quantified as the ratio between the fluorescence intensity in- and outside the vesicle after diluting the vesicles 1 to 20. Therefore, complete encapsulation of the FITC dextran would result in a ratio of 20. Lower values indicate incomplete cargo encapsulation. The hydrodynamic radius of the dextrans used here was provided by the supplier [97] [100].

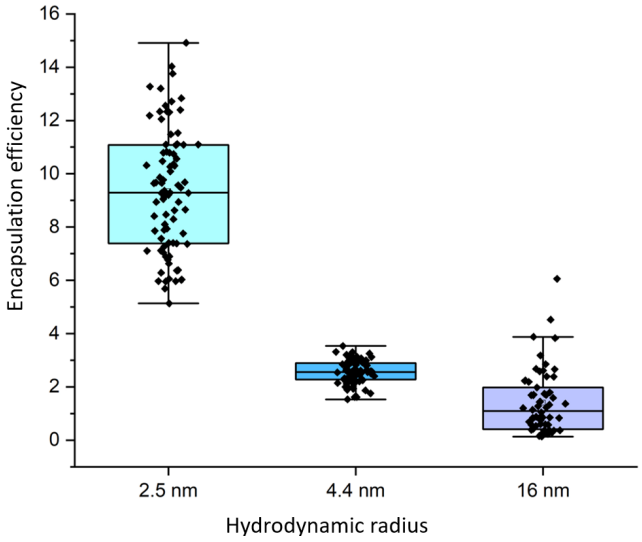


Figure 14: Cargo encapsulation. Encapsulation efficiency of differently sized FITC dextrans as boxplots after detergent-mediated swelling of *E. coli* PL/POPC (3:1) GUVs. Each diamond represents one GUV, three measurements were performed for each dextran.

As shown in figure 14, the encapsulation efficiency decreased with the hydrodynamic radius of the substrate. At a hydrodynamic radius of about 16 nm, the encapsulation efficiency was close to 1, indicating that almost no encapsulation was possible. Most protein radii, however, lie far below this value and should enable encapsulation [94].

Membrane integrity

The membrane integrity was tested via encapsulation of the small membrane impermeable fluorescent dye carboxyfluorescein (CF) [11]. To this end, CF was added in a concentration of 1 µM into the swelling buffer. CF-containing *E. coli* PL/POPC (3:1) GUVs were produced by detergent-mediated swelling and diluted 1 to 20, in order to create a CF gradient directed to the vesicle outside. The fluorescence intensity, contained within the vesicle lumen of 34 GUVs from three different samples, was monitored for 28 min, as shown in figure 15.

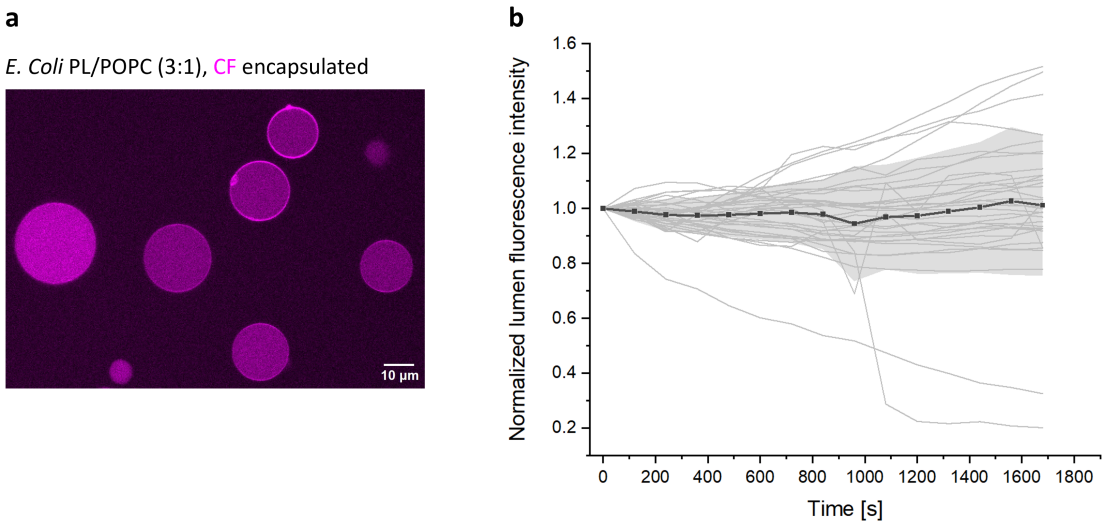


Figure 15: Membrane integrity. a: Image of CF loaded *E. coli* PL/POPC (3:1) GUVs. **b:** Normalized CF intensity in the GUV lumen of 34 GUVs from three different experiments over time. Normalization was based on the first intensity value.

Only 2 of the 34 observed vesicles exhibited a drop in fluorescence below 70%, indicating that most vesicles stayed intact over a time scale of 28 minutes.

Lamellarity

Multilamellar vesicles can pose a problem in investigating transport processes over membranes, as the substrate might not reach the lumen, if it is surrounded by multiple bilayers instead of just one. As the different lamellae are often only separated by few nanomenters, multilamellarity cannot be directly resolved via fluorescence microscopy [67]. To evaluate the lamellarity ξ of the prepared GUVs, a dithionite quenching assay was employed. This assay utilizes the membrane-impermeable reducing agent sodium dithionite to selectively bleach fluorescent lipids in the outer leaflet of the lipid bilayer [51]. For ideal unilamellarity ($\xi = 1$), a fluorescence intensity decrease of 50% would be expected upon dithionite addition. The relative drop in fluorescence decreases for increasing multilamellarity, as only the outermost leaflet can be reached by

dithionite. A schematic depiction of this process is shown in figure 16a.

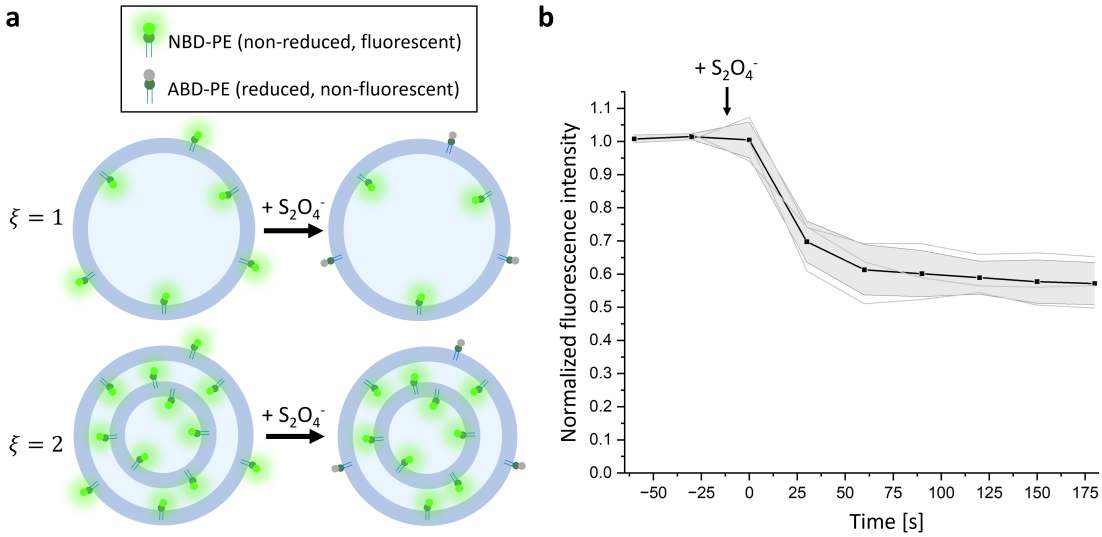


Figure 16: NBD-quenching via sodium dithionite. a: Principle of NBD reduction by dithionite in a uni- and bilamellar vesicle. **b:** Normalized mean fluorescence intensity of *E. coli* PL/POPC/NBD-PE (3:1:0.04) GUVs upon dithionite quenching. Three independent measurements were acquired and averaged. The individual measurements are depicted in light gray. The average fluorescence intensity before dithionite addition was used for normalization. The standard deviation is shown as a gray error band.

Here, GUVs were formed containing NBD-PE, which is a fluorescent lipid that is susceptible to irreversible fluorescence quenching upon reduction by sodium dithionite [56]. As shown in figure 16b, the addition of 0.6 mM dithionite resulted in a drop in NBD fluorescence, which reached a plateau at about 60%, corresponding to the protected (inner leaflet) NBD fraction.

In an alternative approach to quantify the lamellarity ξ, a linear relationship between the membrane fluorescence intensity and lamellarity was assumed, similar to the approach of Parigoris *et al.*, 2020 [67]. Therefore, the membrane fluorescence intensity of 108 *E. coli* PL/POPC/TopFluor PC (3:1:0.03) GUVs from three different samples was measured via the ImageJ/Fiji PlugIn 'Radial Profile Angle' by Paul Baggethun [83]. In short, the PlugIn identified a GUV's center and measured several line profiles starting from the center with varying angles. The line profiles were averaged and the maximum value of the average profile was defined to be the membrane fluorescence intensity. The minimum membrane fluorescence intensity was used to normalize all other values to and served as a reference. Normalized values less than 2× the reference were classified as unilamellar ($\xi = 1$), values between 2× and 3× the reference as bilamellar, and higher ranges were assigned to subsequent categories. The results can be seen in figure 17.

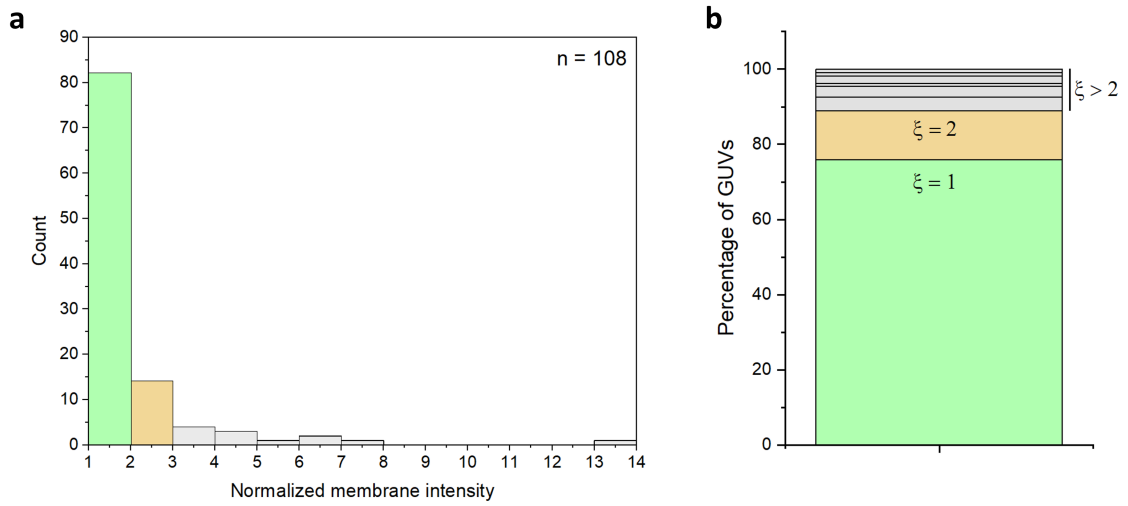


Figure 17: Lamellarity via radial profile analysis. a: Histogram of the normalized membrane fluorescence intensity, measured for 108 *E. coli* PL/POPC/TopFluor PC (3:1:0.03) GUVs. **b:** Stacked column, indicating the percentage of GUVs exhibiting different lamellarities.

The categorization indicated that 76 ± 2% of the measured GUVs were unilamellar. The protected fraction, in dependence of the corresponding lamellarity, was estimated as $\frac{1}{2\xi}$. Then, the average protected fraction could be calculated as a weighted average to be 58%. This result is in good agreement with the protected fraction, observed via dithionite quenching.

Establishing a membrane potential

Biological membranes exhibit a membrane potential, which serves as a driving force for many membrane transport processes [8]. Therefore, it is an important membrane property that needs to be mimicked in membrane model systems, if one wants to observe these processes *in vitro*.

A membrane potential over biomimetic membranes can be established by exploiting an already existing ion gradient [5]. If, under these conditions, a specific ionophor for one of the ion species is added, it allows for this ion species to permeate through the membrane until an electrochemical equilibrium is reached. As no other ion can cross the membrane, charge separation is the consequence. Here, valinomycin was used, which is a potassium ionophor [5]. Accordingly, an overall negative charge is built up in the vesicle lumen, as soon as potassium ions follow their gradient and leave the vesicle. The potential was measured using the Nernstian dye safranin, which is membrane-permeable and positively charged. Therefore, it migrates to the vesicle lumen to balance for the excess negative charge, if it builds up.

The membrane potential can be calculated using the Nernst equation:

$$\Delta\psi = \frac{RT}{zF} \times \ln\left(\frac{c_{in}}{c_{out}}\right) \tag{1}$$

with $\Delta\psi$ being the membrane potential, R being the gas constant, $z = 1$ being the charge number of safranin, F being the Faraday constant, T being the temperature, c_{in} being the safranin concentration on the vesicle inside and c_{out} being the safranin concentration on the vesicle outside. A calibration measurement was used to correlate the safranin concentration with the fluorescence intensity. The calibration measurement was performed in 'Inside'- (150 mM KCl/5 mM HEPES/50 mM sucrose) as well as 'Outside'-buffer (150 mM NaCl/5 mM HEPES/50 mM glucose) to check for possible differences caused by the different aqueous environment. The resulting graph is depicted in figure 18. A linear correlation between fluorescence and concentration was found, which did not change significantly depending on the surrounding solution.

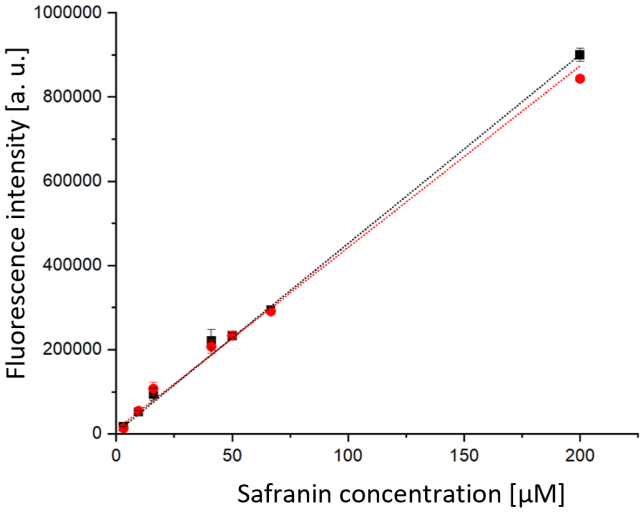


Figure 18: Calibration curve of safranin fluorescence. Safranin fluorescence intensity measured for different defined concentrations of safranin in 'Inside' (black filled squares) and 'Outside' buffer (red filled circles). Mean values of three measurements are shown with the respective standard deviation. The dashed lines show a linear fit performed for both conditions.

Subsequently, the measurements were performed in DOPC GUVs. Three different conditions were tested: (1) GUV solution was diluted 1:20 in 'Outside'-buffer and 5 µM valinomycin was added. (2) The GUVs were diluted 1:20 in 150 mM KCl, 5mM HEPES, 50 mM glucose solution and 5 µM valinomycin was added. (3) The GUVs were diluted 1:20 in 'Outside'-buffer but no valinomycin was added. All samples were supplemented with 6 µM safranin and imaged. Subsequently, the safranin concentration in- and outside the vesicles could be calculated from the respective fluorescence intensity. Inserting these values into the Nernst equation (eq. 1), yielded the respective membrane potential. The resulting values can be seen as a histogram in figure 19.

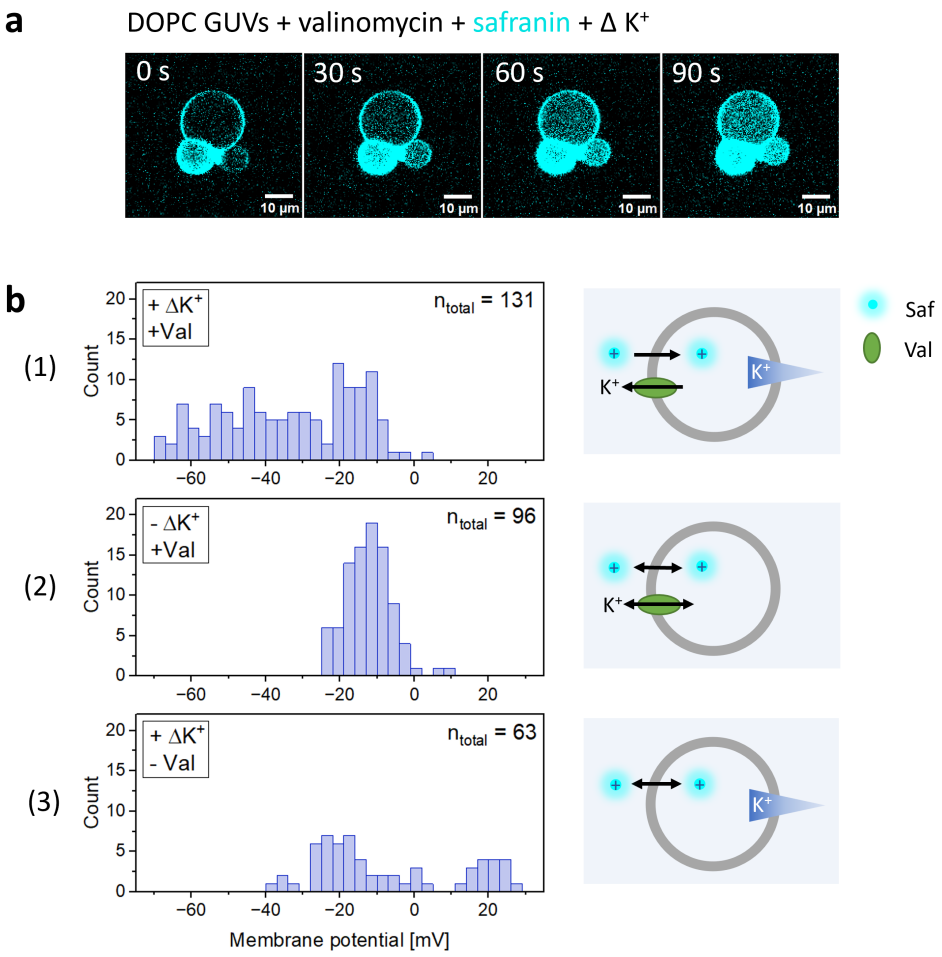


Figure 19: Membrane potential in DOPC GUVs. a: Time Series after 7 min of valinomyin (val) addition shows accumulation of safranin (saf) into the vesicle lumen. **b:** Histograms of the membrane potential distributions for different conditions. GUVs from three measurements were evaluated for each histogram. Next to each measurements is a schematic depiction of the respective conditions.

A membrane potential below -40 mV was only established in presence of both, a potassium gradient and a potassium ionophore. Under these conditions an average membrane potential of -34 ± 19 mV was achieved, although the GUVs exhibited a rather broad distribution, indicating two subpopulations. These could correspond to GUVs which could establish a membrane potential and GUVs that failed to do so. GUVs that do not exhibit unilamellarity are not expected to build up an observable membrane potential and would presumably contribute to the second subpopulation. The 1:20 dilution of the GUV solution in 'Outside-buffer' before imaging set the theoretically achievable membrane potential to -79.4 mV by defining the potassium gradient.

Energy gain from ion translocation in bacteria and GUVs

Next, the energy gained via ion translocation in GUVs and bacteria was compared to asses the GUVs' suitability to drive membrane transport. The Gibbs free energy

released by shuttling 1 mol of ions along its gradient was calculated as follows [6]:

$$\Delta G = zF\Delta\psi + RT\ ln\frac{c_{in}}{c_{out}} \tag{2}$$

with ΔG being the Gibbs free energy released per mol of ion translocation, $\Delta\psi$ being the membrane potential, R being the gas constant, z being the charge number of the ion, F being the Faraday constant, T being the temperature, c_{in} being the ion concentration on the vesicle inside and c_{out} being the ion concentration on the vesicle outside. Using $z = 1$, $R = 8.314$ Jmol^{-1}K^{-1} and $F = 96,485$ Cmol^{-1} next to the parameters given in the table below, ΔG could be estimated for Na^+ translocation in bacteria and in the here used model system.

Table 2: Comparison of different parameters in bacteria and GUVs.

	Bacteria	**Model system**
T	310.15 K	293.15 K
$c_{Na^+,\,out}$	150 mM [48]	150 mM
$c_{Na^+,\,in}$	10 mM [48]	0.1 mM
$\Delta\psi$	-150 mV [6]	-34 mV
$\Delta G/ion$	-21.5 kJmol^{-1}	-21.1 kJmol^{-1}

Both estimated values are similar. This indicates that the model system can, in principle, provide sufficient free energy to drive substrate uptake by Na^+ translocation. In comparison, the Gibbs energy of ATP hydrolysis was found to be $\Delta G = -31.6 \pm 1.3$ kJmol^{-1} by Meurer et al., 2017 [54] and lies, therefore, within the same order of magnitude.

This concludes the general assessment of the fundamental properties of the produced GUVs. In summary, the formed GUVs met all seven predefined requirements, although the membrane potential remains lower and more heterogeneous than in typical bacterial cells.

2.1.2 Large unilamellar vesicles

LUVs have the advantage over GUVs that their formation in physiological buffer conditions is common and uncomplicated [74] [64]. Also cargo encapsulation does usually not pose a problem. LUVs are used more often as a membrane protein containing model system. Therefore, it was not necessary to adjust already existing protocols

drastically. LUVs were produced according to the following workflow: First, multilamellar vesicles were created via hydration of a lipid film. Then, three freeze-thaw cycles were performed. After that, LUVs were either directly extruded via a 100 nm pore filter (detergent-free LUV formation) or diluted in detergent and membrane protein containing solution (formation of proteo-LUVs) [27]. If detergent was added, it was complexed via cyclodextrin addition after 15 minutes of incubation time. For the final step, extrusion through a 100 nm pore filter was performed.

To check for the LUV's overall morphology and integrity, stimulated emission depletion (STED) microscopy was used and compared with confocal images acquired at the same position in the sample. STED is a super-resolution fluorescence imaging technique that overcomes the diffraction limit. Hence, STED can achieve spatial resolutions down to 20–50 nm [24]. LUVs were imaged using the Stedycon microscope (Abberior Instruments GmbH, Göttingen).

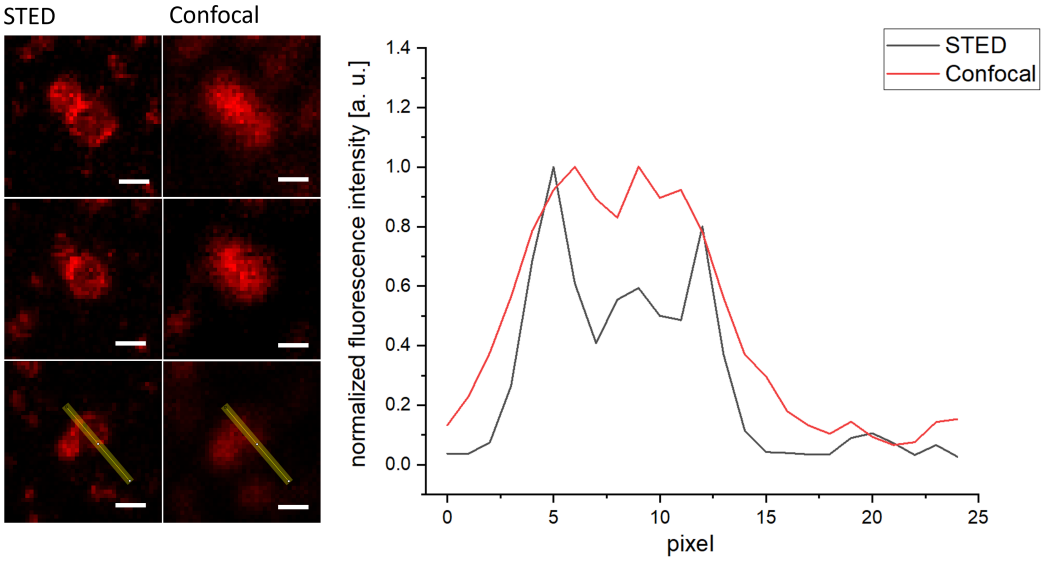


Figure 20: STED and confocal LUV images. STED and Confocal images, acquired with the Stedycon (Abberior Instruments GmbH, Göttingen) in the same sample position of DOPC LUVs, containing Atto647N-PE. Three different LUVs are shown. The scale bar is 200 nm. A line profile was measured through the confocal and the STED images as indicated for the third depicted LUV. The line profiles were each normalized to its maximal value and then plotted.

As visible in figure 20, the LUV membrane could only be resolved via STED. Line profiles show that in contrast to confocal microscopy, STED enabled distinct visualization of the two lipid bilayers on opposing ends of the vesicle.

Immobilization of LUVs

Immobilization of LUVs was a requirement for most of the planned measurements. It enabled washing or observation of the same vesicles over extended periods of time. While sucrose-loaded GUVs sediment to the ground and reside there relatively immobile, this method does not work for LUVs. Instead, LUVs could be embedded into ultra-low melting agarose [46]. This method produced LUVs which were fixed in a 3D space by an agarose mesh. Alternatively, immobilization of LUVs on a surface could be achieved by the following procedure: First, an ibidi µ-dish (ibidi, Gräfeling) was incubated with biotinylated bovine serum albumine (BioBSA), this led to unspecific adsorption of the BioBSA to the ibidi dish's surface. Unbound BioBSA was removed by a washing step. Subsequently, neutravidin (NAv) was added which bound specifically to the BioBSA. After another washing step, LUVs, containing biotinylated phosphatidylethanolamine (BioPE), could be immobilized on the ibidi dish's surface via BioBSA-NAv binding [36]. The final interaction is schematically depicted from a sideview in 21a.

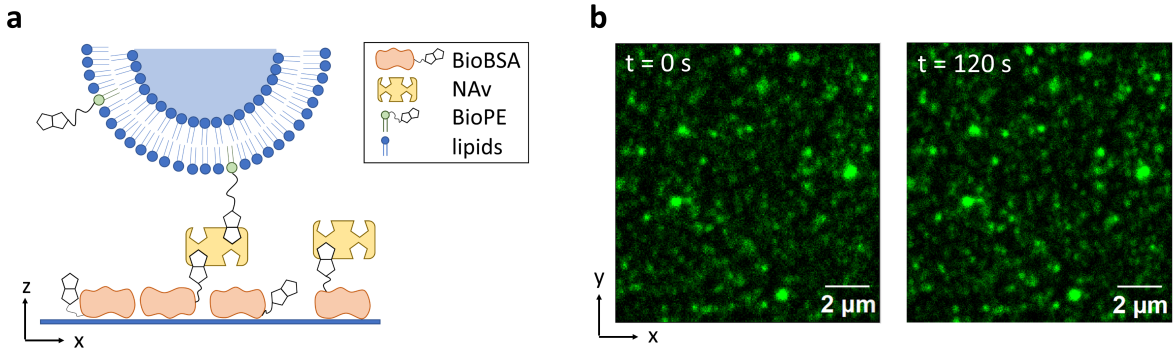


Figure 21: LUV immobilization. a: Schematic sideview (xz-plane) of the LUV immobilization via biotin-NAv binding. **b:** Surface-immobilized DOPC/BioPE (100:1) LUVs stained with safranin, at t=0 and t=120 s.

A time-lapse measurement of immobilized LUVs was used to show that the mobility of the bound vesicles was indeed very limited, as most vesicles remained in the same position after 120 s (figure 21b). For comparison: According to the Stokes-Einstein equation, an LUV of 100 nm diameter would exhibit a diffusion coefficient of 4.3 µm^2/s at 20°C, if non-immobilized, this would result in a root mean square displacement of 5.1 µm within 1 s.

Membrane protein reconstitution

To verify successful membrane protein reconstitution, HiSiaQM-AF546, MurJ-AF647, FtsW-AF488 and RodA-AF488 were reconstituted into DOPC LUVs (figure 22). SDS-

PAGE was used to confirm successful labeling. SDS-PAGE gel images can be found in the Appendix (App. 1, 3, 4).

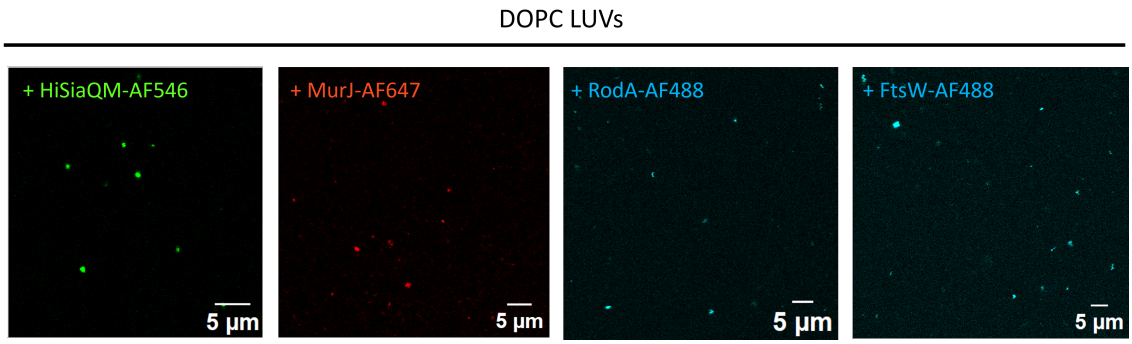


Figure 22: Membrane protein reconstitution in LUVs. Agarose-embedded DOPC LUVs with different reconstituted membrane proteins.

Additionally, it was found that $Nb_{HiSiaQM}$-AF647 was able to recognize LUV-inserted HiSiaQM. The respective images can be found in the Appendix (App. 5).

LUV size

To determine the LUV size distribution, dynamic light scattering (DLS) measurements were performed in a DynaPro NanoStar (Wyatt Technology). In order to check whether the protocol, used to reconstitute membrane proteins, changed the size distribution of the LUVs, the detergent-free preparation method was compared to the detergent-mediated preparation method. Furthermore, the same samples were measured after five hours of storage at 4°C to also check for time-dependent changes in the size distribution.

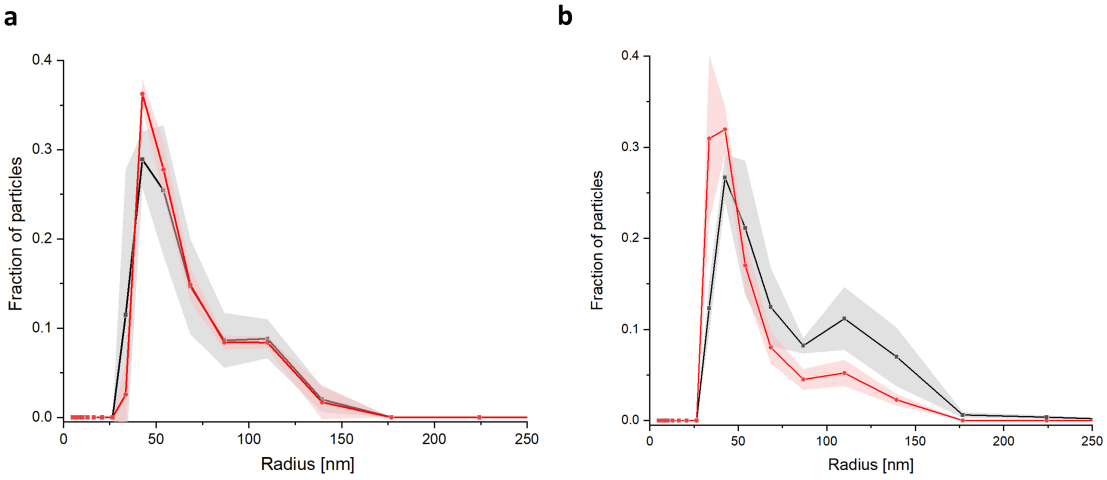


Figure 23: Size measurement of LUVs via DLS. a: Fraction of particles versus radius of DOPC LUVs prepared via detergent-free sample preparation directly after preparation (black) and after 5 hours at 4°C (red). **b:** Fraction of particles versus radius of DOPC LUVs prepared via detergent-mediated sample preparation directly after preparation (black) and after 5 hours at 4°C (red). Shown for each measurement are the mean values of three different DLS experiments with the standard deviation as error band.

Both preparation methods yielded not significantly changed size distributions. The detergent-free formation resulted in an average LUV radius of $r_{avg} = 60 \pm 6$ nm, while detergent-mediated formation led to an average LUV radius of $r_{avg} = 67 \pm 6$ nm. Incubation times of five hours at 4℃ led in both cases to a small change in the distribution towards smaller LUVs.

Membrane Integrity

To test for the LUVs' ability to retain their cargo, DOPC/BioPE (1:0.01) LUVs were loaded with 15 µM CF and immobilized on a glass surface. The CF fluorescence was then monitored over time (figure 24).

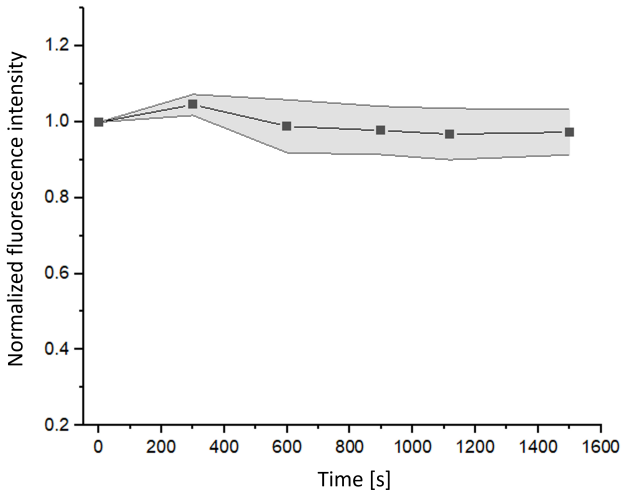


Figure 24: LUV membrane integrity. Normalized fluorescence intensity of DOPC/BioPE (1:0.01) LUVs containing CF immobilized on a glass surface over time. Fluorescence intensity was normalized to the first frame. The mean values from three independent experiments are shown. The standard deviation is depicted by an error band.

As shown in figure 24, the fluorescence intensity of CF contained in the LUVs did not drop significantly over a time of 25 minutes, indicating that no major leakage was occurring over this time period.

Lamellarity

To check for the lamellarity of the produced LUVs, the fluorescent lipid NBD-PE was inserted in the membrane to perform a dithionite-quenching assay, as already previously described. The fluorescence intensity in dependence of time was plotted and is shown in figure 25.

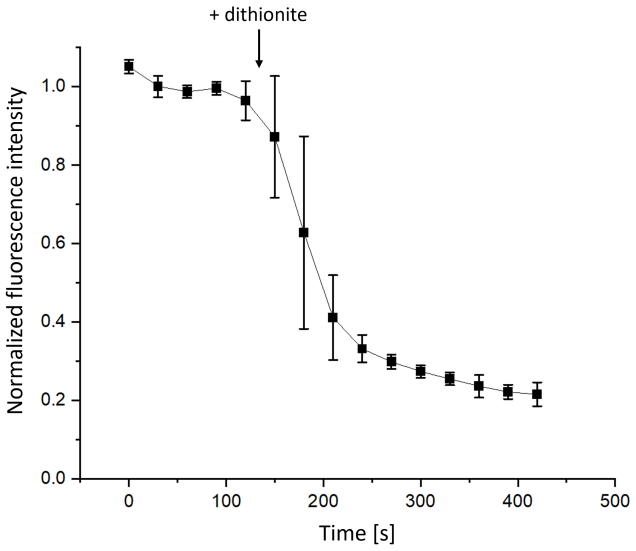


Figure 25: Dithionite quenching of surface-immobilized LUVs. Normalized mean fluorescence intensity of NBD-PE before and after dithionite addition onto surface-immobilized *E. coli* PL/POPC/BioPE LUVs (3:1:0.01). Values were normalized to the average of the frames measured before dithionite addition. The average of three independent measurements is shown with the standard deviation depicted as error.

The measurement resulted in a fluorescence quenching of about 70%, which is even higher than the 50% expected for complete unilamellarity. This could be attributed to a slight surface asymmetry of the outer and inner leaflet, which becomes more pronounced for smaller vesicles. For an LUV with 100 nm in diameter, a bilayer thickness of 4.5 nm and a lipid headgroup area of 0.68 nm^2, the outer leaflet would be expected to contain about 55% of all lipids in the vesicle. Therefore, it is more probable that the drop was additionally caused by lipid residues on the glass surface not belonging to intact LUVs. Although the exact percentage of unilamellar vesicles cannot be determined, the results indicated a high percentage of unilamellar vesicles.

Establishing a membrane potential

Similar to previous experiments performed for GUVs, the import of the Nernstian dye safranin was monitored via fluorescence microscopy for LUVs [5]. As LUVs exhibit sizes below the resolution limit of confocal microscopy, it is impossible to distinguish between the fluorescence originating from membrane-inserted safranin and the safranin imported into the LUV lumen via confocal imaging. Still, the increase in overall fluorescence intensity could be monitored upon addition of valinomycin. The results are depicted in figure 26. Washing the immobilized LUVs resulted in a steeper ion gradient than diluting the GUVs. Under the used experimental conditions, the theoretically attainable membrane potential was −208 mV.

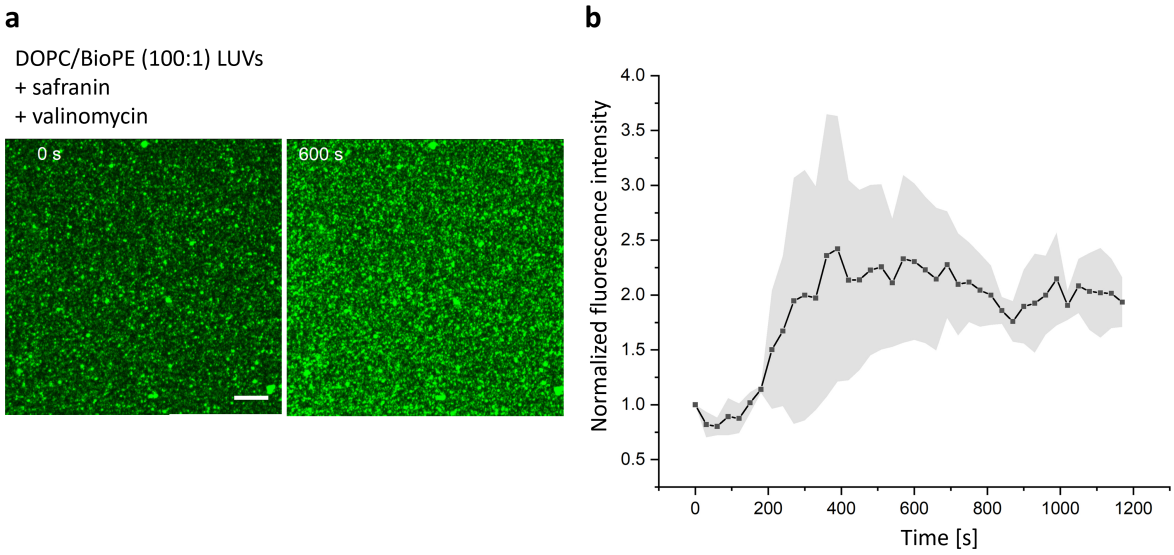


Figure 26: Membrane potential establishment. a: Surface-immobilized DOPC/BioPE (100:1) LUVs, exhibiting a potassium gradient towards the vesicle environment, treated with 6 µM safranin after addition of 5 µM valinomycin. The scale bar is 5 µm. **b:** Normalized fluorescence intensity of safranin in surface-immobilized LUVs, produced with a potassium gradient towards the vesicle environment, after valinomycin addition.

As visible in figure 26, the fluorescence intensity increased over time upon addition of 5 µM valinomycin and finally reached a plateau after about 400 s. This indicated that the membrane potential was fully developed after this time period.

This concludes the characterization of the formed LUVs and GUVs. Returning again to the previously presented conditions, it can be appreciated that both systems represent an appropriate model system to assess the biological questions at hand.

2.1.3 Vesicle fusion

After membrane system development was finished, vesicle fusion was explored to deliver cargo from one vesicle to the other. Charge-mediated vesicle fusion is a process by which donor vesicles merge with target membranes. This process is relevant as a drug delivery mechanism and can be used to mimic membrane transport. The fusion is driven by electrostatic interactions, specifically interactions between oppositely charged lipid headgroups. This reduces the distance between bilayers until fusion can occur [44]. The fusion is schematically depicted in figure 27a.

Electrostatic vesicle fusion of LUVs to GUVs was presented by Lira *et al.* in 2019 [44], who initiated fusion by combining two vesicle species: One species contained the positively charged lipid DOTAP, the other contained the negatively charged lipid PG.

Here, electrostatic vesicle fusion for LUV-LUV fusion was tested. In two seperate experiments lipid mixing, as well as lumen mixing, were investigated. The results are depicted in figure 27b.

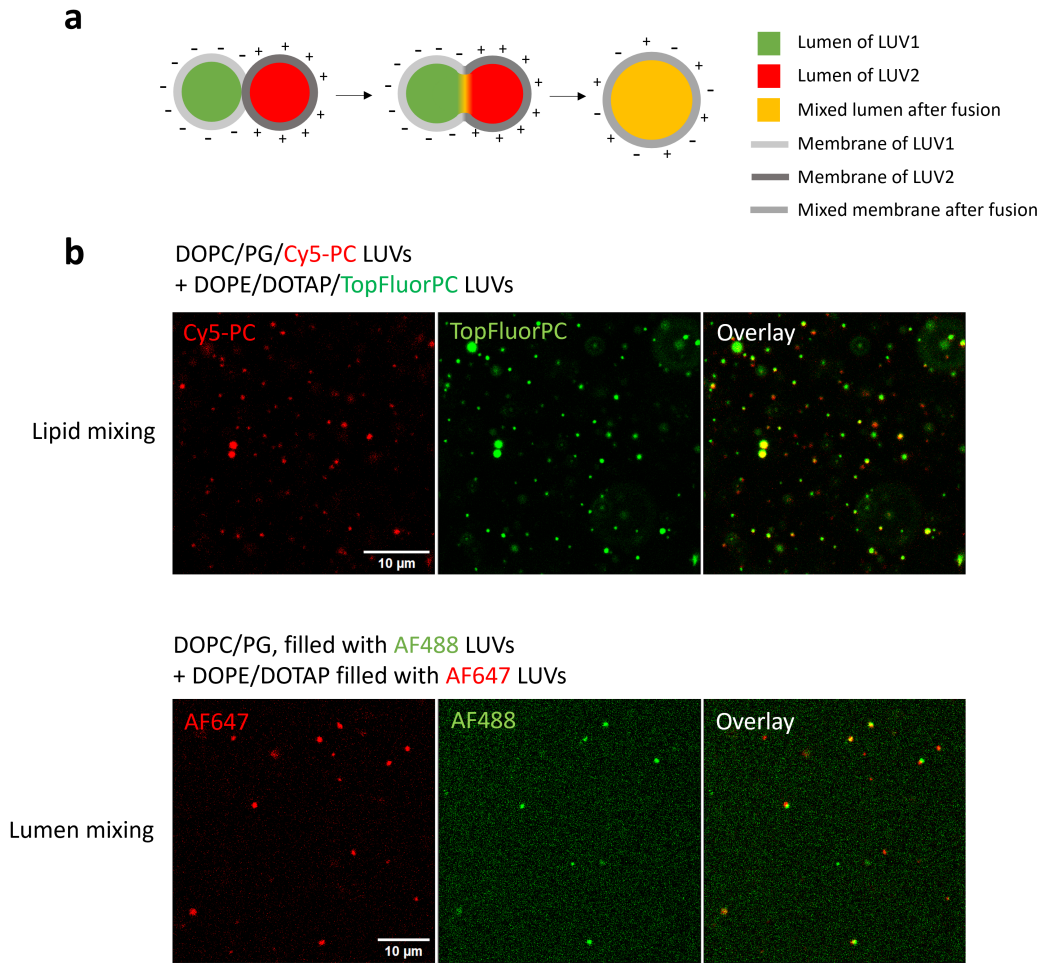


Figure 27: LUV-LUV fusion leading to lipid and lumen mixing. **a:** Charge-mediated fusion shown schematically. **b:** Lipid mixing: DOPC/PG/Cy5-PC (10:1:0.1) and DOPE/DOTAP/TopFluorPC (1:1:0.1) LUVs were incubated together for 10 minutes and finally immobilized via agarose. The composite image demonstrates the overlay of both fluorophores. Lumen mixing: POPC/PG (10:1) LUVs, filled with 10 µM AF488 and DOPE/DOTAP (1:1) LUVs filled with 10 µM AF647 were incubated together for 10 minutes and finally immobilized via agarose. The composite image demonstrates the overlay of both fluorophores.

In the first experiment, the fluorescent lipid TopFluorPC was inserted into the positively charged DOPE/DOTAP/TopFluor PC (10:1:0.1) LUVs, while the fluorescent lipid Cy5-PC was inserted into negatively charged POPC/PG/Cy5-PC (10:1:0.1) LUVs. The vesicle species were combined and incubated for 10 minutes, before they were immobilized in agarose. The agarose-immobilized vesicles were imaged and an overlay of the Cy5-PC and the TopFluorPC channel showed LUVs of mixed lipid composition. In the next experiment, lumen content mixing was studied. Therefore, the vesicle lumen of the positively charged LUVs was loaded with 10 µM AF647, while the negatively

charged LUV lumen was loaded with 10 µM AF488. Again, the two vesicle species were combined and then after a short incubation time immobilized in agarose. After fusion, the vesicles demonstrated a mixed lumen content.

2.2 Construction of a two-color smFRET microscope from a single-channel setup

In order to investigate nanoscale distance changes, which lie beyond the scope of optical resolution, Förster Resonance Energy Transfer (FRET) was implemented. FRET is an important technique to study protein function and dynamics. It is defined as a non-radiative energy transfer between two chromophores which increases with reduced distance between the two chromophores [19]. FRET measurements can be performed as ensemble measurements in solutions, taking advantage of the high number of molecules in the field of view. These measurements provide a good detection method for general trends. However, molecular heterogeneity or subpopulations are averaged out. Single-molecule FRET (smFRET), on the other hand, allows direct observation of individual molecules, revealing heterogeneous states, dynamic transitions, and rare conformations that ensemble methods cannot resolve [23].

To gain an important microscopy tool in assessing protein interactions on a single-molecule level, single molecule (sm) Förster resonance energy transfer (FRET) measurements were employed in this work. Therefore, an already existing sm total internal reflection fluorescence (TIRF) setup, which was built by Dr. Jan Ruland, was amended to perform simultaneous acquisition of two emission channels [80]. An Optosplit II (Cairn GmbH, Heidelberg) was equipped with suitable filtersets and added right before a scientific complementary metal-oxide-semiconductor (sCMOS) camera to achieve that. The modified setup is schematically depicted in figure 28. The filter sets were chosen to be suitable for donor fluorophores that can be excited at 561 nm and acceptor fluorophores that can be excited with 638 nm wavelength light. The system could additionally be used for alternating-laser excitation (ALEX) FRET. ALEX broadens the possibilities of smFRET, by introducing a new parameter for evaluation [32]. This can be accomplished by not only exciting with the donor excitation wavelength, but also alternately exciting with the acceptor excitation wavelength. For ALEX smFRET, the stoichiometry S can be extracted alongside the FRET efficiency E. S serves as an indicator of the donor-to-acceptor ratio.

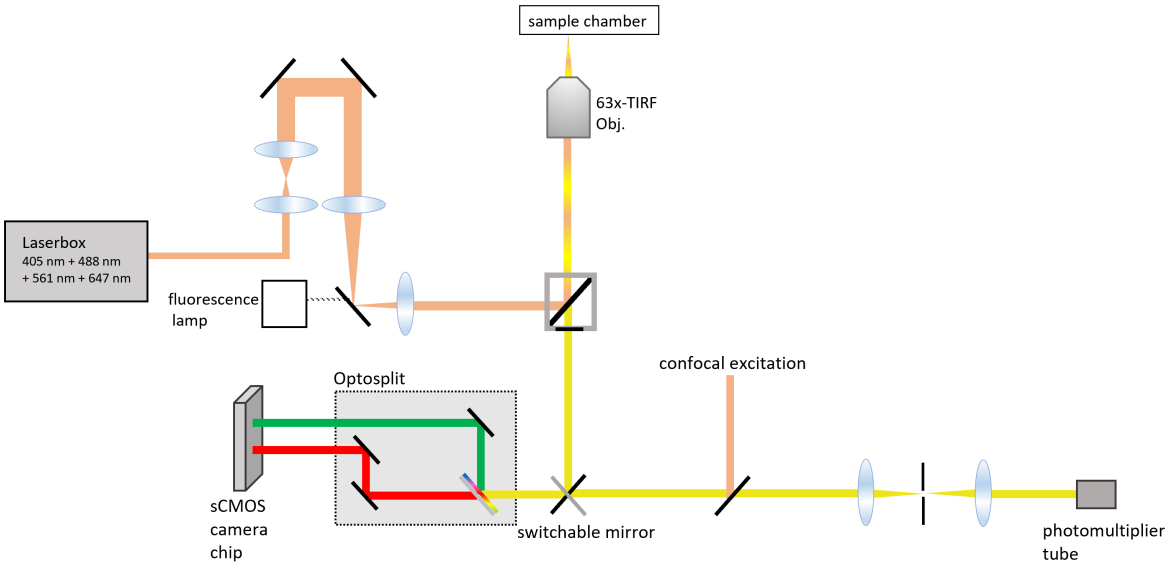


Figure 28: Dual-color smFRET TIRF setup. Schematic representation of a two-channel single-molecule TIRF microscope setup. The orange lines indicate excitation light, while the yellow lines show emission light.

2.2.1 FRET evaluation

The absolute FRET efficiency E represents the fraction of donor excitation transferred to the acceptor, corrected for donor leakage α (fraction of donor fluorescence that is detected in the acceptor channel due to spectral overlap), direct acceptor excitation δ (acceptor fluorescence that arises from direct excitation by the donor excitation laser) and the detection factor γ (accounts for differences in detection efficiency and quantum yield between donor and acceptor fluorophores) [26]. The FRET efficiency E increases upon distance reduction between donor and acceptor fluorophores. The following nomenclature is used throughout this work with emission (em.), excitation (ex.), acceptor (A) and donor (D).

	A ex. (638 nm)	D ex. (561 nm)
A em. (>650 nm)	A_A	A_D
D em. (570-620 nm)	D_A	D_D

Then, the **absolute FRET efficiency** E is defined as:

$$E = \frac{(A_D - \alpha D_D - \delta A_A)}{(A_D - \alpha D_D - \delta A_A) + \gamma D_D} \tag{3}$$

Often determination of the correction factors α, δ and γ is difficult and errors can lead to data distortion [26]. Therefore, approximations are made. If $\gamma = 1$ is assumed, the **corrected FRET efficiency** E' is calculated. If $\gamma = 1$ and $\alpha = \delta = 0$ is assumed, the

so called **raw FRET efficiency** E'' is calculated. Only the absolute FRET efficiency E can be used for a quantitative distance measurement. However, the raw and the corrected FRET efficiencies E' and E'' are often used for relative fluorophore distance comparisons [26].

If ALEX FRET is performed, the **stoichiometry** S can be calculated as follows:

$$S = \frac{D_D + (A_D - \alpha D_D - \delta A_A)}{D_D + (A_D - \alpha D_D - \delta A_A) + \gamma A_A} \tag{4}$$

Assuming $\gamma = 1$ leads to the calculation of the **corrected stoichiometry** S', while assuming $\gamma = 1$ and $\alpha = \delta = 0$ results in the **raw stoichiometry** S''.

2.2.2 smFRET control measurements

To test the smFRET setup, three different annealed DNA oligomer samples with distinct donor-acceptor distances were examined. The DNA oligomers used here were commercially synthesized (Microsynth Seqlab GmbH, Göttingen) corresponding to those used in a multi-laboratory smFRET benchmark study by Hellenkamp *et al.*, 2018 [25]. A biotinylated DNA strand, carrying the dye Atto647N, was combined with different single strands, labeled with Atto550 in different positions. After annealing, the biotinylated DNA was fixed on BioBSA-NAv coated glass cover slips. This sample was then imaged via smFRET and evaluated via the software iSMS [73]. The results are shown as FRET efficiency histograms in figure 29.

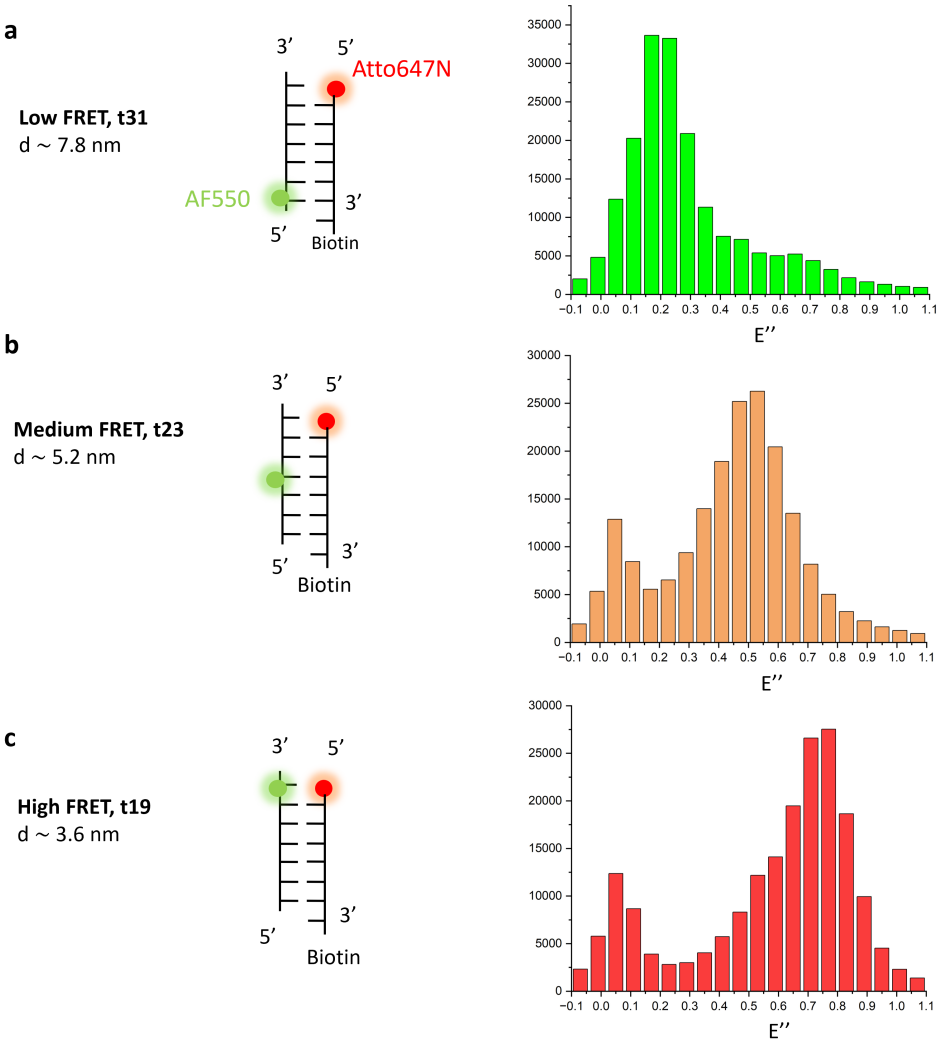


Figure 29: smFRET calibration using DNA samples. Histograms of the raw FRET efficiency for a low FRET sample (green), a medium FRET sample (orange) and a high FRET sample (red). On the left side is a schematic depiction of the respective oligomers. **a:** Low FRET annealed oligonucleotid sample, acceptor strand carrying Atto647N at thymidine 31 and donor strand carrying Atto550 at thymidine 31. **b:** Medium FRET annealed oligonucleotid sample, acceptor strand carrying Atto647N at thymidine 31 and donor strand carrying Atto550 at thymidine 23. **c:** High FRET annealed oligonucleotid sample, acceptor strand carrying Atto647N at thymidine 31 and donor strand carrying Atto550 at thymidine 19.

The histograms for the medium and high FRET sample exhibit two distinct peaks. In the low FRET sample only one distinct peak is visible, although the two peaks might not be distinguishable due to their overlay. The lower FRET efficiency populations possibly originated from unspecifically adsorbed donor-only strands, as donor emission tends to bleed-through into the FRET channel, which can result in apparent FRET signals that are evaluated by iSMS [73]. The higher FRET efficiency populations likely correspond to donor-acceptor double strands and change for the high, medium, and low FRET samples. This indicates that even small changes in distances between donor and acceptor molecules could be detected successfully.

This concludes the methodological developments of this thesis, providing all the required tools to integrate the advanced microscopy techniques with the model membrane systems to study the two membrane transport systems of interest.

2.3 Functional analysis of membrane transporter proteins

2.3.1 The Lipid II flippase

Despite its pivotal role in cell wall biosynthesis, the identity of the lipid II flippase remains under discussion. Goal of this part of the thesis was to test the three putative lipid II flippases RodA, FtsW and MurJ on their lipid II flipping activity in artificial membranes in presence and absence of a membrane potential. Successful membrane protein reconstitution of all three proteins, as well as successful membrane potential establishment, has been demonstrated in the previous subsections.

A sodium dithionite quenching assay was employed to assess lipid II orientation. As a prerequisite, lipid II-NBD had to be synthesized. The primary amine of L-lysine at the lipid II headgroup enabled labeling via NBD-N-hydroxysuccinimide (NHS) ester. Thin layer chromatography (TLC) was used to check for successful labeling. Lipid II containing bands turned blue after phosphomolybdic acid (PMA) treatment. Therefore, lipid II-NBD was identified as the band in which NBD and PMA bands overlayed.

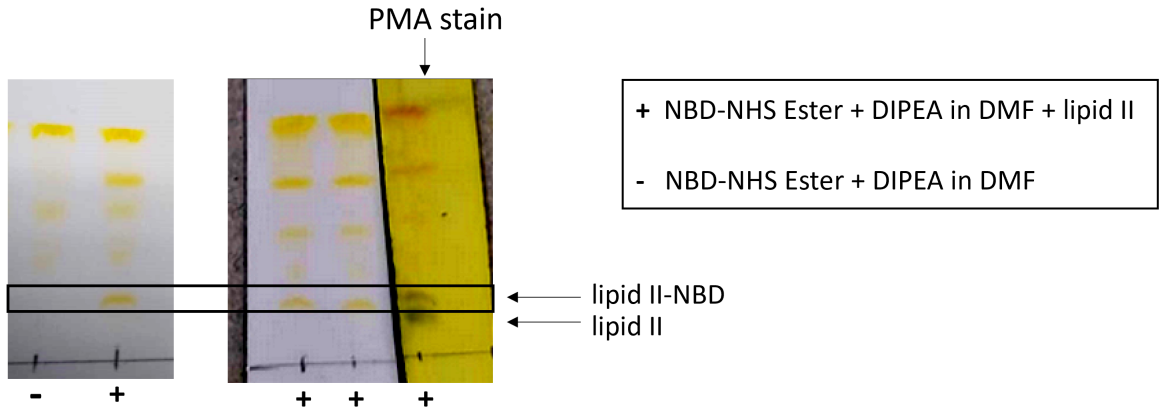


Figure 30: Lipid II-NBD synthesis. Silica gel imaged under white light. (+) indicates that a solution of lipid II, NBD-NHS ester and diisopropylethylamine (DIPEA), solved in dimethylformamide (DMF) was added onto the silica gel, (-) indicates that a solution of only NBD NHS ester and DIPEA, solved in DMF was added. On the right hand side a PMA stained TLC can be seen. Bands that contain lipid II exhibit a blue color.

After identification of the correct band, lipid II-NBD was purified from the silica gel. In the following, DOPC/cholesterol (chol)/BioPE/lipid II-NBD (10:1:0.1:0.014) LUVs were prepared. A solution of 150 mM KCl buffer/10 mM Na_2HPO_4 pH 7.8 was used as hydration buffer.

MurJ, FtsW or RodA were reconstituted into the LUV membrane in a protein to lipid ratio of 1:2500. The proteo-LUVs could then be immobilized onto a pre-treated glass surface, as described before, and washed with 150 mM NaCl/10 mM Na_2HPO_4 pH 7.8. Due to the, thereby, created potassium gradient, a membrane potential could

be established by addition of 5 µM valinomycin. After dithionite addition, a steep decrease in fluorescence intensity was visible for all measured conditions. Exemplary normalized measurements are shown in figure 31.

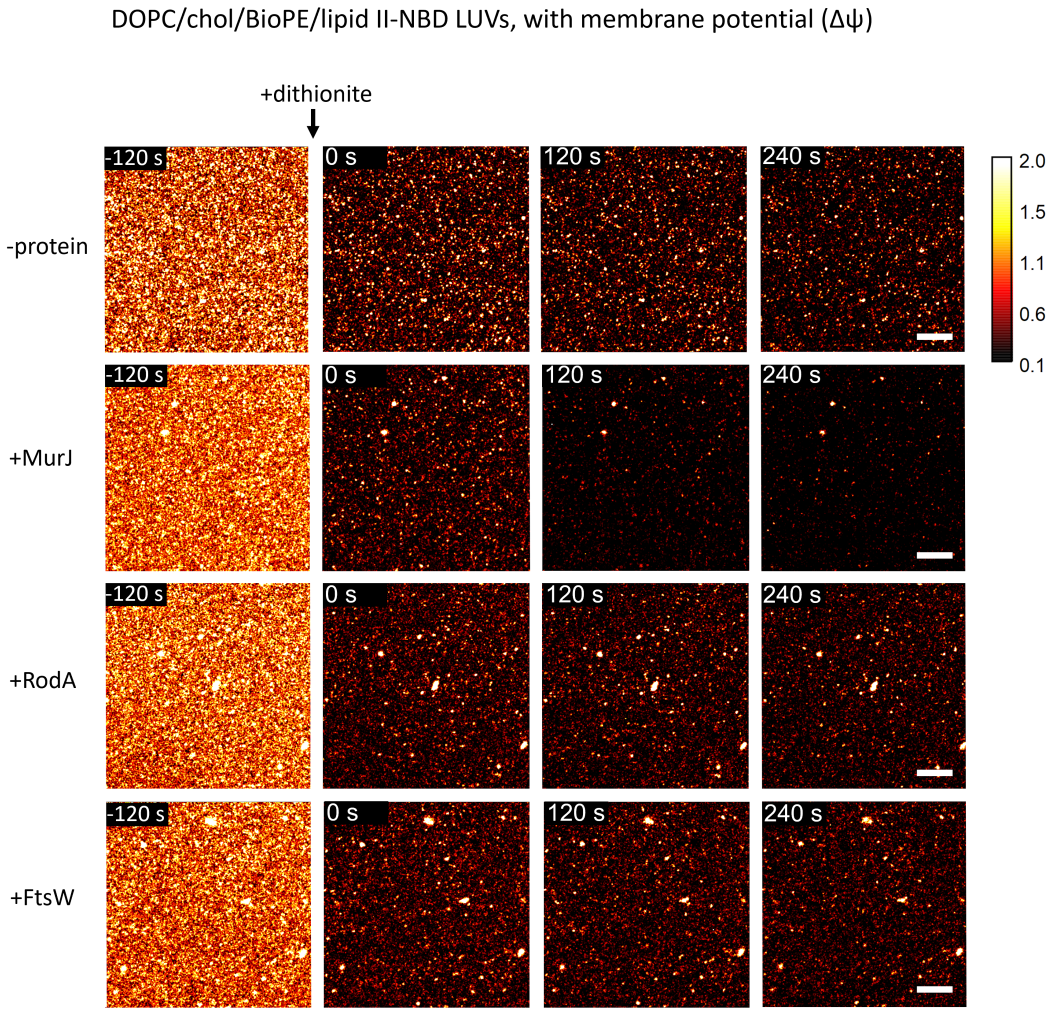


Figure 31: Time series of dithionite quenching of LUVs with no protein, MurJ, RodA and FtsW reconstituted. Images are normalized to the mean lipid II-NBD fluorescence intensity value of the first frame of each respective measurement and displayed using the lookup table "Red Hot" of Fiji [83]. Dithionite was added as indicated. The calibration bar for all time series is depicted on the right hand side. The shown scale bar has a length of 10 µm.

The normalized lipid II-NBD fluorescence intensity of three independent measurements for every protein in membrane potential absence and presence was averaged and plotted in dependence of the time. The respective graphs are shown in figure 32.

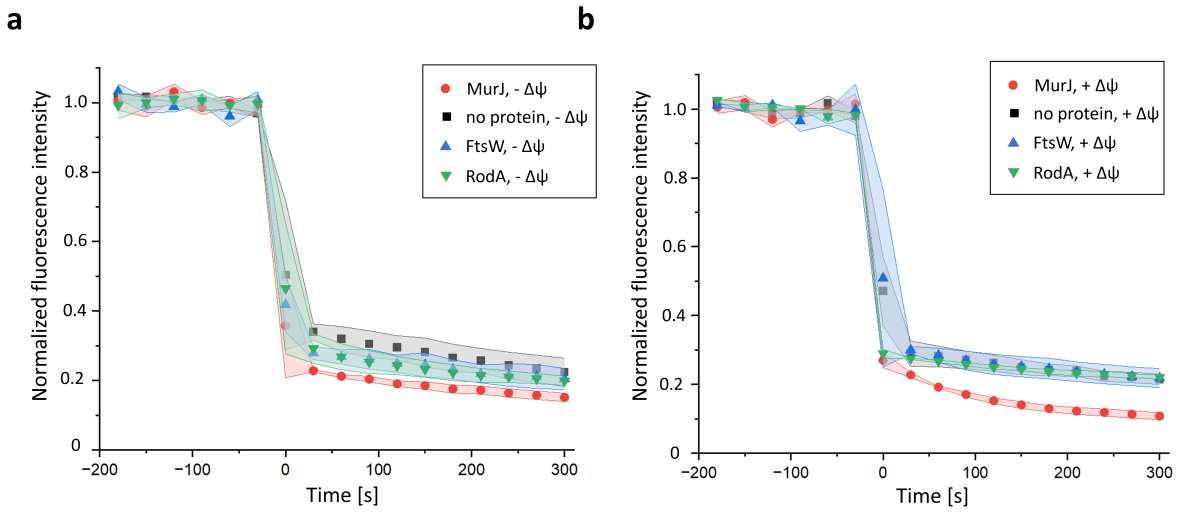


Figure 32: Flipping of lipid II-NBD. Normalized mean fluorescence intensity of lipid II-NBD in DOPC/chol/BioPE/lipid II-NBD (10:1:0.1:0.014) LUVs upon reconstitution of MurJ, RodA and FtsW. Sodium dithionite was added in the time interval between -30 s and 0 s. The data points represent the average of three independent measurements. The standard deviation is depicted as error bar. **a:** In absence of a membrane potential. **b:** In presence of membrane potential.

First, a set of measurements was acquired without a membrane potential (figure 32a). All measured LUVs showed a steep decrease in NBD fluorescence intensity upon dithionite addition before they reached a plateau with a small linear decay. This decay could possibly be caused by bleaching due to the laser excitation used for the image acquisition. The decrease in fluorescence intensity was strongest for MurJ containing LUVs, while RodA or FtsW containing LUVs did not show significant differences to the LUVs without reconstituted proteins.
For the next set of measurements, a membrane potential was established by valinomycin addition (figure 32b). The samples were incubated with valinomycin for 15 minutes before the experiment was performed to allow for a complete build-up of the membrane potential. Interestingly, in the presence of a membrane potential, the sample containing MurJ did not transition to a linear decay after the steep decrease, but decayed first with a steeper slope than the other measured samples. After about 200 s, the slope decreased and approached the slope of the other measured samples. LUVs, containing MurJ, exhibited again the smallest protected fraction, while RodA or FtsW containing LUVs did not differ significantly from LUVs without reconstituted proteins.

To test if MurJ activity could be inhibited, two known MurJ inhibitors were added to the sample for the next experiment (figure 33). The inhibitors 2-(2-Chlorophenyl)-3-[1-(2,3-dimethylbenzyl)piperidin-4-yl]-5-fluoro-indole (CDFI) and Compound D (ComD) [59] [30] were provided by Dr. Anna Müller from the Institute of Pharmaceutical Microbiology (University of Bonn). The inhibitors were added in a concentration of

10 µM before valinomycin incubation was started.

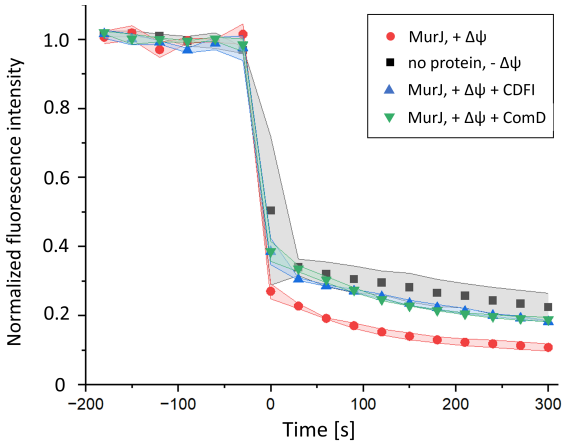


Figure 33: Influence of MurJ inhibitors on flippase activity. Normalized mean fluorescence intensity of lipid II-NBD in DOPC/chol/BioPE/lipid II-NBD (10:1:0.1:0.014) LUVs under different conditions. Sodium dithionite was added in the time interval between -30 s and 0 s. The data points represent the average of three independent measurements. The standard deviation is depicted as error bar.

Inhibitor presence of either one of the inhibitors increased the protected fraction of lipid II-NBD in MurJ containing LUVs, indicating successful inhibition.
To summarize the results of the experiments shown in figures 33 and 32, the final points of each of the three measurements performed for each condition were plotted as a column diagram. The column diagram is shown in figure 34.

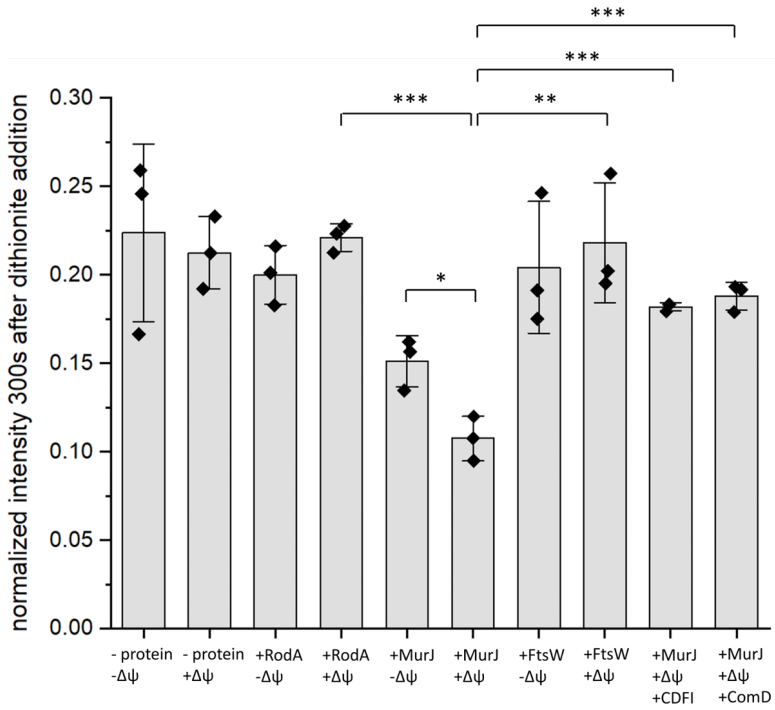


Figure 34: Protected lipid II-NBD fractions. The final points of three independent measurements showing the normalized fluorescence intensity 300 s after dithionite addition are plotted as a column diagram with error bars giving the standard deviation. The significance was tested via an unpaired Student t-test and is indicated on top of the column (*p<0.05, **p<0.01, ***p<0.001).

The data points demonstrate that all LUVs, except the ones containing MurJ, reach a value of about 20% to 25% of their original fluorescence intensity 300 s after dithionite was added. Even without a membrane potential, MurJ containing LUVs already exhibited a significantly lower protected fraction than all other conditions. This value reduced again significantly in presence of a membrane potential. However, MurJ-containing vesicles that were treated with the inhibitors CDFI and ComD exhibited protected fractions close to the samples which did not contain MurJ.

2.3.2 TRAP transporters

TRAP transporters utilize an SBP-dependent secondary active transport mechanism to import hydrophilic substrates [70]. The import is vital for some pathogens' ability to evade immune response [33]. Goal of this part of the thesis was to observe the import process directly via fluorescence microscopy in model membrane systems to gain a better understanding of the import mechanism and to test how the import is influenced by environmental parameters as well as certain protein mutations.

The SBP as Neu5Ac sensor

A requirement for a successful fluorescence based import assay was the use of a sensor that recognizes Neu5Ac with a high affinity. The SBP's ability to scavenge Neu5Ac from the periplasm could be utilized for this purpose. The import process is depicted schematically in gray scale in figure 35. The respective step is shown in color.

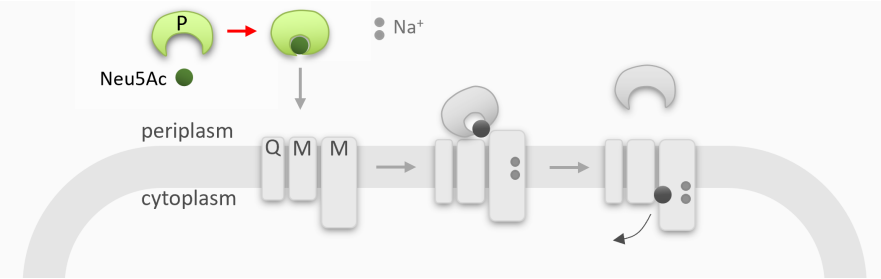


Figure 35: TRAP-transporter mechanism. Schematic depiction of key steps of the proposed Neu5Ac import by SiaPQM with colored highlight on the binding of the Neu5Ac by the SBP. Image based on [70].

The SBP remains in an open state without a substrate [69]. When substrate is present, the SBP closes around it, thereby bringing its two globular domains closer to each other [70] [69]. This conformational change could be detected by FRET in two different ways.

(1) **Intraprotein labeling**: SiaP from *V. cholerae* (VcSiaP) was modified via intraprotein labeling, meaning donor and acceptor were attached each to one globular domain of VcSiaP [69]. A scheme is shown in figure 36a.

(2) **Interprotein labeling**: A $\mathrm{Nb}_{P_{closed}}$, specifically binding only closed HiSiaP, enabled these experiments. The acceptor molecule was bound to $\mathrm{Nb}_{P_{closed}}$, while the donor was conjuagated to HiSiaP. The conformational change of HiSiaP, triggered by Neu5Ac binding, then resulted in binding of $\mathrm{Nb}_{P_{closed}}$ to HiSiaP. A scheme is shown in figure 36b.

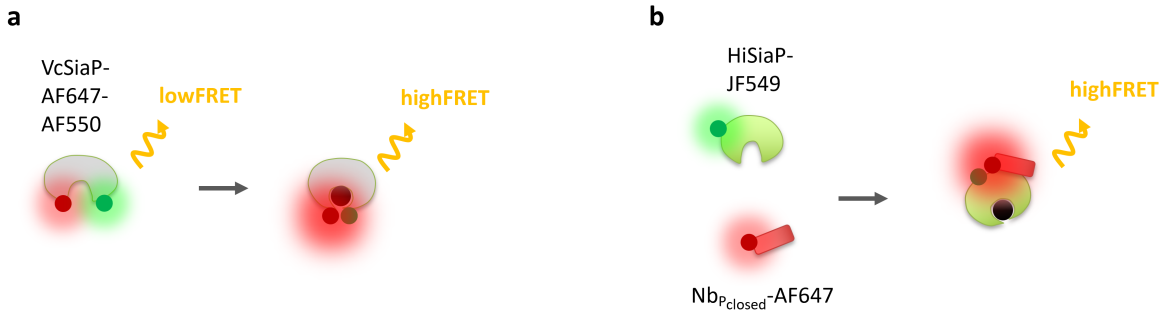


Figure 36: Neu5Ac detection by FRET via two labeling approaches. a: Intraprotein labeling approach (1), **b:** Interprotein labeling approach (2).

Both approaches exploit the fact that Neu5Ac presence leads to a distance reduction between donor and acceptor dye. Therefore, both systems can detect Neu5Ac by increasing in FRET efficiency. This was tested via ensemble FRET in solution by adding either VcSiaP-AF555-AF647 or $Nb_{P_{closed}}$-AF647 and HiSiaP-JF549 into a solution and measuring the raw FRET efficiency E''. After this, Neu5Ac was added to the respective solutions and E'' was measured again. The resulting data is depicted in figure 37.

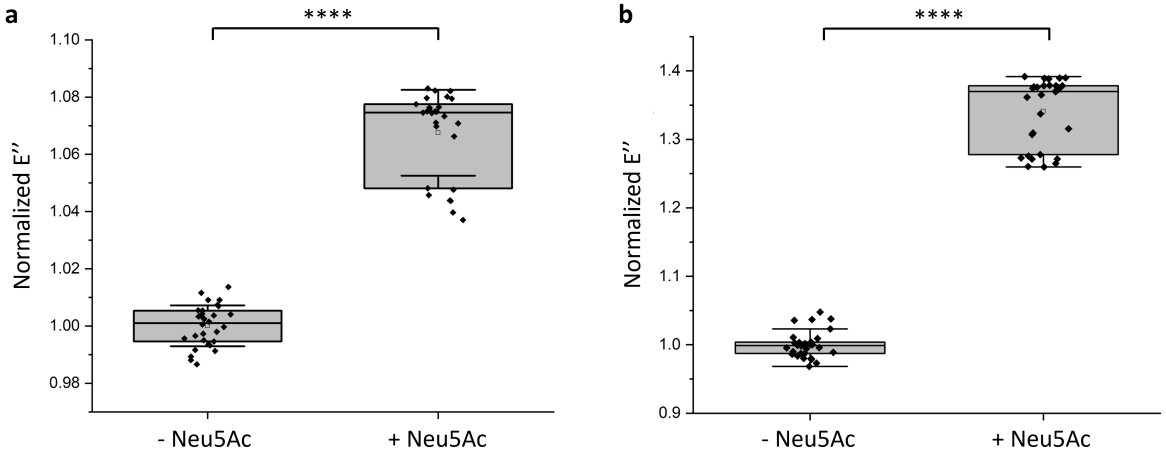


Figure 37: Neu5Ac FRET sensor systems. a: Boxplot diagram of the normalized E'' of a solution of 60 nM VcSiaP-AF555-AF647 without and with 3.5 µM Neu5Ac addition. **b:** Boxplot diagram of the normalized E'' of a solution of 60 nM HiSiaP-JF549 and 60 nM $Nb_{P_{closed}}$-AF647 without and with 3.5 µM Neu5Ac addition. Three independent measurements were performed for each condition. The significance was tested via an unpaired Student t-test and is indicated on top of the column (****p<0.0001).

As shown in figure 37, both labeling strategies were able to detect the presence of Neu5Ac. While the intramolecular labeling approach resulted in a normalized E'' increase of about 6.7 ± 1.5%, the intermolecular labeling resulted in an increase of 34.1 ± 4.8%.

In the next step, the binding affinity of VcSiaP for Neu5Ac was determined. To do so, Neu5Ac was added stepwise to a 60 nM VcSiaP-AF555-AF647 solution until complete saturation was reached. The raw FRET efficiency E'' was measured for each stepwise addition to derive the fraction of VcSiaP-AF555-AF647 that closed around substrate (ϑ):

$$\vartheta(E'') = \frac{E'' - E''_0}{E''_{max} - E''_0} \tag{5}$$

with E''_0 representing the raw FRET efficiency without Neu5Ac and E''_{max} representing the raw FRET efficiency with Neu5Ac saturation.

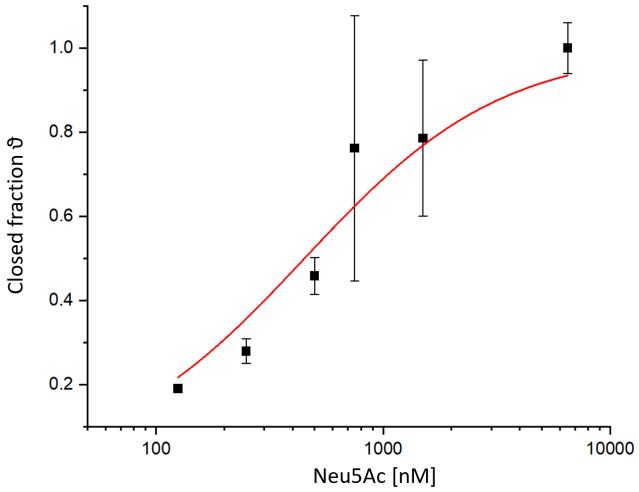


Figure 38: Affinity of VcSiaP for Neu5Ac. Plot of the closed fraction of VcSiaP against the Neu5Ac concentration on a logarithmic scale. The data was fitted with a saturation function (eq. 6), shown in red.

The closed fraction increased with increasing Neu5Ac concentration until a plateau was reached. The data was fitted with the following equation to determine the binding affinity k_D, as described by Peter *et al.*, 2021 [69].

$$y = \frac{x}{x + k_D} \tag{6}$$

The binding affinity was determined from the fit parameter as $k_D = 450 \pm 180$ nM.

Single molecule interaction studies of HiSiaQM and HiSiaP on surface-immobilized LUVs

The next step was to investigate the binding of HiSiaP to HiSiaQM as the subsequent part of the overall import. HiSiaP-QM complex formation and substrate transfer is highlighted in figure 39.

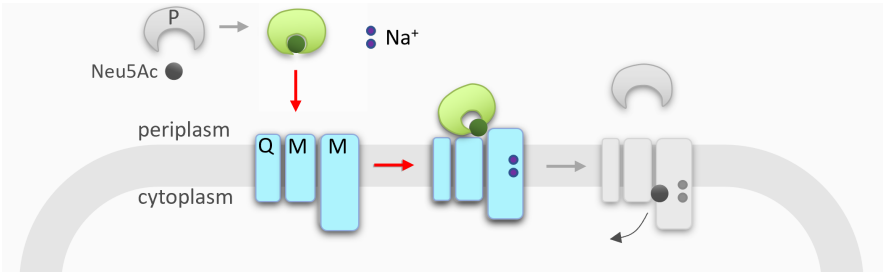


Figure 39: TRAP-transporter mechanism. Schematic depiction of key steps of the proposed Neu5Ac import by SiaPQM with coloured highlight on the interaction of the SBP with the membrane-inserted QM domain. Based on [70].

Total internal reflection fluorescence (TIRF) single-molecule microscopy was used to observe HiSiaP-AF647's interaction with HiSiaQM. This enabled us to study the impact of substrate presence, a sodium gradient gradient and a membrane potential on the complex formation. HiSiaQM was reconstituted in surface-immobilized DOPC/BioPE/ TopFluor PC (100:1:0.1) LUVs. This allowed us to deposit different solutions in- and outside of the LUVs. TIRF illumination created an evanescent field that extended only few hundred nanometers into the sample. Only fluorophores within this distance to the coverslip surface could be excited. The illumination depth of the evanescent field is with about 50 to 300 nm similar to the average LUV size [18]. Hence, added HiSiaP-AF647 was selectively detected when it interacted with the surface-immobilized LUVs, as free diffusing proteins left the evanescent field quickly. Using the Stokes-Einstein equation and approximating a Stokes radius of 2.7 nm, HiSiaP would exhibit a root-mean square displacement of about 2.2 µm/10 ms at 20°C. A schematic overview of the measurements is depicted in figure 40.

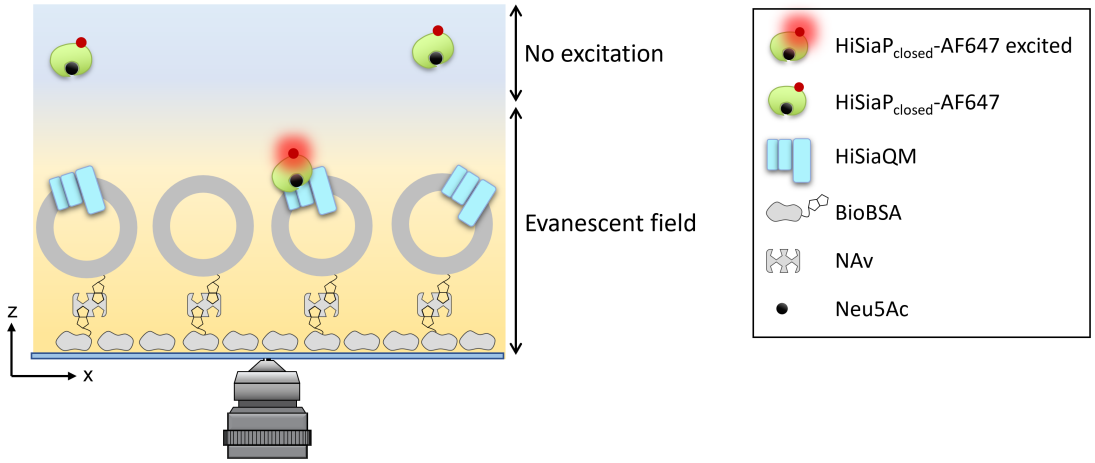


Figure 40: HiSiaP-QM complex formation, visualized via single-molecule TIRF microscopy in xz-projection. TIRF illumination enables selective excitation of HiSiaP-AF647 interacting with surface-immobilized LUVs.

Different conditions were tested for their influence on the binding behaviour of HiSiaP to HiSiaQM. As the import mechanism relies on the existence of a sodium gradient [61], the binding was measured in presence and absence of a sodium gradient, as well as in presence and absence of sodium itself. To establish this, a sodium chloride buffer (150 mM NaCl/5 mM HEPES, pH 7.2) and a potassium chloride buffer (150 mM KCl/5 mM HEPES, pH 7.2) were used. In the following, the potassium chloride buffer will be abbreviated with K, while the sodium chloride buffer will be abbreviated with Na. Furthermore, the effect of a membrane potential was tested, which could be generated by the addition of valinomycin, if an ion gradient was present. Also of interest was the effect that Neu5Ac presence had on the HiSiaP-HiSiaQM interaction. Finally, different HiSiaQM mutations were investigated as well. HiSiaP-AF647 was

added in a concentration of 2 nM for each measurement. Exemplary single-molecule measurements are depicted in figure 41.

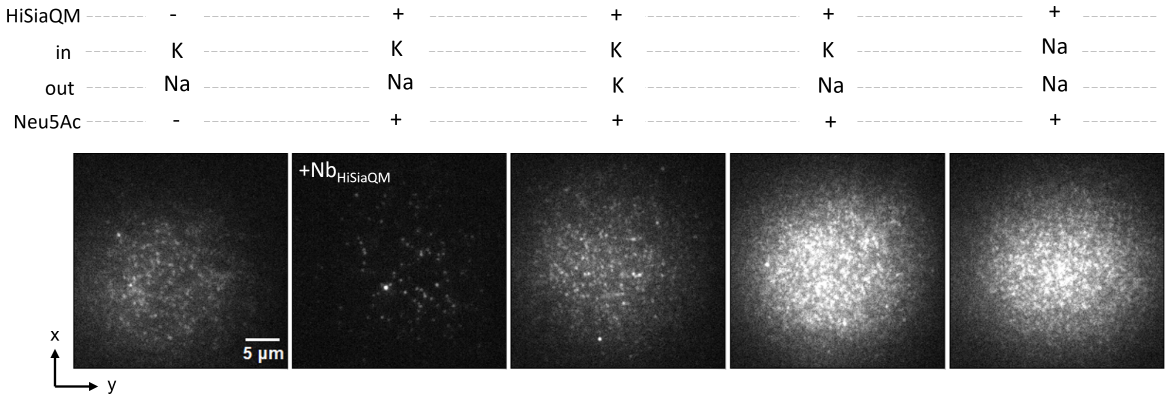


Figure 41: HiSiaP-QM complex formation, visualized via single-molecule TIRF microscopy. HiSiaP-AF647 on surface-immobilized DOPC/BioPE/TopFluor PC (100:1:0.1) LUVs. Different conditions are indicated above each image. All images show frame 5/1000 of each respective measurement.

To quantify the amount of interactions, the single-molecule data was tracked via the Fiji plugin TrackMate [95] and the number of tracks per movie was plotted for the different measurement conditions. These are depicted as column diagrams in figure 42.

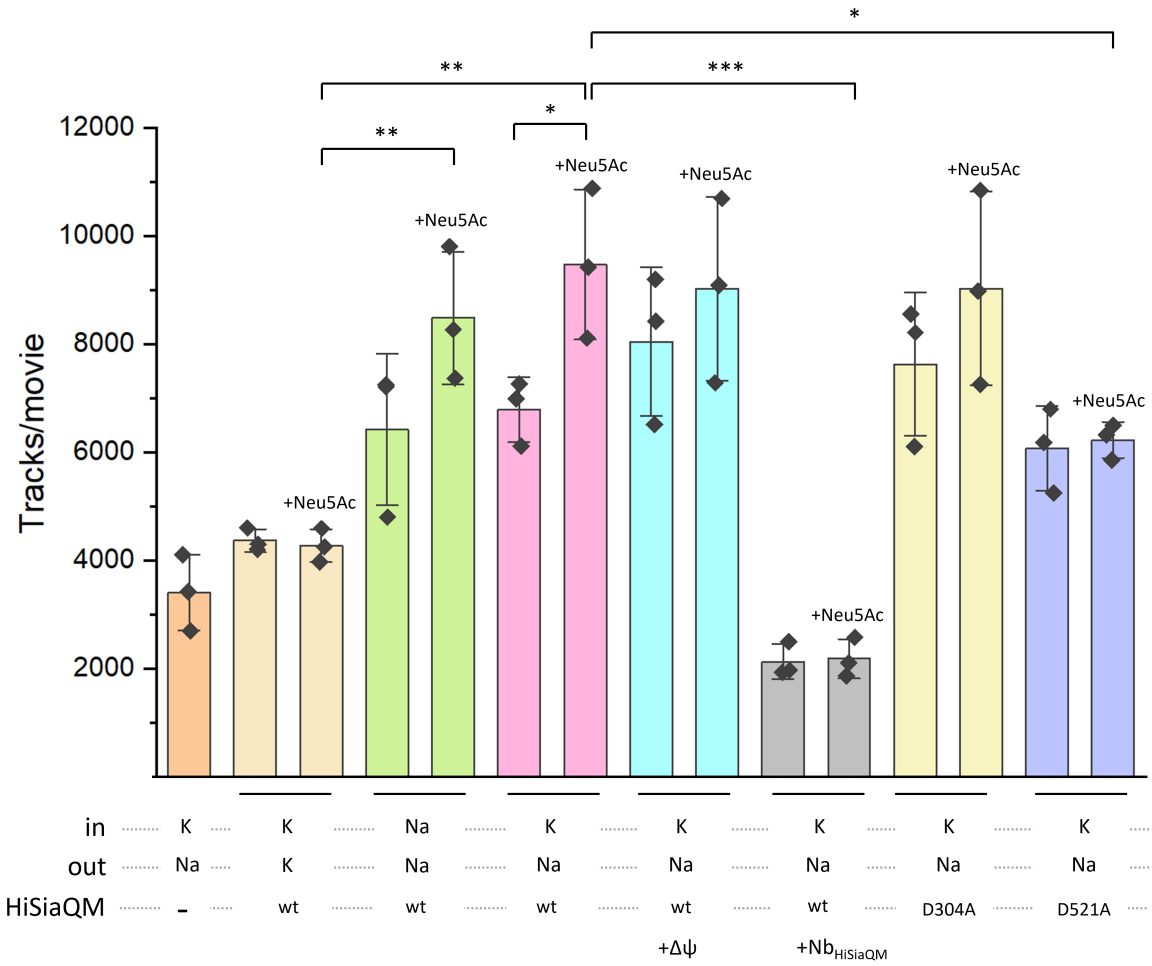


Figure 42: Single-molecule interaction studies of HiSiaQM and HiSiaP on surface-immobilized LUVs. Tracks per movie of HiSiaP-AF647 interacting with DOPC/BioPE/TopFluorPC (1000:10:1) LUVs. Each diamond represents the average of 30 different movies. The columns indicate the mean value of the three measurements. The standard deviation is given as an error bar. The significance was assessed via a Student t-test and is shown on top of the columns (*p<0.05, **p<0.01, ***p<0.001).

First, a baseline was established by measuring the unspecific interactions between HiSiaP-AF647 and LUVs with no HiSiaQM reconstituted. After this value was established, HiSiaQM-containing LUVs were measured in absence of sodium, as K was used on the in- and outside of the vesicles. This resulted in a small increase in binding events, when compared to the baseline measurements. The addition of Neu5Ac resulted in no significant change. In the next step Na was used for the in- and outside of the vesicles. This increased the amount of tracks per movie significantly over the baseline measurement. Here, addition of Neu5Ac resulted in another increase in tracks per movie. For the next measurement, a sodium gradient was established with Na being present on the vesicle outside and K being present on the inside. The tracks per movie showed no significant change in comparison to the measurements with only Na present. Also here, addition of Neu5Ac resulted in an increased tracks/movie value, when compared to the measurement without Neu5Ac. In the next step, additionally

to the sodium gradient, also a membrane potential $\Delta\psi$ was established upon addition of valinomycin to the sample. Measurements were started after 15 min of incubation time after valinomycin addition. The presence of a membrane potential led to a small increase in tracks/movie in the sample without Neu5Ac, when compared to the same conditions without the membrane potential. To block the binding position of HiSiaP to HiSiaQM, a HiSiaQM-binding $Nb_{HiSiaQM}$ was applied before HiSiaP-AF647 was added. For these measurements, the amount of tracks per movie reduced greatly and was even below the value, measured for no HiSiaQM present. Under $Nb_{HiSiaQM}$ blocking, the presence of Neu5Ac did not have any influence. In the next step, HiSiaQM-wt was substituted with HiSiaQM-D304A, a protein mutant in which the amino acid aspartic acid (D) in position 304 was substituted with alanine (A). D304 is located close to a sodium binding site of HiSiaQM [12]. In our experiments, this mutant did not show any significant changes in binding events, when compared to the wild type. In the final measurement, another mutant was employed. HiSiaQM-D521A carries a mutation in the putative substrate-binding site [70] [21]. This mutant reduced the tracks per movie without Neu5Ac only slightly, when compared to the wildtype, but after addition of Neu5Ac almost no increase was visible.

Neu5Ac import assay

Finally, the success of the entire import process was assessed by testing, if Neu5Ac could be translocated from the surrounding solution into the vesicle lumen. The Neu5Ac release, which is finalizing the import, is highlighted in figure 43.

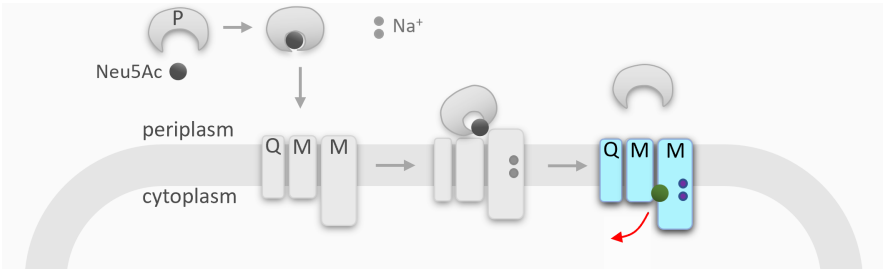


Figure 43: TRAP-transporter import overview. Schematic depiction of key steps of the proposed Neu5Ac import by SiaPQM with coloured highlight on the release of Neu5Ac into the cytoplasm. Based on [70].

Single-molecule FRET import assay into surface-immobilized LUVs

smFRET provides nanometer-scale distance information in real time [23]. Depositing single sensor proteins into the lumen of an LUV established a highly sensitive system to register even single Neu5Ac molecules. TIRF illumination was used to reduce background signal.

To test which sensor system was most suitable, both, the inter- and the intramolecular labeled sensors were tested by loading them into the lumen of DOPC/BioPE (100:1) LUVs. The aim was to achieve, on average, one sensor per LUV. Accordingly, the sensor concentration in the hydration solution was adjusted based on the previously determined average LUV diameter. However, because the LUV population exhibited a distribution of diameters, individual vesicles did not necessarily contain exactly one sensor. After formation, the LUVs were surface-immobilized via biotin-NAv binding. Finally, three washing steps exchanged the extravesicular solution and removed non-encapsulated sensor proteins. A negative control was acquired in absence of Neu5Ac and a positive control was measured by adding Neu5Ac into the hydration buffer before LUV formation. Corresponding exemplary data is shown in figure 44.

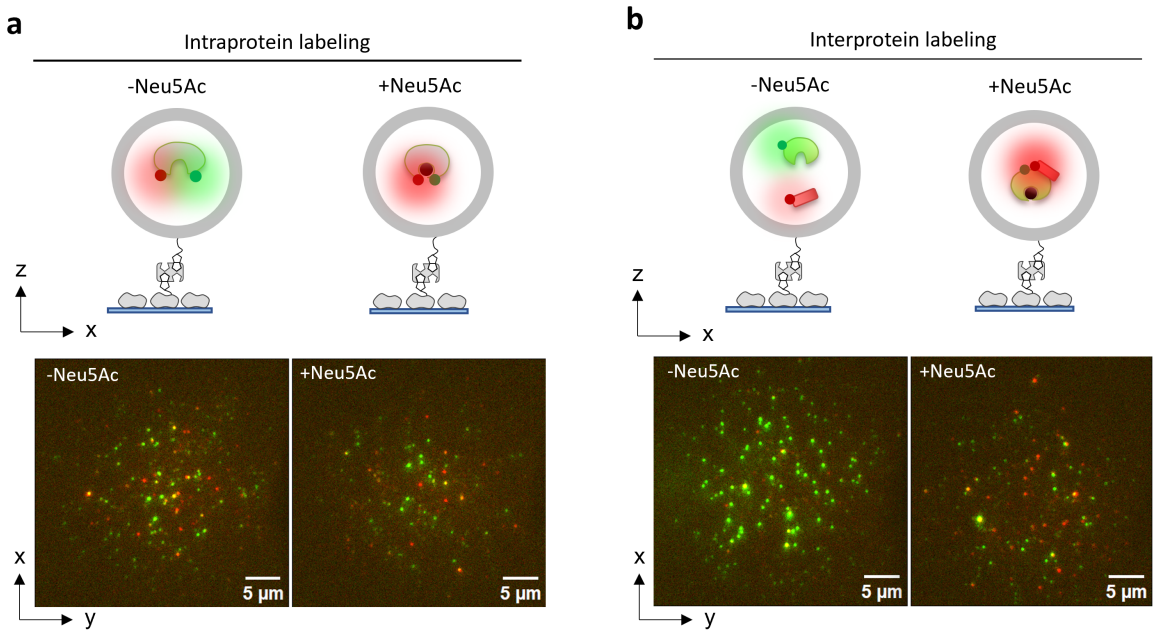


Figure 44: Inter- and intraprotein labeled FRET Neu5Ac sensors in surface-immobilized DOPC/BioPE (100:1) LUVs. Single signals indicate single LUVs. **a:** Overlay of the donor (green) and FRET channel (red) for VcSiaP-AF550-AF647 without Neu5Ac and with 2 µM Neu5Ac added pre-formation. **b:** Overlay of donor (green) and FRET channel (red) for $Nb_{P_{closed}}$-AF647 and HiSiaP-JF549 without Neu5Ac and with 2 µM Neu5Ac added pre-formation.

The software iSMS [73] was used for data evaluation. iSMS evaluates only signals that are visible in the FRET and the donor channel. For these signals, the raw FRET efficiency E'' was determined. Subsequently, histograms, showing the normalized frequency of E'', were generated and are depicted in figure 45.

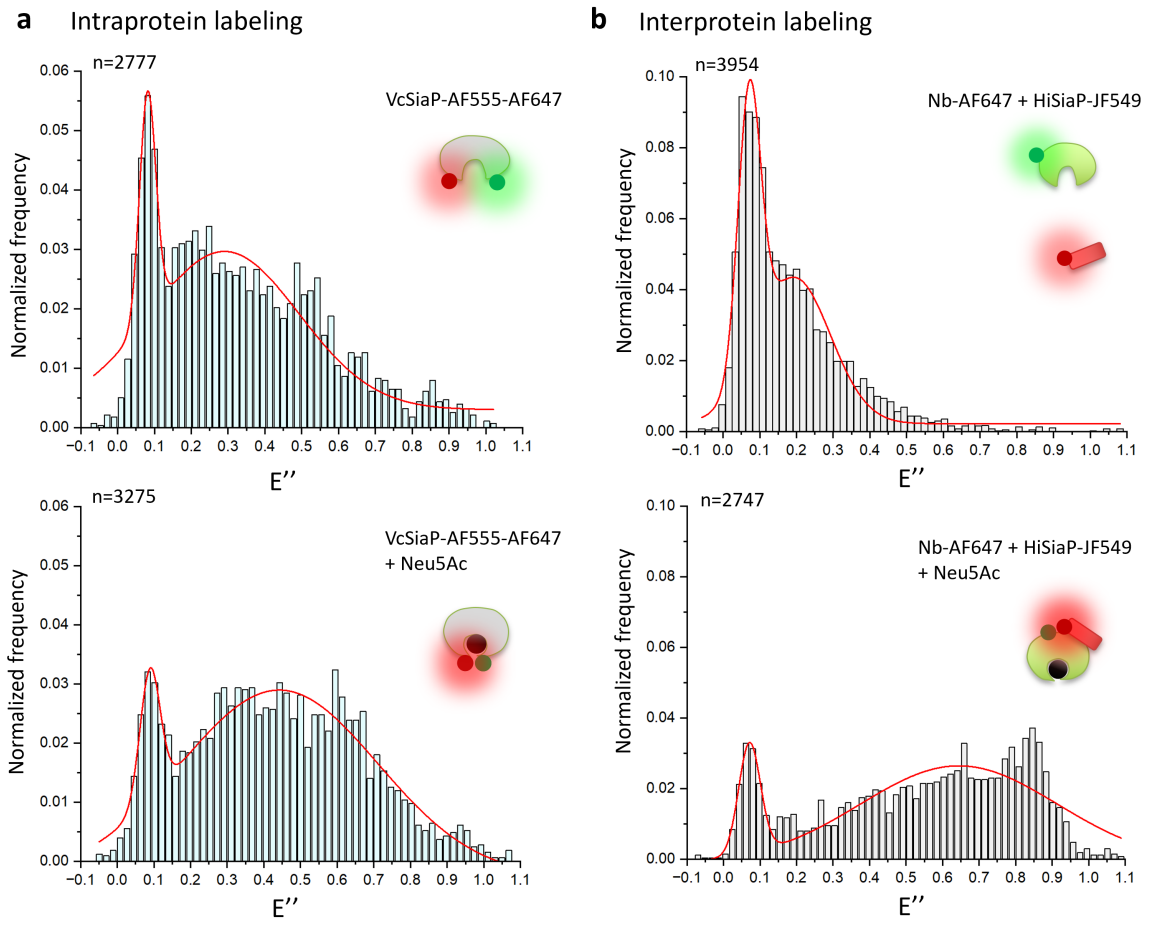


Figure 45: smFRET sensor systems recognize Neu5Ac. a: VcSiaP-AF555-AF647 in DOPC/BioPE (100:1) LUVs without Neu5Ac and with Neu5Ac added pre-formation. **b:** HiSiaP-JF549 and $Nb_{P_{closed}}$-AF647 in DOPC/BioPE (100:1) LUVs without Neu5Ac and with 2 µM Neu5Ac added pre-formation. The frequency was normalized to the total amount of signals. Two-component Gaussian functions (eq. 7) were fitted to all histograms (red). The fit parameters can be found in the Appendix (App. 9).

Both FRET sensor systems exhibited a distinct peak at low FRET efficiencies. This population likely originated from donor-only molecules, as donor emission bleed-through into the FRET channel can result in apparent FRET signals. All histograms were fitted with a two-component Gaussian function:

$$f(x) = y_0 + \sum_{i=1}^{2} \frac{w_i}{\sqrt{2\pi}\sigma_i} \exp\left(-\frac{(x-\mu_i)^2}{2\sigma_i^2}\right) \tag{7}$$

Both systems showed a visible histogram shift towards higher FRET efficiencies upon Neu5Ac presence, although the intermolecular labeling resulted in a more pronounced shift and was, therefore, chosen as the sensor system for upcoming smFRET experiments. While the big shift was advantageous, the intermolecular labeled sensor system exhibited the disadvantage that it consists of two different independently diffusing proteins. This may lead to different occupancies in the vesicle lumen that deviate from a donor:acceptor ratio of 1. The process of sensor protein encapsulation during LUV

formation is depicted schematically in figure 46. To overcome this challenge, ALEX was employed to distinguish between donor-only, acceptor-only, and different ratios of donor to acceptor signals.

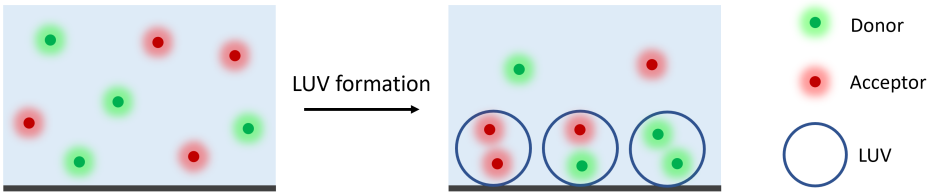


Figure 46: Poisson-distributed vesicle occupancy. Donor and acceptor diffuse independently during LUV formation, this results in a Poisson-distributed LUV occupancy. LUVs which contain only donor or only acceptor fail to report Neu5Ac import.

In order to calculate the corrected FRET efficiency E' and the corrected stoichiometry S', the correction factors donor leakage α and direct acceptor excitation δ were measured (App. 6).

Subsequently, donor- and acceptor-only samples were measured via ALEX smFRET. iSMS's function to analyze only spots in which donor as well as acceptor signal are present was disabled for these samples. Corrected FRET efficiency E' and corrected stoichiometry S' were determined for every signal and are shown as a heatmap in figure 47.

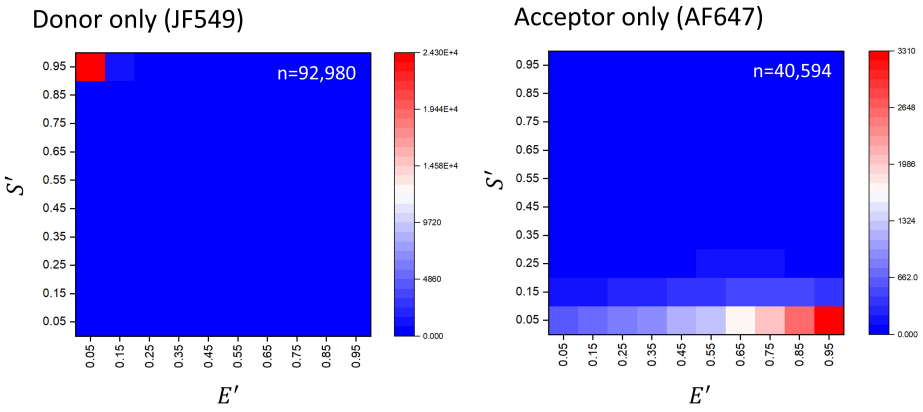


Figure 47: Donor- and acceptor-only ALEX smFRET in surface-immobilized DOPC/BioPE (100:1) LUVs. Results of ALEX smFRET measurements of donor-only and acceptor-only samples, shown as heatmaps with an interval width and height of 0.1. The corrected stoichiometry S' is shown on the y- and corrected FRET efficiency E' is shown on the x-axis.

As can be seen in figure 47, donor-only signals clustered around a corrected stoichiometry value of 1 and a corrected FRET efficiency value of 0. Acceptor-only samples

clustered at a corrected stoichiometry value of 0 and exhibited a rather broad corrected FRET efficiency distribution. In acceptor-only control samples, D_D and A_D are expected to be essentially absent. As a result, these channels contain mostly background and noise contributions, leading to a broad FRET efficiency distribution.

To reach a better understanding of ALEX measurements, an artificial data set was created and used for the prediction of the corrected FRET efficiency and stoichiometry changes for different LUV occupancies upon Neu5Ac saturation. The occupancies are indicated using the following notation: D represents a donor molecule and A represents an acceptor molecule. Therefore, the notation DDDAA would correspond to 3 donor molecules and 2 acceptor molecules per LUV. The data is shown in figure 48.

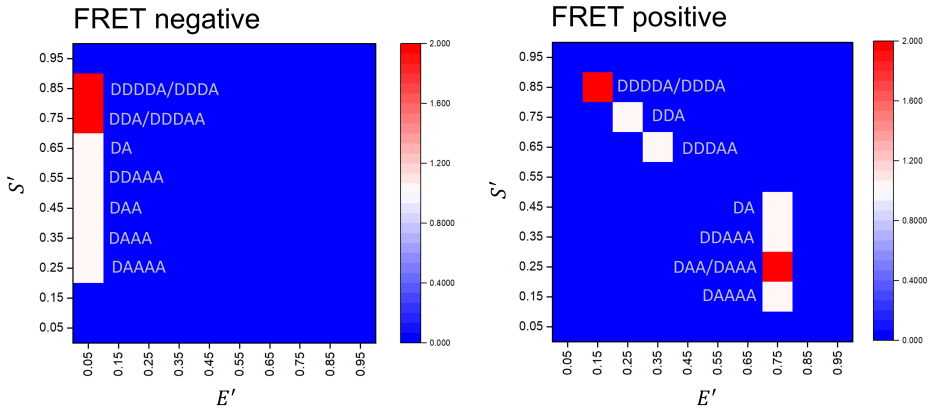


Figure 48: ALEX smFRET evaluation for artificial data set. Results of ALEX smFRET simulation for a FRET positive and a FRET negative artificial data set, shown as heatmaps with an interval width and height of 0.1. The corrected stoichiometry S' is shown on the y- and corrected FRET efficiency E' is shown on the x-axis. Used values: For FRET positive: $D_D = 50$, $A_D = 220$, $A_A = 300$, for FRET negative: $D_D = 500$, $A_D = 70$, $A_A = 300$. The correction factors that were determined for the optical system at hand were used. The occupancies that were included in the simulation are given in the heatmaps.

Notably, subpopulations emitted a less pronounced change in E' upon turning FRET-positive the higher their donor to acceptor ratio is. Also visible is that an increase in E' is always accompanied by a downward shift in S'. Furthermore, since the correction factor γ was not determined, an S' value of 0.5 does not need to coincide with a 1:1 ratio of donor:acceptor.

After performing the necessary steps to be able to interpret the final data, import measurements into surface-immobilized LUVs could finally be performed. To do so, LUVs were formed to contain on average one HiSiaP-JF549 and one $Nb_{P_{closed}}$-AF647 protein per vesicle. The concentration needed to establish this could be calculated based on the average LUV diameter measured via DLS previously. Subsequently, LUVs were surface-immobilized and washed. Neu5Ac import could then be registered by

an increase of FRET signal inside the LUVs. LUVs which do not contain at least one of both of the sensor proteins will fail to report Neu5Ac import. Next to the sensor proteins, the LUVs contained HiSiaQM and exhibited a sodium gradient in all experiments. A negative control was performed in absence of Neu5Ac (figure 50a). A positive control was acquired by adding Neu5Ac into the hydration solution before LUV formation (figure 50e). However, this control had the disadvantage that it introduced a bias in the occupancy of the LUVs. If HiSiaP-JF549 and $Nb_{P_{closed}}$-AF647 are already bound before LUV formation occurs, the occupancy is not Poisson-distributed anymore. This is schematically depicted in figure 49.

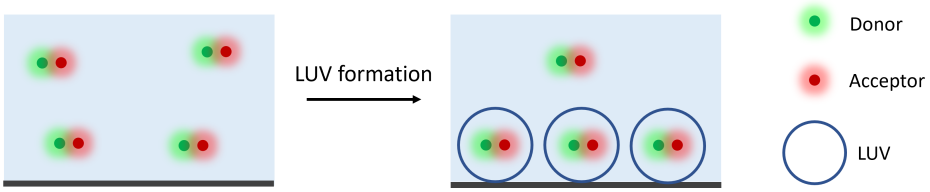


Figure 49: Vesicle occupancy with Neu5Ac added before LUV formation. Donor and acceptor diffuse together during LUV formation, if Neu5Ac was added before LUV formation, this results in a non Poisson-distributed occupancy.

Therefore, another control was performed. LUVs were formed before Neu5Ac was added. Subsequently, Neu5Ac import was mimicked by vesicle fusion. To this end, Neu5Ac containing positively charged LUVs were added to the sensor-protein containing negatively charged LUVs, as vesicle fusion leads to lumen combination of the two LUV species. The results are shown as heatmaps in figure 50d. Finally, the real import measurements were performed. First, Neu5Ac was added from outside, but no HiSiaP was provided (figure 50b). Next, both were added (figure 50c).

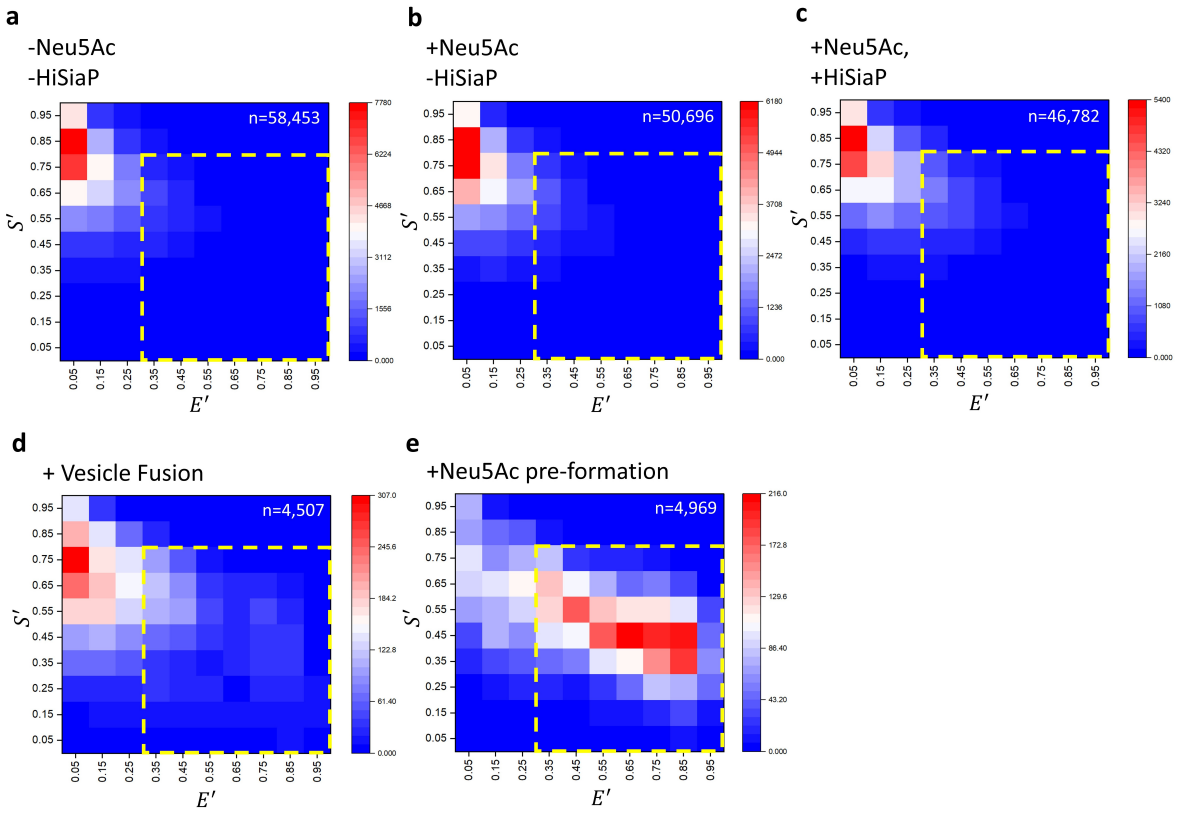


Figure 50: Neu5Ac import in LUVs, shown as heatmaps. smFRET ALEX data for surface-immobilized *E. coli* PL/POPC/BioPE (3:1:0.04) LUVs, containing HiSiaQM in a protein:lipid ratio of 1:1000 and exhibiting a sodium gradient towards the vesicle inside. The results are depicted as heatmaps with an interval width and height of 0.1. Stoichiometry is shown on the y- and FRET efficiency on the x-axis. **a:** Neither HiSiaP, nor Neu5Ac were added. **b:** 2 µM Neu5Ac were added from outside, no HiSiaP was present. **c:** 2 µM Neu5Ac were added from outside, 1 µM HiSiaP was added from outside. **d:** Positively charged LUVs containing Neu5Ac were mixed with the sensor-containing LUVs before immobilization. **e:** 2 µM Neu5Ac were added into the hydration buffer before LUV formation was started.

To quantify the heat map shift towards higher FRET efficiencies, the marked area in figure 50 (Stoichiometry 0 to 0.8 and FRET efficiency 0.3 to 1) was chosen as a region of interest (ROI) and the points contained within the ROI were counted. The percentage of points contained by the ROI versus all points was calculated and plotted as a scatter diagram in figure 51.

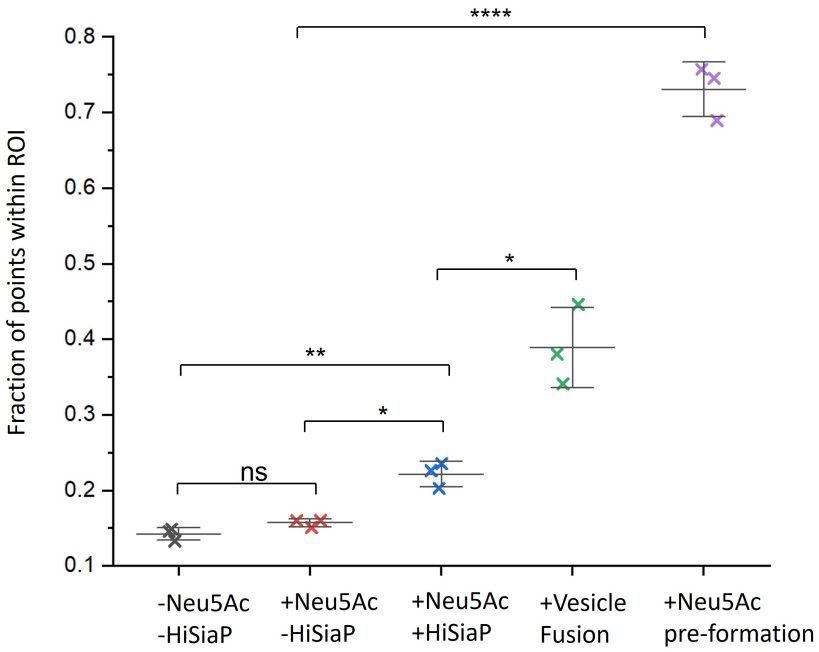


Figure 51: Neu5Ac import in LUVs. Percentage of points contained in ROI of ALEX data for different conditions. Mean values of three experiments are shown with their standard deviation as error bar.

The data indicates that Neu5Ac addition without HiSiaP led to no significant increase in percentage of points within the ROI. If HiSiaP was added additionally a significant increase took place and the percentage rose from 14.2 ± 0.7% to 22 ± 1%. If Neu5Ac containing, positively charged LUVs were applied, the percentage increased to 39 ± 4%. Finally, if Neu5Ac was already added to the solution in which LUVs were formed, the percentage climbed up to 73 ± 3%.

Ensemble import assay in GUVs

As the single-molecule FRET assay only provided a binary detection approach, the next step was to develop an assay that enables a real time ensemble import observation. For that purpose, GUVs were employed as a model system and loaded with VcSiaP-AF555-AF647 as a Neu5Ac FRET sensor protein. The advantage of using VcSiaP was that it was found to not be able to bind to HiSiaQM, effectively preventing possible export of the substrate [61]. Additionally, the intraprotein labeling ensured an always identical ratio of donor and acceptor, unaffected by the different abilities of proteins to permeate through the gel substrate, used for the GUV swelling. The GUVs were composed of *E. coli* PL/POPC/TopFluorPC (3:1:0.01). After formation, GUVs were diluted in buffer solution, which led to the dilution of the non-encapsulated VcSiaP. Imaging of the TopFluorPC, which localized in the GUV membrane, enabled segmentation of the GUV lumen and surrounding solution. The presence of VcSiaP in the in- as well as outside-buffer resulted in the opportunity to independently monitor the Neu5Ac concentration

on the in- and outside of GUVs. Figure 52 shows an exemplary measurement, split into the different acquired channels.

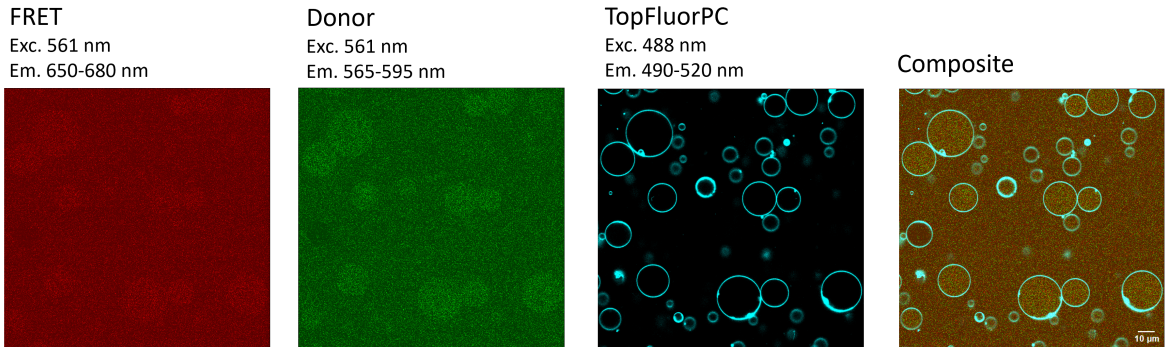


Figure 52: Channels of ensemble FRET measurement. Images of the acquired channels of an exemplary measurement of *E. coli* PL/POPC/TopFluorPC (3:1:0.01) GUVs with 60 nM VcSiaP-AF555-AF647.

To evaluate the acquired data, ROIs were manually placed inside the imaged GUVs (GUV_{IN}), while the non-encapsulated solution was automatically segmented and measured by a self-written Fiji macro (GUV_{OUT}). The macro's workflow is described in detail in section 6. An example of the image segmentation is shown in figure 53.

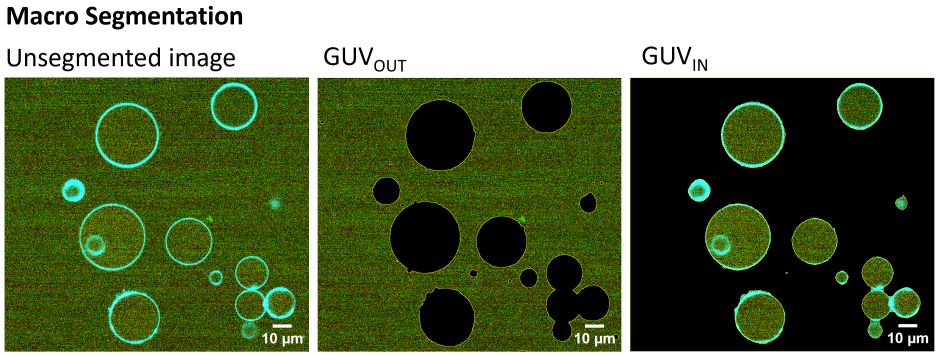


Figure 53: Macro segmentation. Exemplary data after image segmentation in GUV_{IN} and GUV_{OUT}. The yellow line surrounds the selected area. For representation purposes, the not in the selection included area has been deleted from the shown images.

In figure 54, the raw FRET efficiencies calculated from the GUV_{IN} ROIs E''_{IN} are depicted as green scatter plots, while the raw FRET efficiencies of GUV_{OUT} ROIs E''_{OUT} are shown in red scatter plots. The first condition measured was a negative control in which no Neu5Ac was added to the GUV solution. In this case, E''_{IN} and E''_{OUT} did not significantly differ from each other. For the next experiment, Neu5Ac was applied from the outside, but no HiSiaP was added. In this case, E''_{IN} was slightly elevated in comparison to the experiments without Neu5Ac. E''_{OUT}, on the other hand, showed an increase of about 8%, indicating that the VcSiaP in the outside-solution was saturated with Neu5Ac. Finally, Neu5Ac and HiSiaP were applied together. For this experiment, E''_{IN} was elevated in comparison to the experiments in which no HiSiaP

was added, while the data showed no significant difference between the E'' of the in- and outside solution. These results indicate successful Neu5Ac import in presence of HiSiaP. Finally, a positive control was performed by adding Neu5Ac already to the GUV swelling solution. In this case, the raw FRET efficiencies of in- and outside solution both show VcSiaP saturation with Neu5Ac. No significant difference between vesicle in- and outside was detected.

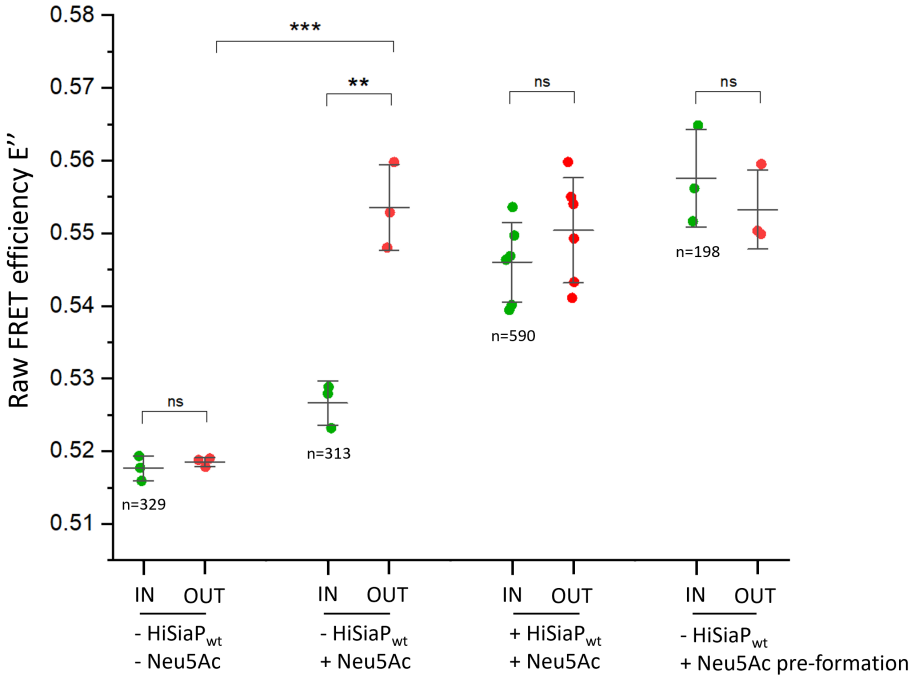
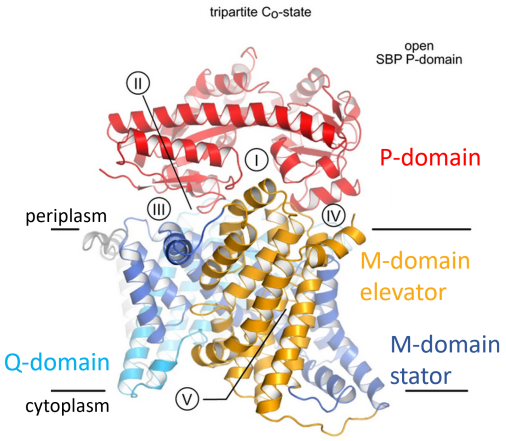


Figure 54: Neu5Ac detection via ensemble FRET in GUVs. Plot of the raw FRET efficiency E'' in- and outside of *E. coli* PL/POPC (3:1) GUVs of mean values of at least three measurement. HiSiaP was added in a concentration of 5 µM and Neu5Ac was added in a concentration of 15 µM, if added. The number of single GUVs contributing to the mean values are shown in the graph. The significance was determined via a Student t-test and is indicated on top of the scatter plots (*p<0.05, **p<0.01, ***p<0.001).

As visible in figure 54, inhomogeneous distribution of Neu5Ac between vesicle in- and outside leads to a E''_{in}/E''_{out} ratio that deviates from 1. The ratio will be called import success in the following. The more the value approaches 1, the more import has occurred.

Different protein mutants were used to test the HiSiaPQM's import mechanism and to determine how the respective mutations altered its activity. The protein mutants were expressed and purified by Philipp Hendricks from the workgroup of Dr. Gregor Hagelüken. An overview of the mutants with their structural context is shown in figure 55.

a



b

Mutation	Region of the mutation [70]
QM-F111A	periplasmic loop Q3-Q4 (II)
QM-F111E	periplasmic loop Q3-Q4 (II)
QM-loop del. (Δ111-118)	periplasmic loop Q3-Q4 (II)
QM-D304A	Na^+/Neu5Ac binding site (V)
QM-R30E	P-QM interface, C-lobe (IV)
QM-E429R	P-QM interface, C-lobe (IV)
QM-W227R	P-QM interface, N-lobe (III)
P-E172R	P-QM interface, C-lobe (IV)
P-F74A	periplasmic loop Q3-Q4 (II)
P-S60R	P-QM interface, N-lobe (III)

Figure 55: Structural context of protein mutants. a: AlphaFold model of the tripartite complex in the outward-facing strate (OFS) with P_{open}. Image modified from [70]. **b:** Protein mutations used in this study with the region in which the mutation is located. Mutations are denoted using the single-letter amino acid code with the original residue, residue number, and substituted residue indicated. For the QM-loop del. mutant, residues 111-118 have been deleted.

The individual import successes for different environmental conditions or mutants were determined after 20 minutes after Neu5Ac addition. Mean import success values for independent measurements are shown as column diagram in figure 56.

In the first measurement, HiSiaQM-wt and HiSiaP-wt were tested. Additionally, a sodium gradient directed towards the vesicle lumen was established. Here, the import success did not significantly differ from 1, indicating that Neu5Ac import was successful. Keeping all other parameters unchanged, but omitting HiSiaP, led to a significant decrease in import success. A similar result could be observed, when instead of HiSiaP, the sodium gradient was removed in favor of equal sodium levels on both sides of the membrane. In the following, different protein mutants were tested. The P-mutants HiSiaP-F74A, HiSiaP-S60R and HiSiaP-E172R in combination with HiSiaQM-wt and a sodium gradient resulted in reduced import successes, when compared to HiSiaP-wt. HiSiaQM-W227R and HiSiaQM-F111A were able to achieve similar import successes as HiSiaQM-wt, while HiSiaQM-E429R, HiSiaQM-F111E, HiSiaQM-D304A and HiSiaQM-loop del. showed attenuated import success when compared to HiSiaQM-wt.

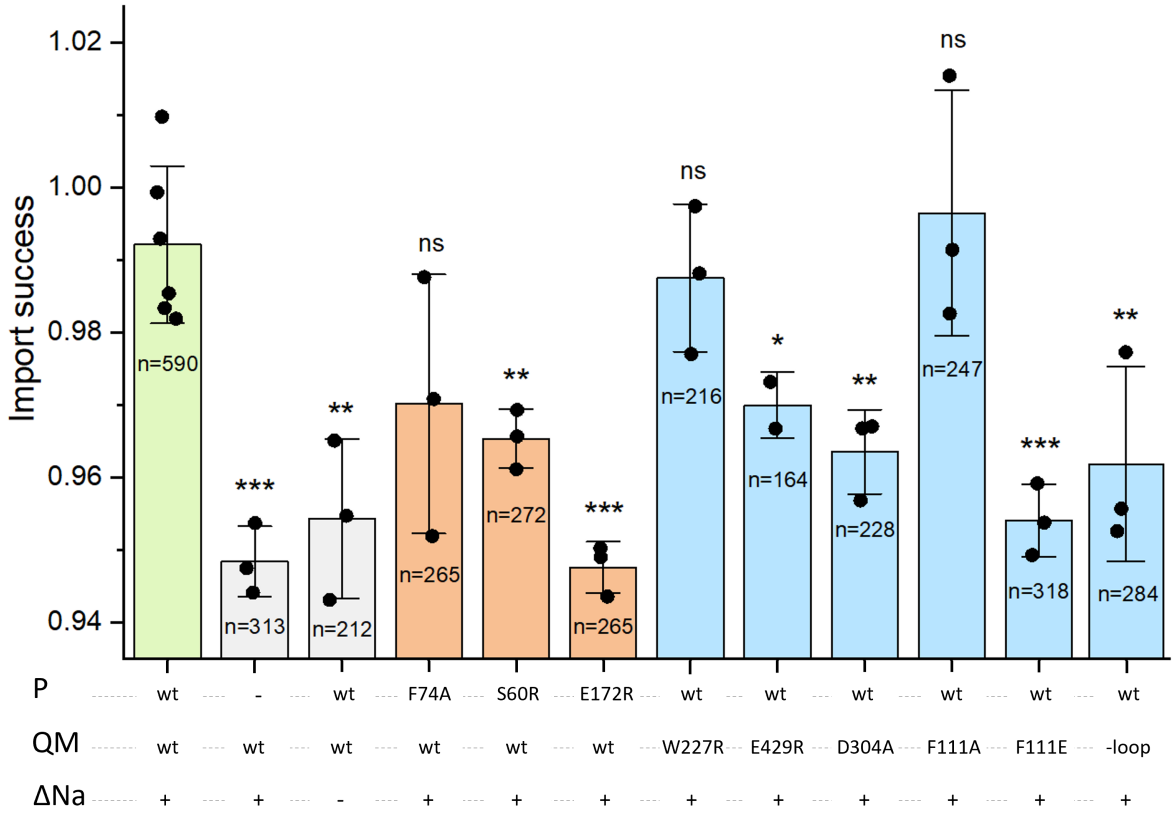


Figure 56: Import success. Mean import success of different experiments after 20 minutes of Neu5Ac addition as a column diagram with the respective standard deviation for different conditions. The mean of each experiment is represented as a point. Green columns represent experiments in which import conditions, according to [61], are met and HiSiaP-wt and HiSiaQM-wt were used. Grey columns represent experiments in which HiSiaP-wt and HiSiaQM-wt were used, but import conditions are not met. Orange columns represent experiments with P-domain mutations but HiSiaQM-wt, while blue columns represent experiments with QM-domain mutations but HiSiaP-wt. The amount of single GUV ROIs contributing to each column is written onto the column. The significance was tested via an unpaired Student t-test against the wildtype measurement under import conditions and is indicated on top of the column (*p<0.05, **p<0.01, ***p<0.001).

Time-resolved ensemble import assay into GUVs

After demonstrating that import could be observed in the model system at hand, the progress of the import was monitored over time. To quantify the progress, the FRET efficiency on the GUV inside was measured directly after Neu5Ac addition and then after the time t had passed. To show the time development, or lack thereof, the time-dependent raw FRET efficiency ratio was calculated as $E''_{in,t}/E''_{in,0s}$. This ratio will be called import progress in the following. Effective import is then shown by an import progress that exceeds 1 significantly.

The import progress for HiSiaPQM-wt was depicted over time in presence of either only a sodium gradient or a sodium gradient in tandem with a membrane potential and for

HiSiaQM-D304A in combination with HiSiaP-wt and a sodium gradient (figure 57).

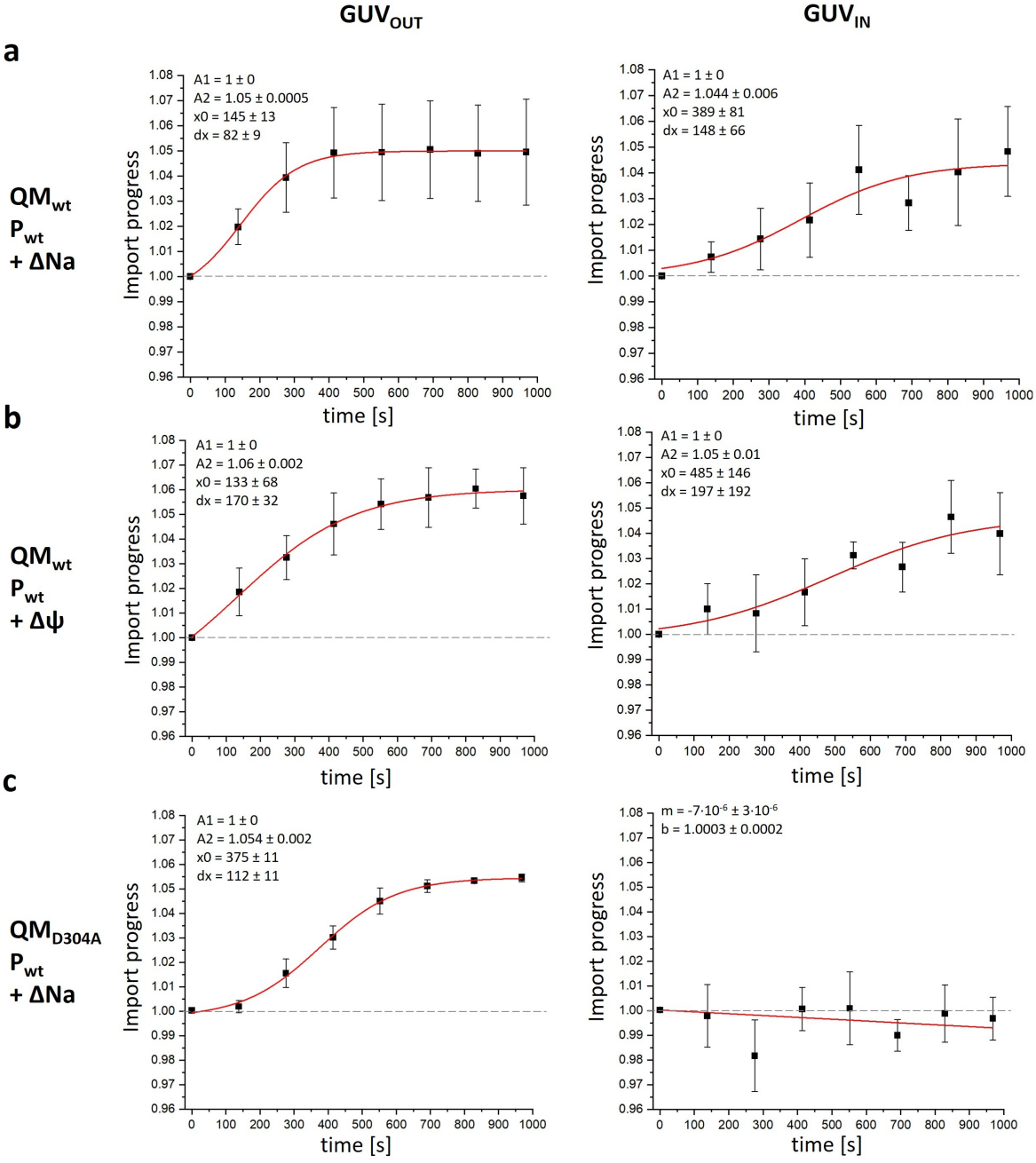


Figure 57: Time-resolved Neu5Ac import. Mean import progress of GUV$_{OUT}$ and GUV$_{IN}$ (left and right column). **a:** For HiSiaQM-wt, HiSiaP-wt in presence of a sodium gradient. **b:** For HiSiaQM-wt, HiSiaP-wt in presence of a membrane potential and a sodium gradient. **c:** With HiSiaQM-D304A and HiSiaP-wt in presence of a sodium gradient. The data was fitted with a Boltzmann function (a, b) or a linear function (c), represented in red. The fitting parameters are given in the graph. Each mean import progress curve was calculated from three independent experiments. Error bars indicate the standard deviation.

A Boltzmann function was fitted to the data that showed an increase in import progress, yielding parameters for the minimum (A_1) and maximum (A_2) responses, the half-maximal point x_0, and the slope factor dx.

$$y = \frac{A_1 - A_2}{1 + e^{(x-x_0)/dx}} + A_2 \tag{8}$$

The minimum response A_1 was set to 1 for the fit. Interestingly, complete saturation was not reached for GUV_{IN}, as A_2 of the inside solutions stayed below the values reached for the outside solutions. x_0, on the other hand, was elevated in the inside solutions, indicating that more time passes after measurement start until half of the maximal response has been triggered. This delay would correspond to the time taken up by the import. However, no significant differences were visible between GUV_{IN} in presence or absence of the membrane potential. As the GUV_{IN} measurement with HiSiaQM-D304A did not increase in import progress over time, a linear fit was performed on this data set.

To compare the effects of various experimental conditions on the HiSiaPQM functionality, the import progress was determined for all conditions after 829 s. The import progress, depicted as column diagram is shown in 58.

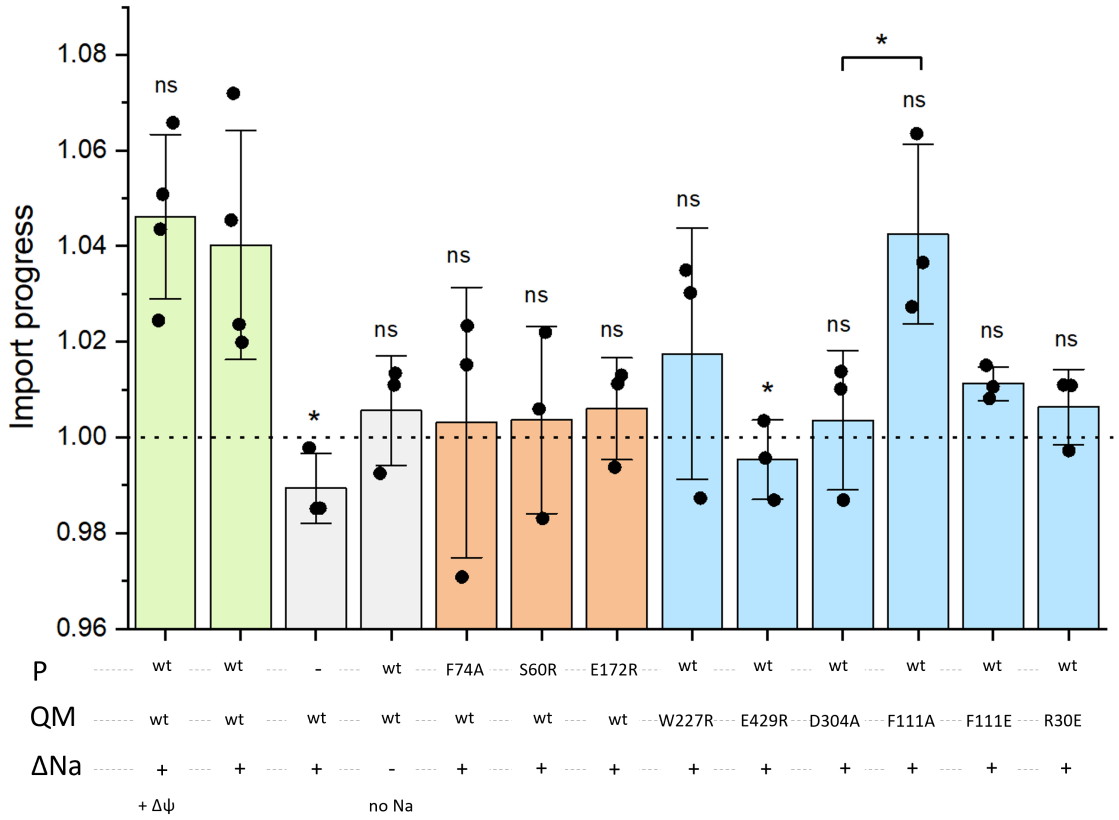


Figure 58: Import progress. Mean import progress of minimum three independent experiments 829 s after Neu5Ac addition as a column diagram with the respective standard deviation. The mean of each experiment is shown as a point. Green columns represent experiments in which import conditions, according to [61], are met and HiSiaP-wt and HiSiaQM-wt were used. Grey columns represent experiments in which HiSiaP-wt and HiSiaQM-wt were used, but import conditions are not met. Orange columns represent experiments with P-domain mutations but HiSiaQM-wt, while blue columns represent experiments with QM-domain mutations but HiSiaP-wt. The significance was tested via an unpaired Student t-test against the wildtype measurement with a sodium gradient, but without a membrane potential and is indicated on top of the column (*p<0.05, **p<0.01, ***p<0.001).

Overall, the measured import progress aligned well with the previously measured import success. Import progress was measured with a membrane potential established next to a sodium gradient which led to slightly larger import progress after 829 s, when compared to experiments in which only the sodium gradient was established. Absence of HiSiaP resulted in an import progress even slightly below 1, indicating that import was strongly attenuated. Complete sodium absence similarly resulted in a decreased import progress in presence of HiSiaQM-wt and HiSiaP-wt. The mutants HiSiaP-F74A, HiSiaP-S60R, HiSiaP-E172R, HiSiaQM-E429R, HiSiaQM-D304A, HiSiaQM-R30E remained under an import progress value of 1.01, indicating only minimal changes in the raw FRET efficiencies of the GUV lumens after 829 s. HiSiaQM-W227R and HiSiaQM-F111E exceeded this value slightly. QM-F111A showed, in good agreement to the import success measurements, notably elevated import progress.

3 Discussion

The goal of this thesis was to investigate two membrane transporter systems: The lipid II flippase and TRAP transporters. Both represent promising drug targets, due to their absence in eukaryotic organisms [76] [79]. Because *in vivo* studies are inherently complex and make it difficult to isolate individual factors, membrane model systems were employed. Therefore, systems that mimic cellular membranes and remain experimentally accessible were required. For this purpose, giant unilamellar vesicles (GUVs) and large unilamellar vesicles (LUVs) were utilized. Each of these models offers distinct advantages and limitations, but together they provide a complementary framework. Both model systems had to meet specific requirements to enable functional reconstitution of membrane proteins and their observation by fluorescence microscopy. GUVs are not commonly used in protein activity studies, as typical formation pathways can lead to membrane protein denaturation. Consequently, established preparation methods had to be adapted and the produced model systems had to be characterized.

3.1 Model system optimization and characterization

3.1.1 Giant unilamellar vesicles

In this work, I developed a new GUV formation method which is based on the work of Dezi *et al.*, 2013 [14] and Parigoris *et al.*, 2020 [67]. Detergent-mediated swelling of proteo-GUVs is an accessible method that is able to produce high proteo-GUV yield in presence of physiological salt concentrations, which was difficult to achieve with previous methods. Contradicting are the membrane proteins' requirement for a detergent concentration above the CMC and the GUVs' destabilization by high detergent concentrations [90]. Here, GUV formation was directly performed in detergent presence. This presumably led to a symmetric detergent molecule distribution among both lipid leaflets, which improved the membranes' detergent tolerance. Detergent-mediated electroformation was already presented by Dezi *et al.*, 2013 [14]. Here, I employed detergent-mediated swelling. This technique allows for a GUV formation in physiological salt concentrations which was not the case for detergent-mediated electroformation. Polyacrylamide gels were used as swelling substrate, as proposed by Parigoris *et al.*, 2020 [67], to prevent gel incorporation into the produced GUVs. Using detergent-mediated swelling, four different membrane proteins (MurJ, FtsW, RodA and HiSiaQM) were successfully reconstituted into the GUV membrane. This indicates that the method is applicable for a variety of membrane proteins.

Furthermore, the method allowed for cargo encapsulation. The cargo concentration

in the GUV lumen was found to be about half of the swelling solution's concentration for cargo exhibiting a hydrodynamic radius of about 2.5 nm, which would correspond to a globular protein of about 20-50 kDa [16]. Moreover, GUVs, produced via detergent-mediated swelling, exhibited predominantly intact membranes with a unilamellar percentage of 76 ± 2%. In 2013, McPhee *et al.* examined GUVs formed via electroformation in salt-free water and found a unilamellar fraction of about 81% [52]. In comparison, detergent-mediated swelling, although performed in salt-solutions, produced a similar unilamellarity.

A very important property of the bacterial cell membrane is the membrane potential, as it serves as an energy source for the transport systems, investigated in this work. Replicating this complex property has proven to be challenging in artificial membranes. Bally *et al.*, 1985 exploited the properties of valinomycin and combined it with LUVs exhibiting an ion gradient to establish a membrane potential. The potential was detected spectroscopically with the Nernstian dye safranin [5].
In this work, I measured the membrane potential via fluorescence microscopy. The formation of GUVs in physiological salt solutions enabled the establishment of a membrane potential in GUVs. The measurements in this work show that membrane potentials of up to -70 mV could be established in presence of both, valinomycin and a potassium gradient, although the GUVs exhibited a broad distribution of membrane potentials, which indicated that a fraction of GUVs failed to build up a membrane potential. This could have been caused by multilamellarity or membrane defects that allow for unspecific ion leakage. The theoretically expected membrane potential of -79.4 mV, defined by the potassium concentration gradient, was underscored in practice. However, it must be noted that linear dependence of fluorescence intensity and fluorophore concentration can only be assumed for low concentrations [39]. Therefore, it is possible that the established membrane potential was underestimated in this work. Gibbs free energy estimations for the here used model system suggest that it can nevertheless provide similar free energy values for ion transport like bacterial cells [6].

3.1.2 Large unilamellar vesicles

Existing LUV formation protocols are compatible with high-salt solutions and LUVs have often been used in membrane protein function studies. Therefore, they are a valuable and reliable system. LUV formation was performed via established methods. Here, LUVs were immobilized to enable single vesicle imaging. This was accomplished via agarose-embedding [46] or BioBSA-NAv binding [98]. While the latter method is useful to fixate LUVs on the coverslip surface, the contact with the rigid glass surface can flatten or distort LUVs. Furthermore, reconstituted membrane proteins might stick to the glass rather than staying exclusively in the bilayer. Therefore, it must be

noted that a glass-supported vesicle may not fully represent a free-standing membrane system. Successful membrane protein reconstitution could be achieved for fluorescently labeled HiSiaQM, MurJ, FtsW and RodA.

In summary, I established and characterized two model systems, which allow the in-depth investigation of the two membrane transporters at hand. The biomimetic vesicle system created here is schematically depicted in figure 59.

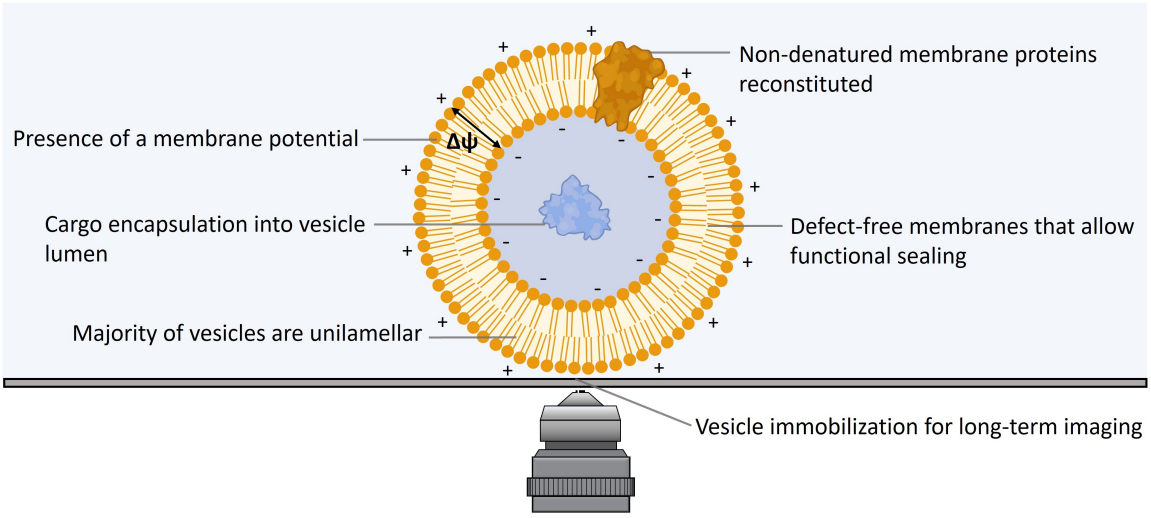


Figure 59: Artificial vesicle with the established properties. Schematic model membrane system, as created in this work together with the necessary requirements that enable functional membrane protein observation.

3.2 The lipid II flippase

The identity of the lipid II flippase has been a topic of ongoing discussion. While most evidence speaks in favor of MurJ being the flippase, lipid II flipping has never been demonstrated in membrane model systems. In 2018, Rubino *et al.* found that lipid II flipping is attenuated by absence of a membrane potential, suggesting that the membrane potential is the driving force of the lipid II flip [77]. However, this property was not yet added into model system measurements. To our knowledge, this study tests for the first time all three leading lipid II flippase candidates for their flipping activity in membrane model systems which provide a membrane potential. The key measurements were performed in LUVs. A drawback of this model system is that the fluorescence intensity of the lumen cannot be directly measured via fluorescence microscopy which makes it difficult to determine which exact membrane potential was reached. Bacteria usually exhibit membrane potentials of about -100 mV to -200 mV [6], the theoretical value for this study was defined by the established potassium gradient and amounts to -208 mV.

3.2.1 MurJ shows lipid II flipping activity

The lipid II orientation was measured via dithionite quenching of lipid II-NBD. This technique has also been used by Mohammadi *et al.*, 2011 [56], who did not apply a membrane potential and performed the assay spectroscopically in free floating LUVs. Their results revealed a decreased protected fraction of lipid II-NBD, if FtsW was added into LUVs, indicating lipid II flipping activity of FtsW [56]. This effect, however, was later on shown to be unspecific for lipid II [57]. Mohammadi *et al.*, 2014 concluded that FtsW might offer a pore-like structure through which lipid II and other phospholipids can pass [57]. In this thesis, dithionite quenching was measured via confocal laser scanning microscopy in surface-immobilized LUVs. Interestingly, the fluorescence dropped to less than 50% upon dithionite addition. This could be partly attributed to the size difference of outer and inner LUV leaflet. However, it also seems probable that, as the LUVs are surface immobilized, some lipid residues of collapsed LUVs remain on the surface. These lipids have no protected fraction and will, therefore, be quenched completely. Dithionite quenching of lipid II-NBD was performed for all three proteins in presence and absence of a membrane potential. Already in absence of a membrane potential, MurJ presence led to a smaller protected fraction than the other proteins. FtsW and RodA did not show significant differences when compared to a sample without reconstituted protein. In presence of a membrane potential, MurJ's effect increased and the protected fraction decreased significantly, while the other proteins did not show significant changes upon membrane potential establishment. This suggests that MurJ is able to translocate lipid II-NBD, in contrast to FtsW and RodA. Interestingly, even with MurJ and a membrane potential, a protected fraction of lipid II-NBD remains. Whether this is due to the membrane potential being consumed before all lipid II-NBD could be flipped, or due to other reasons, cannot be answered with our experiments.

Our results support findings of Kumar et al., 2019. They proposed that MurJ requires the membrane potential to reset from its outward-open to the inward-open conformation in the lipid II flipping cycle [38]. Kumar et al., 2019 suggested that this conformation reset is driven by a cation antiport [38]. This seems more likely than an anion symport, due to MurJ's structural similarity to the MATE transporters [38], which are known to utilize cation exchange to drive transport. The MATE transporters, that have been investigated, function by H^+ or Na^+ exchange [65]. If the membrane potential would indeed drive the conformational reset, this could result in the ability of MurJ to perform one single flipping cycle in absence of a membrane potential. Subsequently, it would be trapped in its outward-open conformation. This could explain the activity MurJ already exhibited in our experiments in absence of a membrane potential. Two known MurJ inhibitors were applied to samples containing MurJ and led to a visibly

increased protected fraction. ComD was found to inhibit cell wall biosynthesis by Mott *et al.*, 2008 [59]. They also identified a point mutation in MurJ that grants resistance against ComD. The position of this residue far from the putative substrate binding site suggests that ComD binds MurJ and allosterically traps it in its current conformation [59] [37]. The second used inhibitor was the indole compound CDFI, found by Huber *et al.*, 2009 [30]. Three point mutations were identified in MurJ that resulted in resistance against CDFI. Their positions indicate that CDFI and ComD exhibit different mechanisms of action, although both presumably inhibit MurJ allosterically [37]. The inhibitory effect of both compounds could be confirmed by our results. Taken together, our results strongly support MurJ as a lipid II flippase under the conditions tested, whereas neither RodA nor FtsW showed significant flipping activity in our assay.

In 2025, Englehart *et al.* found that in *B. subtilis* MurJ cannot be the sole lipid II flippase [15]. They suggested that there are two distinct peptidoglycan synthesis pathways. One, in which MurJ acts as the flippase, while transglycosylation and transpeptidation are executed by aPBPs and a second one, in which the lipid II flipping as well as peptidoglycan synthesis are mediated by a complex of a bPBP and a SEDS protein (FtsW or RodA) [15]. It has already been shown that SEDS and bPBPs form a 1:1 complex and share extensive interaction interfaces. These complexes were found to synthesize peptidoglycan [87]. Therefore, it could be possible that FtsW and RodA in our experiments could not flip lipid II as their cognate bPBP was not present.

Proposed MurJ mechanism

Our results support the following mechanism for MurJ's lipid II flipping activity (figure 60).

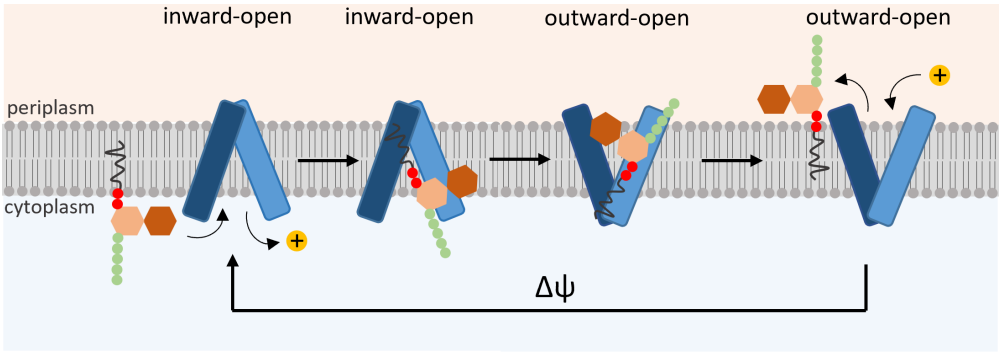


Figure 60: Proposed MurJ cycle. MurJ is shown to flip lipid II from cyto- to periplasm by an alternating-access mechanism. Then it resets from outward-open to inward-open state by antiporting a cation. Based on [38].

Presumably, MurJ starts out in its inward-open state and binds lipid II in this state. It then performs an alternating access mechanism to mediate the transfer of lipid II's

hydrophilic headgroup over the membrane. On the periplasmic side, lipid II then detaches again from MurJ in its outward-open state. Our work indicates that MurJ can perform one flip even without a membrane potential, although lipid II flipping increases in presence of a membrane potential. This suggests that MurJ needs the membrane potential to antiport an cation along its ion gradient to reset back from the outward-open into the inward-open state. The cation antiport is more likely than an anion symport due MurJ's structural similarity to the MATE transporters, although this cannot be concluded from our data [38]. Here, a very limited model system was used, containing only the following cations: K^+, Na^+ and H^+. If MurJ functions as a cation antiporter, one of these ions must be the cation that gets imported into the vesicles. K^+ was used to create a steep gradient towards the vesicle outside, which makes its import energetically unfavorable. Therefore, presumably Na^+ or H^+ act as the antiported cations. This aligns with the cations used by MATE transporters and is sensible regarding their structural similarity [65].

3.3 TRAP transporters

The second aim of this thesis was to observe Neu5Ac import, orchestrated by HiSiaPQM, via fluorescence microscopy in real time. Required for this assay was the development of an SBP-based Neu5Ac sensor system. With this, we wanted to develop a real-time Neu5Ac import assay to gain knowledge about the TRAP transporter mechanism by testing mutants on their import ability and environmental factors influencing it.

3.3.1 Two FRET sensors can detect Neu5Ac

The import process is initiated upon binding of Neu5Ac by the P-domain (SBP). The SBP converts upon substrate binding into a closed position by bringing its two globular domains closer together. This property was utilized for FRET measurements by an intraprotein labeling of VcSiaP [69], and an interprotein labeling of HiSiaP and $Nb_{P_{closed}}$. Both sensors showed a significant increase in FRET efficiency, if Neu5Ac was present, although the FRET efficiency increase was lower for intraprotein labeling. This is in agreement with expectations, as the donor and acceptor are already in a distance of less than 10 nm, in P_{open}, and therefore go from a "low-FRET" state to a "high-FRET" state, while $Nb_{P_{closed}}$ and HiSiaP start in a "non-FRET" state for the interprotein labeling approach. The binding affinity with which VcSiaP-AF555-AF647 binds Neu5Ac could be determined to be 450 $\pm$ 180 nM. This is in agreement with the value measured by Peter *et al.*, 2021 [69], who found an affinity of 300 $\pm$ 100 nM. Hence, two sensor systems could detect Neu5Ac presence with nanomolar affinity.

3.3.2 HiSiaP-QM complex formation

The next part of the import process is initiated upon delivery of the substrate to the membrane-integral QM-domain, resulting in an interaction between the P- and the QM-domain [70]. HiSiaP-QM complex formation was monitored in real-time on a single-molecule level by observing the interaction of HiSiaP-AF647 with HiSiaQM-containing surface-immobilized LUVs. These measurements can be compared to measurements performed by Peter *et al.*, 2022 [70], who also probed the HiSiaP-QM complex formation via single-molecule microscopy of HiSiaP-AF647. However, their measurements were performed on solid supported lipid bilayers, which do not allow for functional sealing, therefore, no ion gradient could be generated. In this study, surface immobilized LUVs were used as a model system, which allowed the deposition of different solutions in- and outside the LUVs.

Measurements in presence of a sodium gradient did not differ significantly from measurements performed with sodium chloride solution deposited on both sides of the LUVs. For both conditions the influence of Neu5Ac addition was tested, and in both cases, Neu5Ac presence led to an increase in binding interactions. With an excess of Neu5Ac, HiSiaP would mostly be present as $HiSiaP_{closed}$, while HiSiaQM mostly assumes its Inward Facing State (IFS). This suggests that $HiSiaP_{closed}$ exhibits a higher affinity towards HiSiaQM-IFS than P_{open}. This result is in good agreement with the study of Peter *et al.*, 2024, who found a conformational coupling between $HiSiaP_{closed}$ and HiSiaQM-IFS [71]. Mulligan *et al.*, 2009 identified the sodium gradient as driving force for the Neu5Ac import [61]. Interestingly, however, the absence of a sodium gradient did not affect HiSiaP-QM complex formation, indicating that this initial step does not rely on the gradient.

If potassium chloride was deposited in- and outside the LUVs, significantly reduced HiSiaP binding was visible. Without sodium, binding was also not elevated in presence of Neu5Ac. This indicates that HiSiaQM might require bound sodium ions, before it can interact with HiSiaP. Alternatively, sodium could also be structurally essential for either HiSiaP or HiSiaQM. Its absence would then lead to destabilization of their conformational structures and, therefore, reduced binding.

Subsequently, two HiSiaQM mutants were tested. The first was HiSiaQM-D304A. Currie *et al.*, 2024 found that D304 is not directly involved in Na^+-binding, but coordinates the residues of one of the Na^+-binding sites of HiSiaQM [12]. Peter *et al.*, 2022 performed a growth assay with HiSiaQM-D304A. The growth assay used SEVY3, a modified *E. coli* strain in which the Neu5Ac transporter NanT was replaced by HiSiaPQM.

With Neu5Ac as the only carbon source, bacterial survival was then linked to successful Neu5Ac import, executed by HiSiaPQM [70]. Substitution of the charged aspartic acid (D) with the unpolar alanine (A) rendered the protein entirely non-functional and, therefore, inhibited cell growth [70]. These results suggest an essential role of D304 during Neu5Ac import. In our measurements, HiSiaQM-D304A showed similar HiSiaP binding like HiSiaQM-wt. Hence, the mutation did not significantly influence the initial complex formation of HiSiaP-QM, pointing towards an essential function only later on in the import cycle.

HiSiaQM-D521A also inhibited cell growth, revealing strongly impaired protein function [70]. Currie *et al.*, 2024 identified D521 as part of the substrate binding site in HiSiaQM [12], which points towards HiSiaQM-D521A being a substrate deficient mutant. In our experiments, HiSiaQM-D521A did not show significant differences to HiSiaQM-wt if no Neu5Ac was provided. However, in presence of Neu5Ac, HiSiaQM-D521A showed no increase in binding events, meaning that no conformational coupling could be observed in this case. This suggests that the conformational coupling between HiSiaQM-IFS and HiSiaP$_{closed}$ could be dependent on HiSiaQM's ability to bind Neu5Ac.

3.3.3 Neu5Ac import can be visualized via ALEX smFRET

The next goal was to measure the actual import of Neu5Ac. This was first done via an ALEX smFRET import assay employing surface-immobilized LUVs. To this end, a Neu5Ac sensor was used in the vesicle lumen to recognize imported Neu5Ac. HiSiaP-JF549 and Nb$_{P_{closed}}$-AF647 were chosen as sensor system, due to their larger shift in FRET efficiency. However, as acceptor and donor are individually diffusing molecules, the ratio of donor to acceptor within the LUVs follows a Poisson distribution. To account for this, ALEX smFRET was used. The resulting measurements were performed on surface-immobilized sensor-containing LUVs and visualized as a heatmap of the corrected FRET efficiency versus the corrected stoichiometry.

First, sensor-containing LUVs which were not treated with Neu5Ac were measured as a negative control. For a positive control Neu5Ac was added to the LUV hydration buffer before LUV formation had started, so that Neu5Ac was present in the vesicle lumen together with the sensor proteins. The positive control showed a stark shift to higher FRET efficiencies and lower stoichiometry, indicating that Neu5Ac detection was successful. To overcome the occupancy bias introduced by adding Neu5Ac already before LUV formation, vesicle fusion was used to mimic membrane transport. Neu5Ac delivery via vesicle fusion led to less pronounced shift to lower S' and higher E'. The difference may partly be caused by incomplete vesicle fusion, but it is probably also

due to the Poisson-distributed donor:acceptor occupancy, which reduces the system's response to Neu5Ac import. Thus, this sample could act as the benchmark for the maximal response of the import assay and proves that the assay successfully recognizes Neu5Ac in the vesicle lumen.
In the following, Neu5Ac import in sensor-containing LUVs with HiSiaQM was tested by adding HiSiaP and Neu5Ac into the solution surrounding the LUVs. Neu5Ac addition without HiSiaP did not lead to significant changes in S' and E'. This observation agrees well with the observation of Mulligan *et al.*, 2009 that HiSiaP is necessary to mediate the import [61]. Finally, HiSiaP and Neu5Ac were added and a small but visible shift towards lower corrected stoichiometry S' and higher corrected FRET efficiency E' was observed, pointing towards functional Neu5Ac import under these conditions. While the effect is significant, it is lower than the effect observed via vesicle fusion. Possible reasons for this include the immobilized nature of the LUVs. Close contact to a solid support might attenuate membrane protein mobility, also membrane proteins with large extramembraneous domains may be sterically blocked or partially denatured by direct contact with the support, reducing their activity [9].

3.3.4 Neu5Ac import can be observed via ensemble FRET in GUVs

After the import was visualized via smFRET, an ensemble FRET assay was employed in GUVs. This enabled continuous monitoring of the import progress in real-time which was not possible before, as previous studies relied on sample withdrawal and purification at discrete time intervals to assess import [61] [12]. For the ensemble assay, VcSiaP-AF555-AF647 was used as a Neu5Ac sensor. While this led to a smaller change in FRET efficiency upon binding of Neu5Ac, it guaranteed a stable ratio of donor to acceptor as both are conjugated to one single protein. This was especially helpful since GUV formation was performed by gel swelling and the size differences in $\mathrm{Nb}_{P_{closed}}$ and HiSiaP could lead to a heterogeneity in donor and acceptor distribution among the GUVs. Also, it was shown that VcSiaP is not able to mediate a possible export [69] [61]. This ensures that imported Neu5Ac remained in the GUV lumen. The use of GUVs instead of LUVs allows for an almost completely free-standing membrane system.

Sensor-containing GUVs with HiSiaQM were diluted in buffer solution for imaging. Therefore, VcSiaP-AF555-AF647, that was not encapsulated in the GUV lumen, distributed in the surrounding buffer. This allowed us to determine the raw FRET efficiency E'' of the GUV in- and outside separately. As expected, the data showed a visible increase in in the E'' of the GUV outside solution upon addition of Neu5Ac from the vesicle outside. If no HiSiaP was provided, the raw FRET efficiency E'' inside the GUV, however, increased only slightly over time. The small increase was probably caused by some GUVs exhibiting unspecific leakage. This indicated that while Neu5Ac

was present outside of the GUV, it did not get imported without HiSiaP. If HiSiaP was provided, the E'' of the GUV in- and outside was almost equal. This again underlines that HiSiaP is absolutely necessary for the import to occur.

The import success was used to evaluate protein function. The more this value approached 1, the more Neu5Ac import had occurred. Addition of Neu5Ac in absence of either HiSiaP or a sodium gradient, led to an import success deviating significantly from 1, indicating that Neu5Ac import was attenuated. That agrees very well with previous results of this work. Furthermore, this demonstrates that the sodium gradient is a requirement for the import. This supports Mulligan *et al.*'s findings, who proposed an electrochemical sodium gradient as energy source, driving the import [61].

In the following, mutants of HiSiaP or HiSiaQM were tested for their import success. Importantly, all mutants were tested by providing the wildtype protein counterpart, Neu5Ac and a sodium gradient. The import success for the mutants was measured 20 minutes after Neu5Ac addition. In the following, the results of this work are going to be compared to the effect the same mutants had in SEVY3 cell growth assays, measured by Peter *et al.*, 2022 [70].

Effects of HiSiaP mutants on Neu5Ac uptake

The mutant HiSiaP-S60R essentially abolished cell growth, indicating that protein activity was severely impacted [70]. Substituting serine (S) with the positively charged arginine (R) would likely interfere with a positively charged surface area of HiSiaQM, as the mutation is located on the P-QM interface N-lobe [70]. In our experiments, the mutant also showed a reduced import success when compared to the wild type, supporting the results of the growth assay.

HiSiaP-E172R was also found to inhibit cell growth. The mutation is located in the P-QM interface C-lobe. The change from glutamic acid (E) to arginine (R) would be expected to lead to a charge reversal and additionally to steric clashes as arginine's guanidinium group occupies more space than glutamic acid's carboxylate. Impaired import success was confirmed in our experiments, which aligned with the results of the growth assay.

The mutant HiSiaP-F74A was not tested in the growth assay. The mutation is located adjacent to the periplasmic loop connecting the transmembrane helices Q3 and Q4 of HiSiaQM in the PQM model of Peter et al., 2022 [70]. Exchanging phenylalanine (F) to alanine (A) is not expected to introduce major conformational differences, as both

amino acids are unpolar. In our experiments, HiSiaP-F74A showed a non-significant reduction of import success compared to the wildtype.

Effects of HiSiaQM mutants on Neu5Ac uptake

In the next step, HiSiaQM mutations were investigated. HiSiaQM-W227R was selected to modify the P-QM interface indirectly by displacing the transmembrane helices 3 and 4a of HiSiaQM. This was achieved by introducing the large, charged arginine (R) into the hydrophobic binding pocket of tryptophan (W) [70]. In growth assays, this mutation led to a reduction in cell growth, which was, however, not as substantial as for the aforementioned mutations [70]. In our study, HiSiaQM-W227R did not show significantly decreased import activity compared to the wildtype.

HiSiaQM-E429R carries a mutation at the P-QM interface C-lobe. As described before, the amino acid change from glutamic acid (E) to arginine (R) would be expected to be highly disruptive, which is confirmed by the drastic growth defect observed [70]. For this mutant, only two measurements could be performed, which is why the measured value holds some uncertainty. Yet, our results also indicate attenuated import activity for this mutation.

HiSiaQM-D304A carries a mutation close to one sodium binding site. Currie *et al.*, 2024 found D304 to coordinate the residues of one sodium binding pocket [12]. Exchanging the negatively charged aspartic acid (D) with the small and unpolar alanine (A) is a rather disruptive mutation. It was shown to essentially stop cell growth completely in growth assays [70]. Our measurements also revealed a significantly reduced import success, compared to the wildtype. This underlines that HiSiaQM-D304 is essential for protein activity. Previous results in this work showed a similar number of interactions of this mutant with HiSiaP like HiSiaQM-wt, indicating that the first step of the import seems to be unaffected. This indicates that D304 is required at a later stage, following P–QM complex formation. Interestingly, Goyal *et al.*, 2025 identified a third ion binding site, next to two sodium binding sites, in SiaQM of *Fusobacterium nucleatum*. D304 was part of this third binding site [21]. Longer coordination distances in this site could possibly indicate a weak or transient binding, but the exact function of this site remains unclear [21]. Combining the studies of Goyal *et al.*, 2025 and Currie *et al.*, 2024 it seems plausible that D304 is involved in ion binding of HiSiaQM. Our data supports the essentiality of D304 for successful import and suggests a task after HiSiaP-QM formation. However, it cannot be concluded whether HiSiaQM-D304A influences sodium binding by modifying the binding site indirectly or represents a third, possibly transient, binding site.

Subsequently, HiSiaQM-F111A was tested. The conserved phenylalanine is located in a hydrophobic periplasmic loop of the Q-domain connecting the transmembrane helices Q3 and Q4. As described before, substituting phenylalanine (F) with alanine (A) does not change charge and hydrophobicity of the residue. HiSiaQM-F111A did not show an effect on cell growth. This is in agreement with its import success measured here, which is even slightly exceeding the wildtype.
Substituting the same position with glutamic acid (E) for QM-F111E represents a more severe alteration. The charged glutamic acid side chain could disrupt local secondary structure that relied on the hydrophobicity of phenylalanine (F). This mutant has not been measured in a growth assay yet. In our measurements, QM-F111E showed an impaired import success, which indicates that the periplasmic loop, specifically its hydrophobicity, has a key role during the import.
Subsequently, a HiSiaQM mutant was measured in which a majority of the periplasmic loop was deleted ($\Delta 111-118$). No growth assay data was measured for this mutant. In our experiments, it showed a significant decrease in import activity, underlining again the crucial role of this hydrophobic periplasmic loop.
Possible explanations for its importance were provided by Schneberger *et al.*, 2024 who identified a VHH that led to substrate release in $VcSiaP_{closed}$ by binding to a hydrophobic surface area of VcSiaP [84]. While this hydrophobic area is not strictly conserved, similarities were found among different species. Structural analysis revealed that the hydrophobic surface area of SiaP is located closely to the periplasmic, hydrophobic loop connecting Q3 and Q4 in SiaQM. Due to the proximity, the periplasmic loop could reach the hydrophobic surface area. This suggests that SiaP could be controlled by SiaQM to open on command and release the substrate. This mechanism would not resemble a "scooping" of the substrate, but rather a "push-to-release" [84]. The "push-to-release" mechanism would be advantageous to fulfill two functions: First, it prevents the substrate from rebinding to the SBP, thereby promoting unidirectional transport. Second, it guarantees a successful substrate transfer during which the substrate is not lost into the periplasm [42]. Our results support a "push-to-release" mechanism. While the conserved phenylalanine does not appear to fulfill a specific function, as substitution with alanine is tolerated, its polarity seems to be essential. This would align well with an interaction with the hydrophobic surface area of HiSiaP.

Time-resolved analysis of Neu5Ac uptake

To examine the import time scale, the above described experiments were repeated under continuous image acquisition. The results are in good agreement with the results already gained for the end-point measurements. Effectively, only HiSiaQM-F111A

showed significant import activity next to the wildtype proteins. In these measurements also the mutant QM-R30E has been measured. This mutation is also located at the P-QM interface C-lobe and shows a drastic growth defect [70]. This is also reflected by our measurements, which indicate inhibited import activity. The effect of the R30E mutant cannot be explained by steric clashes in the inward-facing state of the transporter [70]. However, Peter *et al.*, 2022 noted that this residue lies within salt-bridge distance of HiSiaP-E172R, in the outward-facing PQM model [70]. Moreover, HiSiaQM-E429 is found adjacent to HiSiaQM-R30 [70]. Mutation of all these residues led to a loss of protein function in this study, as described previously. This highlights the apparent importance of this region for the interaction between HiSiaP and HiSiaQM.

Next, the influence of the membrane potential on the import activity was tested. In 2009, Mulligan *et al.* found that a membrane potential accelerated Neu5Ac import, although it was not strictly required [61]. Samples with membrane potential exhibited in our measurements a slightly higher import activity than samples with only a sodium gradient. However, no significant differences in import velocity could be derived, indicating that in our experiments membrane potential presence did not significantly accelerate import.

Proposed mechanism for HiSiaPQM

The knowledge gained in this study supports the following cycle for TRAP transporter import of Neu5Ac (figure 61).
The process starts with binding of the substrate by the SBP, which brings the two globular domains of the SBP closer together. This is supported by the high affinity of the SBP to the substrate. In the following step, the bound SBP delivers the substrate to the membrane-inserted QM-domain, which is in the IFS. This interaction is mediated by the conformational coupling that the IFS and specifically P_{closed} exhibit [71]. P_{open} can also interact with HiSiaQM, although in reduced frequency. Furthermore, there are indications that sodium presence is necessary for this process to happen. However, a sodium gradient does not seem to be necessary. After P_{closed} is bound to the QM-domain, the QM-domain uses its monomeric elevator mechanism to transform into the OFS [70]. Presumably, during the conformational changes a conserved hydrophobic loop of the Q-domain executes a "push-to-release" mechanism to open the SBP and trigger substrate transfer to the QM-domain. After the transfer, the substrate then gets co-transported with at least two sodium ions. The success of the import process depends on a sodium gradient, which makes it plausible that this gradient is used as an energy source. During the co-transport, the QM-domain changes into the IFS again. If

there is a conformational coupling present, this could support the detachment of P_{open}. Then, the substrate and the co-transported ions are released into the cytoplasm.

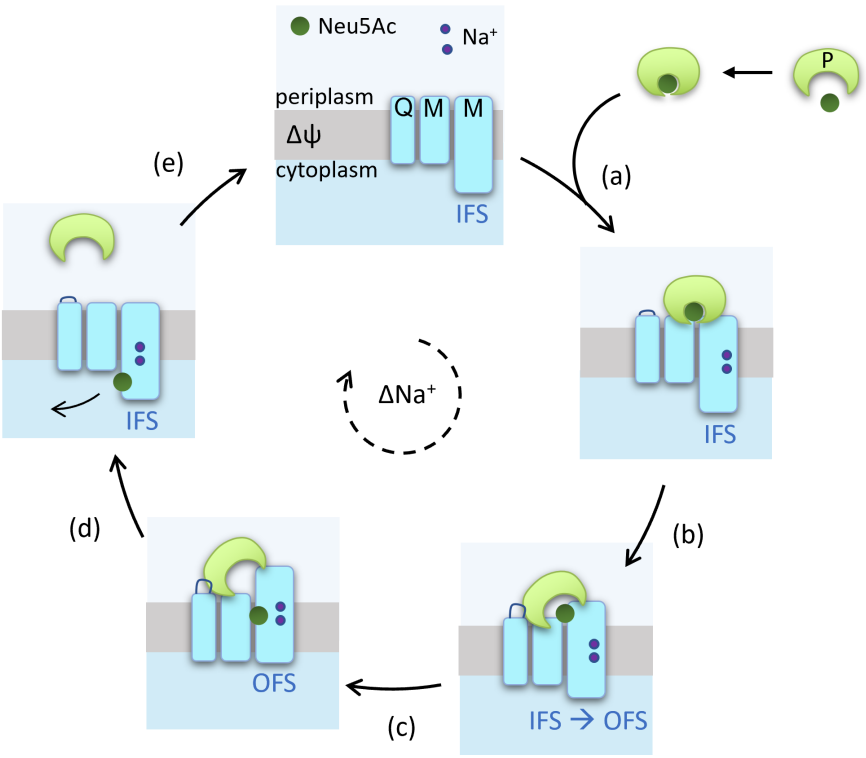


Figure 61: Proposed TRAP transporter cycling model. Schematic overview about the substrate transport cycle of HiSiaPQM. (a) HiSiaP binds Neu5Ac with high nanomolar affinity. The conformational coupling of $HiSiaP_{closed}$ and HiSiaQM-IFS supports binding. The binding is attenuated without sodium. (b) Periplasmic loop of HiSiaQM triggers "push-to-release"-mechanism to mediate Neu5Ac transfer. (c) HiSiaQM binds Neu5Ac. (d) Conformational coupling of $HiSiaP_{closed}$ and HiSiaQM-IFS supports release of $HiSiaP_{open}$. (e) Neu5Ac and sodium ions are released into the cytoplasm.

4 Conclusion and Outlook

In this work, a new approach to form GUVs was developed, which is highly advantageous for future membrane protein research and can be broadly applied. It is an accessible procedure that allows the gentle formation of membrane protein containing GUVs in physiological salt concentrations. It was also possible to establish a membrane potential across the GUV membrane. The complementary advantages of GUVs and LUVs benefitted different experimental purposes. With this combination, I established an artificial platform to investigate membrane transport processes *in vitro* via advanced fluorescence microscopy. I used this to study the membrane transport of the water soluble Neu5Ac as well as the membrane-inserted lipid II.

First, the three most likely lipid II flippase candidates were tested side by side and in presence of a membrane potential for their flipping activity. The obtained results clearly pointed to MurJ as the lipid II flippase. Also, MurJ seems to be able to perform one lipid II flip in absence of a membrane potential, supporting the hypothesis that the membrane potential is utilized to reset from outward- to inward-facing. Furthermore, flipping activity could be stopped by two MurJ inhibitors. Future experiments could utilize mutants of MurJ to identify how specific domains influence the flipping activity. Also, the identity and number of antiported ions involved in the flipping process remains unknown. Testing the influence of different buffer conditions on the flipping activity could elucidate the identity of the antiported ion species. Furthermore, specificity of MurJ flipping should be tested in future experiments. Another open question is whether MurJ is really the only lipid II flippase. From an evolutionary standpoint, it would be reasonable for such a critical process to be safeguarded by multiple, potentially redundant, pathways. In this context, it would be of particular interest to investigate whether the hypothesis by Englehart *et al.*, 2025 holds true that SEDS proteins, in concert with bPBPs, may function as an alternative lipid II flippase [15].

Next, the import of a sialic acid, specifically Neu5Ac, by the TRAP transporter HiSiaPQM was investigated. A single-molecule binding assay revealed that sodium absence attenuates P-QM interaction, while Neu5Ac presence increases the number of interactions. In order to visualize Neu5Ac import, two different Neu5Ac FRET sensor systems were used. Subsequently, Neu5Ac import was demonstrated for the first time via fluorescence microscopy. Neu5Ac import was first measured via ALEX smFRET in LUVs, using the introduced intermolecular labeled sensor system. Future experiments could utilize a connection between the donor- and acceptor-carrying protein to generate a FRET sensor that is not influenced by changing donor to acceptor ratios. Finally, Neu5Ac import was observed time-resolved in an ensemble FRET import assay in

GUVs. This enabled continous monitoring of the import which was not possible before, as previous methods relied on sample withdrawal and purification at discrete time intervals [61] [12]. Ensemble assays were used to identify environmental conditions, as well as certain regions within the TRAP complex, that are required for successful import. The results suggest that HiSiaQM might employ a "push-to-release" mechanism, similar to a scoop-motif that has been found for ABC-transporters that allows a successful transfer of substrate from the SBP to the membrane-inserted protein complex. This hypothesis could be solidified further in the future by proximity tests between the periplasmic loop of HiSiaQM and the allosteric binding pocket of HiSiaP [84]. Close proximity of this regions could potentially be verified by cystein crosslinking as well as smFRET experiments. Furthermore, the exact role of HiSiaQM-D304 remains unclear. Our experiments suggest that this residue has an essential function during import, but does not affect HiSiaP-QM complex formation. Future studies will be required to clarify its role and to test Goyal et al.'s hypothesis of D304A being involved in a third ion binding site.

5 Materials

5.1 Chemicals

Table 3: List of used chemicals with respective manufacturer.

List of chemicals I	
Chemical	**Manufacturer**
AlexaFluor488 NHS Ester	Thermo Fisher Scientific, Schwerte
AlexaFluor647 NHS Ester	Thermo Fisher Scientific, Schwerte
Agarose, ultra low melting	Merck, Darmstadt
Ammonia 30% solution	Carl Roth GmbH, Karlsruhe
Ammoniumpersulfate	Sigma-Aldrich, Taufkirchen
Biotin-phosphatidylethanolamine	Avanti Polar Lipids, Alabaster, AL
Biotin-Bovine serum albumine	Thermo Fisher Scientific, Schwerte
Bovine serum albumine	Sigma Aldrich, Taufkirchen
5(6)-Carboxyfluorescein	Sigma-Aldrich, Taufkirchen
Chloroform	Sigma-Aldrich, Taufkirchen
Cholesterol	Avanti Polar Lipids, Alabaster, AL
Cy5-phosphatidylcholine	Avanti Polar Lipids, Alabaster, AL
Diisopropylethylamine	Carl Roth GmbH, Karlsruhe
Dimethylsulfoxide	Carl Roth GmbH, Karlsruhe
Disodiumhydrogenphosphate-dihydrate	Carl Roth GmbH, Karlsruhe
DNA-oligomer t19-Atto550	Microsynth, Balgach, Switzland
DNA-oligomer t23-Atto550	Microsynth, Balgach, Switzland
DNA-oligomer t31-Atto550	Microsynth, Balgach, Switzland
DNA-oligomer t31-Atto647N-biotin	Microsynth, Balgach, Switzland
DOPC	Avanti Polar Lipids, Alabaster, AL
DOPE	Avanti Polar Lipids, Alabaster, AL
DOTAP	Avanti Polar Lipids, Alabaster, AL
D-Sucrose	AppliChem, Darmstadt
E. coli Polar Lipid Extract	Avanti Polar Lipids, Alabaster, AL
Ethanol	VWR, Darmstadt
FITC-dextran 10 kDa	Sigma-Aldrich, Taufkirchen
FITC-dextran 40 kDa	Sigma-Aldrich, Taufkirchen

List of chemicals II	
Chemical	**Manufacturer**
FITC-dextran 500 kDa	Sigma-Aldrich, Taufkirchen
Glucose	Sigma-Aldrich, Taufkirchen
HEPES	AppliChem GmbH, Darmstadt
Heptakis(2,6-di-O-methyl)-β-cyclodextrin	Sigma-Aldrich, Taufkirchen
Immersionoil Immersol 518	Zeiss, Oberkochen
Methanol	VWR, Darmstadt
N, N-Dimethylformamide	Sigma-Aldrich, Taufkirchen
N-Acetylneuramic acid	Sigma-Aldrich, Taufkirchen
N-dodecyl-β-maltoside	Carl Roth GmbH, Karlsruhe
N-dodecyl-β-thiomaltoside	Anatrace, Maumee, OH
Neutravidin	Thermo Fisher Scientific, Schwerte
NBD NHS Ester	Biomol GmbH, Hamburg
NBD-PE	Avanti Polar Lipids, Alabaster, AL
PageRuler Prestained Protein Ladder	Thermo Fisher Scientific, Schwerte
Phosphomolybdic acid	Sigma-Aldrich, Taufkirchen
POPC	Avanti Polar Lipids, Alabaster, AL
POPG	Avanti Polar Lipids, Alabaster, AL
Potassium chloride	Sigma-Aldrich, Taufkirchen
Rotiphorese Gel 30 (37.5:1)	Carl Roth GmbH, Karlsruhe
Safranine O	Thermo Fisher Scientific, Schwerte
Sodium chloride	Fisher Scientific, Darmstadt
Sodium dithionite	Fisher Scientific, Darmstadt
Sodium hydroxide	Acros Organics, Geel, Belgium
Tetramethylethylendiamine	Merck, Darmstadt
TopFluorPC	Avanti Polar Lipids, Alabaster, AL
Triton X100	Sigma-Aldrich, Taufkirchen

5.2 Instruments and optical devices

Table 4: Used instruments and optical devices with respective manufacturers.

List of instruments	
Instrument	**Manufacturer**
α-Plan-Apochromat-63x/1.46 Oil Corr M27 Obj.	Zeiss, Oberkochen
Apochromat-63x/1.4 Oil Obj.	Zeiss, Oberkochen
Axiovert 200 microscope	Zeiss, Oberkochen
BandPass filter 595/50 ET	AHF analysetechnik, Tübingen
Centrifuge Allegra X-22R	BeckmanCoulter, Krefeld
C-Flex Laserbox	Hübner, Kassel
Dichroic mirror HC 640 sr	AHF analysetechnik, Tübingen
DynaPro NanoStar DLS device	Wyatt Technology, Santa Barbara, CA
ELGA Ultra Analytic Water Purification	Purelab, Salt Lake City, UT
F-2700 fluorescence spectrometer	Hitachi, Hitachinaka, Japan
-80°C freezer	PHC Europe, Breda, Netherlands
Gel Documentation Ingenius	Syngene, Cambridge, UK
Mini Extruder	Avanti Polar Lipids, Alabaster, AL
RCT Heated Plate Magnetic Stirrer	IKA, Staufen
LongPass filter LP650	AHF analysetechnik, Tübingen
nanoDrop 2000 c	Thermo Scientific, Schwerte
Optosplit II	Cairn GmbH, Heidelberg
Pipetus pipetting device	Hirschmann Laborgeräte, Eberstadt
prime BSI sCMOS camera	Teledyne, Thousand Oaks, CA
pHenomenal pH meter	VWR, Darmstadt
Thermomixer C	Eppendorf, Hamburg
TIRF-Quadfilterset 405/488/561/640	AHF analysetechnik, Tübingen
Ultrasound bath	Bandelin Sonorex, Berlin
Vortex mixer Genius 3	IKA, Staufen
Weighing scale PBA124I-1S	VWR, Darmstadt
Zeiss Confocal LSM880	Zeiss, Oberkochen

5.3 Special laboratory consumables

Table 5: Special laboratory consumables with respective manufacturers.

List of used special laboratory consumables	
Material	**Manufacturer**
35-mm-ibidi-μ-dish	Ibidi, Gräfeling
100 nm pore polycarbonate filter	Avanti Polar Lipids, Alabaster, AL
culture-insert-3 well-ibidi-μ-dish	Ibidi, Gräfeling
Filter support 10 mm diameter	Avanti Polar Lipids, Alabaster, AL
Parafilm	Sigma-Aldrich, Taufkirchen
Sephadex PD-10 column	Cytiva, Freiburg
TLC Silica gel 60 F_{254}	Merck KGaA, Darmstadt
Vivaspin 6, MWCO 50,000	Sartorius, Göttingen
Vivaspin Turbo 4, MWCO 100,000	Sartorius, Göttingen

5.4 Software

Table 6: Used software with respective sources.

List of used software	
Software	**Source**
Fiji/ImageJ	Schindelin *et al.*, 2012 [83]
TrackMate	Tinevez *et al.*, 2016 [95]
Gene Snap	Syngene, Cambridge, UK
iSMS	Preus *et al.*, 2015 [73]
Origin 2021b	OriginLab, Northhampton, MA
Zen Black	Zeiss, Oberkochen
Zen Blue	Zeiss, Oberkochen

6 Methods

6.1 Detergent-mediated proteo-GUV swelling

Acrylamide/Bisacrylamide gels were used as a swelling substrate. The gel was prepared by mixing 1.75 mL distilled water with 180 µL Rotiphorese Gel 30 (37.5:1). To start polymerisation, 2 µL TEMED and 20 µL 10% APS were added. 40 µL of this solution were pipetted onto parafilm and a cleaned coverslip was placed on top. After 15 minutes of incubation time, the parafilm was removed and the gel-coated coverslip was dried at 60℃ for 30 minutes on a heating block.

The desired lipid composition was mixed in chloroform and adjusted to concentration of 15 mg/mL. 4 µL of this solution were placed on top of the dehydrated gel substrate and quickly spread as evenly as possible over the entire gel substrate, utilizing a cannula needle. After chloroform evaporation, the lipid coated coverslip could be placed in a well of a 24-well plate. Addition of 200 µL buffer led to immediate vesicle swelling that could be observed easily via brightfield microscopy. The swelling buffer was supplemented with 0.25 mM DOTM and membrane protein, if reconstitution was wished. To allow sedimentation of the GUVs, the swelling buffer was usually prepared using 50 mM sucrose. Swelling was performed at 20℃. If detergent was added, 25 µL of 6 mM cyclodextrin solution were added after 25 minutes of swelling. After 1 h, the swelling was completed and the supernatant solution was taken off the gel substrate to be stored at 4℃. The method was based on developments by [67] and [14].

6.2 LUV preparation via lipid film hydration and extrusion

Large unilamellar vesicles (LUVs) were prepared by the lipid film hydration method followed by freeze–thaw cycling and extrusion, according to established protocols [27]. The desired lipid mixture was dissolved in chloroform and transferred to a 2 mL microcentrifuge tube to be dried under a stream of nitrogen gas to form a thin lipid film on the inner wall of the tube. The dried lipid film was hydrated with aqueous buffer to reach a final lipid concentration of 10 mg/mL. Hydration was performed by vigorous shaking at room temperature for 30 min, resulting in a suspension of multilamellar vesicles. The sample was then subjected to three freeze–thaw cycles by alternating immersion in liquid nitrogen and incubation at room temperature, with gentle mixing between cycles. After this step, the overall sample was distributed into 25 µL aliquots. For storage, the aliquots were kept at -80℃ after the final freezing. Following freeze–thawing, the vesicle suspension was extruded through polycarbonate membranes of 100 nm pore size using a miniextruder (Avanti Polar Lipids) to obtain LUVs of uniform diameter. The final vesicle preparation was stored at 4℃ and used within 5 hours.

If membrane protein reconstitution was wished, the protocol had to be adjusted. Thawed aliquots were mixed with 32 µL of hydration buffer supplemented with 11 mM DDM and the desired membrane protein. After an incubation time of 15 minutes, 44 µL 15 mM cyclodextrin in hydration buffer were added and the final extrusion was performed.

6.3 LUV immobilization via BioBSA-NAv

LUV immobilization was accomplished by incubating an ibidi 35 mm µ-dish with glass bottom (ibidi, Gräfeling) with 200 µL 0.2 mg/mL biotinylated bovine serum albumine (BioBSA) solved in phosphate buffered saline (PBS) for 1 h under constant shaking. Subsequently, the glass bottom was washed by adding and removing 800 µL buffer solution three times. Care was taken not to completely dry out the glass bottom. After washing, 200 µL 0.2 mg/mL neutravidin (NAv) in PBS solution were added and incubated under shaking for 30 minutes. Subsequently, the glass coverslip was washed again for three times by adding and removing 800 µL of buffer. In the last buffer removal, 1 mL of solution was removed. Finally, the LUV solution was added to the µ-dish. After an incubation time of 15 minutes, the sample was again washed for three times to remove unbound vesicles and finally adjusted to 800 µL of sample volume. The method was based on [98].

6.4 LUV immobilization via agarose

LUV immobilization in a 3D-space could be accomplished via low melting (LM) agarose. 1 g LM agarose was combined with 100 mL buffer solution, so that equimolar solutions in- and outside of the LUVs were reached. The solution was heated in the microwave until the powder had dissolved. The LM agarose solution was left to cool down until a temperature of about 40℃ was reached. Then, vesicles and LM agarose solution were combined in a volume ratio of 1:1 and mixed carefully by pipetting slowly up and down. The solution was added onto an ibidi µ-dish and left at room temperature for at least 10 minutes for agarose jellification. The method was based on [46].

6.5 Dithionite quenching assay

Sodium dithionite quenching is a technique which is suitable to asses phospholipid orientation. The here used method was based on developments by [51] and [56].

Sodium dithionite stock solution preparation

A 1 M sodium dithionite stock solution was freshly prepared immediately before use by dissolving the compound in 1 M Tris-HCl buffer, pH 10.0. The stock was kept on ice and used within 30 minutes of preparation.

Dithionite quenching for GUVs

E. coli PL/POPC/NBD-PE (3:1:0.1) GUVs were prepared in 150 mM KCl/10 mM Na_2HPO_4/ 50 mM sucrose, pH 7.8 solution. In the following, GUVs were diluted 1:20 in 150 mM NaCl/10 mM Na_2HPO_4/50 mM sucrose, pH 7.8 solution and deposited in an ibidi µ-dish. Confocal imaging was done using a Zeiss LSM880 and an α-Plan-apochromat 63x/1.46 Oil Korr M27 objective. Excitation of NBD-PE was done at 488 nm and a laser power of 2%. The confocal pinhole was opened to 1 Airy unit (AU). After focusing the sedimented GUVs, a focus stabilization was employed by using the Zeiss definite focus system. Subsequently, a time series measurement with an interval time of 30 s was started. After acquisition of two frames, 0.5 µL of a 1 M dithionite stock solution were added to 800 µL sample volume on the microscope without changing the imaging position in the sample. Care was taken that imaging was restarted after 30 s. Subsequently, another time series was acquired with the same imaging parameters. For this time series, 6 frames were acquired.

Dithionite quenching for LUVs

LUVs were prepared in 150 mM KCl/10 mM Na_2HPO_4, pH 7.8 solution and surface-immobilized as described before. The extravesicular solution was exchanged to 150 mM KCl/10 mM Na_2HPO_4, pH 7.8. Confocal imaging of the NBD-labeled lipids containing LUVs was done using a Zeiss LSM880. The sample was then mounted onto the microscope's sample holder. Imaging was done with an α-Plan-apochromat 63x/1.46 Oil Korr M27 objective. Excitation of lipid II-NBD was done at 488 nm and a laser power of 1%. The pixel dwell was set to 1.78 µs, while the confocal pinhole was opened to 1 AU. After focusing the surface-immobilized LUVs, a focus stabilization was employed by using the definite focus system. Then, a time series measurement with an interval time of 30 s was started. Minimally five frames were acquired. Then, 0.5 µL of a 1 M dithionite stock solution were added to 800 µL sample volume on the microscope without changing the imaging position in the sample. Care was taken that imaging was restarted after 30 s. Subsequently, another time series was acquired with the same imaging parameters. For this time series, minimally 11 frames were acquired.

6.6 Membrane potential establishment and measurement

The membrane potential is an important membrane property that needed to be replicated in artificial membranes. The methods used here were based on [5].

Membrane potential in GUVs

DOPC GUVs were formed in 150 mM KCl, 5 mM HEPES and 50 mM sucrose, pH 7.2 and diluted 1:20 in either 150 mM NaCl, 5 mM HEPES and 50 mM glucose, pH 7.2 or 150 mM KCl, 5 mM HEPES and 50 mM glucose, pH 7.2. Safranin was added in a concentration of 6 µM to indicate the membrane potential. Valinomycin, if added, was supplied in a concentration of 5 µM. Safranin fluorescence intensity in the vesicle lumen was imaged via confocal imaging on a Zeiss LSM880. Excitation was performed via a 488 nm laser and a laser power of 1%. An α-Plan-apochromat 63x/1.46 Oil Korr M27 objective was used for imaging. Imaging was performed manually by scanning through the sample and acquiring individual images.

Membrane potential in LUVs

DOPC/BioPE (100:1) LUVs were formed in 150 mM KCl, 5 mM HEPES, pH 7.2 and then surface-immobilized. Afterwards, the LUVs could be washed be 3 times by adding and removing 600 µL 150 mM NaCl, 5 mM HEPES, pH 7.2. Safranin was added in a concentration of 6 µM to indicate the membrane potential. Valinomycin was added in a concentration of 5 µM. Safranin fluorescence intensity in the vesicle lumen was imaged via confocal imaging on a Zeiss LSM880. Imaging was started immediately after valinomycin addition. Excitation was performed via a 488 nm laser and a laser power of 2%. An α-Plan-apochromat 63x/1.46 Oil Korr M27 objective was used for imaging. After focusing the surface-immobilized LUVs, a focus stabilization was employed by using the definite focus system. Then, a time series measurement with an interval time of 30 s was started and 39 frames were acquired.

6.7 Dynamic light scattering

Dynamic light scattering measurements were performed using a DynaPro NanoStar (Wyatt Technology). LUV samples were prepared in 150 mM NaCl/5 mM HEPES (pH 7.2), as described before. Sample preparation was performed detergent-mediated and without the addition of detergent. Each sample was measured directly after preparation and also after 5 hours at 4°C. For each sample, 20-25 runs with a measurement duration of 10 seconds each were recorded.

6.8 Preparation of positively charged LUVs for vesicle fusion

In order to promote vesicle fusion, positively charged LUVs were synthesized from DOPE/10 mol% DOTAP with substituted fluorescent lipids, when necessary. The lipids were solved in a concentration of 5 mM in 20 mM Triton X-100/150 mM NaCl/5 mM HEPES (pH 7.2). If cargo was wished in the experiment, it was additionally added to the solution. The lipid-solution was then diluted 1:2 in 150 mM NaCl/5 mM HEPES (pH 7.2) and finally combined with an equal volume of 13 mM cyclodextrin solution. The mixture was vortexed for 2 minutes. Vesicles were used within one hour. The method was based on [44] and [22].

6.9 Protein purification and labeling

Different proteins and their mutants were heterologously expressed in *E. coli* and, subsequently, purified using affinity chromatography, followed by high-performance liquid chromatography (HPLC). The protein preparation of TRAP transporter related proteins was carried out by Philipp Hendricks from the workgroup of Dr. Gregor Hagelüken (Institute of Structural Biology, University of Bonn). The protein preparation of lipid II flippase related proteins was carried out by Mara Bingel from the workgroup of Dr. Anna Müller (Institute of Pharmaceutical Microbiology, University of Bonn). In the following, all used proteins are listed. The organisms, the proteins originate from, are indicated in front of the protein: *Staphylococcus aureus* (Sa), *Haemophilus influenzae* (Hi) or *Vibrio cholerae* (Vc).

Table 7: Proteins used in this study and respective sources.

Protein Mutants	
Protein	**preparation by**
HiSiaQM-wt	Philipp Hendricks
HiSiaP-wt	Philipp Hendricks
HiSiaQM-F111A	Philipp Hendricks
HiSiaQM-F111E	Philipp Hendricks
HiSiaQM-loop deletion Δ111-118	Philipp Hendricks
HiSiaQM-D304A	Philipp Hendricks
HiSiaQM-D521A	Philipp Hendricks
HiSiaQM-R30E	Philipp Hendricks
HiSiaQM-E429R	Philipp Hendricks
HiSiaQM-W227R	Philipp Hendricks
HiSiaP-E172R	Philipp Hendricks
HiSiaP-F74A	Philipp Hendricks
HiSiaP-S60R	Philipp Hendricks
VcSiaP-AF555-AF647	Philipp Hendricks
$Nb_{HiSiaQM}$	Philipp Hendricks
$Nb_{P_{closed}}$-AF647	Philipp Hendricks
HiSiaP-JF549	Philipp Hendricks
SaMurJ-wt	Mara Bingel
SaFtsW-wt	Mara Bingel
SaRodA-wt	Mara Bingel

6.9.1 Protein labeling with NHS-ester conjugated dye

Different proteins were labeled with an N-hydroxysuccinimide (NHS) ester-functionalized fluorescent dye under mildly basic conditions to enable covalent attachment to primary amines. For each labeling reaction, protein was diluted in 100 mM sodium hydrogen carbonate buffer, pH 8.0, to the desired concentration. Depending of the available amount of protein, the concentration range was adjusted to be between 0.5 mg/mL and 2 mg/mL. The NHS ester dye was prepared as a solution in anhydrous dimethyl sulfoxide (DMSO), which was frozen in aliquots. Single aliquots were thawed immediately prior to use and added to the protein solution at a molar ratio appropriate for the desired labeling density. Usually a ratio of 1:5 (protein to dye) was used. The reaction mixture was gently mixed and incubated for 2 h at room temperature, protected from light.

Excess unreacted dye was removed by size-exclusion chromatography, using a Sephadex pre-prepared desalting column, which was equilibrated with the appropriate storage buffer. The labeled protein was, subsequently, concentrated using an Amicon centrifugal ultrafiltration device with a molecular weight cut-off suitable for the protein of interest. Protein concentration was determined by using a nanoDrop 2000 c and the degree of labeling was calculated from absorbance measurements at the dye's maximum absorbance wavelength and 280 nm.
The procedure was performed similarly for membrane proteins, however, it was ensured that an adequate detergent amount had to be present at all times, as otherwise the membrane proteins would have aggregated and denatured during the process.

6.9.2 SDS-PAGE

Protein samples were analyzed by sodium dodecyl sulfate–polyacrylamide gel electrophoresis (SDS–PAGE) under denaturing conditions using a 12% resolving gel. Samples were mixed 1:1 (v/v) with 2× Laemmli sample buffer containing 5% (v/v) β-mercaptoethanol. Water soluble proteins were heated at 95℃ for 5 min to ensure complete denaturation and reduction of disulfide bonds. Membrane proteins were incubated for 1 hour at 37℃.

Gels were cast with a 12% polyacrylamide resolving layer and a 5% stacking layer. Therefore, for one resolving gel 2.4 mL of distilled water were combined with 3 mL of Rotiphorese gel (37.5:1), 1.95 mL 1.5 M Tris (pH 8.8) and 75 µL 10% SDS solution. Polymerization of the resolving layer was started by addition of 75 µL 10% ammonium persulfate (APS) and 3 µL N,N,N′,N′-tetramethylethylenediamine (TEMED). The solution was poured between two glass slides immediately after APS and TEMED

addition. After 30 minutes, the stacking gel was prepared of 1.36 mL of distilled water, 0.34 mL Rotipohorese Gel 30 (37.5:1), 0.26 mL 1 M Tris (pH 6.8) and 20 µL 10% SDS solution. Polymerization was started upon 10 µL 10 % APS and 2 µL TEMED addition. The stacking gel was poured on top of the already polymerized resolving gel and subsequently a comb was pushed into the stacking gel to make space for the sample solutions. Polymerization was finished after another 30 minutes. The denatured protein samples were loaded into the wells after comb removal. The sample volume was adjusted to the protein concentration. Electrophoresis was performed in Tris–glycine–SDS running buffer (25 mM Tris, 192 mM glycine, 0.1% SDS, pH 8.3) at a constant voltage of 150 V. Molecular weight markers were run in parallel for size estimation.

6.10 Lipid labeling

Lipid labeling was performed by dissolving the fluorescent dye, conjugated to an NHS ester in dimethylformamide (DMF), and mixing it thoroughly with the desired lipid components in a ratio of 5:1 (dye:lipid). Only lipids with a primary amine could be labeled. Additionally, the organic base diisopropylethylamine (DIPEA) was added to reach 1 vol% of the labeling solution. The reaction was carried out for 2 hours at room temperature.

Thin layer chromatography (TLC) was used to verify lipid composition and labeling efficiency. Lipid samples were spotted onto silica gel TLC plates (Merck KGaA, Darmstadt) and run in a solvent system of chloroform:methanol:water:ammonia 65:25:4:1 v/v/v/v. Fluorescent lipids were visualized using a UV lamp or by eye, if possible. Lipid species were identified via a phosphomolybdic acid (PMA) staining. To do so, the TLC plates were coated with PMA solution in and then placed on a heating plate, at 131℃. After about 1 minute, blue lines indicated the position of the lipid bands on the TLC plate. Silica gel plates that were not used for PMA labeling could be used to purify the labeled lipid from, by scraping the correct band off and incubating the silica gel powder in methanol for 15 minutes. Then, the mixture was centrifuged (Centrifuge Allegra X-22R, Beckman Coulter) at 1000 rpm for 10 minutes before the supernatant could be separated from the silica gel.

The concentration of fluorescent lipids in the supernatant was determined spectroscopically. Therefore, the sample was measured in a F-2700 fluorescence spectrometer (Hitachi, Hitachinaka, Japan) and, subsequently, the Lambert-Beer law was employed to estimate the concentration.

6.11 Stimulated emission depletion microscopy

Large unilamellar vesicles (LUVs) were imaged using a Stedycon STED microscope (Abberior Instruments GmbH, Göttingen) [24]. Vesicles were prepared and immobilized on glass coverslips, as described above. The fluorescently labeled lipid Atto647N-PE was incorporated into DOPC/BioPE LUVs to enable STED imaging. Excitation was performed using a 640 nm laser, while fluorescence depletion was achieved using a STED laser beam at a wavelength of 775 nm. Confocal and STED images of the same field of view were recorded sequentially to assess resolution enhancement. The excitation laser power was set to 3.8% for STED imaging and 1.8% for confocal imaging. The STED laser power was set to 23.4%. Image acquisition and hardware control were carried out using the Stedycon control software (Abberior Instruments GmbH). Pixel dwell time was set to 10 µs (STED) and 5 µs (confocal), with a line frequency of 132 Hz for both. Three line accumulations were performed for STED, while only one was performed for confocal imaging. Pixel size for STED was set to 24 nm and 70 nm for confocal imaging.

6.12 Single-molecule imaging

The single-molecule measurements have been performed on a Total Internal Reflection Fluorescence (TIRF) setup, built into a commercial Zeiss LSM880 [80]. The setup included a C-Flex laserbox with the Cobolt lasers emitting 405 nm, 488 nm, 561 nm and 634 nm light. An α-Plan apochromat TIRF 63x, 1.46 NA oil immersion objective was used for the measurements. Detection was done by a the Photometrics primeBSI camera with a pixel size of 6.5 x 6.5 µm. Separate detection paths for the two-channel emission were established by using an Optosplit II. The dichroic mirror, used for the beam separation, was the F38-640-T3, Strahlenteiler HC 640 sr, additionally, two optical filters were used to clean up the emission light in the respective emission light path: LP650 and F47-595, 595/50 ET Bandpass.

6.12.1 Single-molecule HiSiaP-AF647 LUV binding assay

DOPC/BioPE/TopFluorPC (100:1:0.1) LUVs were prepared in either KCl-buffer (150 mM KCl/5 mM HEPES pH 7.2) or NaCl-buffer (150 mM NaCl/5 mM HEPES pH 7.2). HiSiaQM was reconstituted in a protein to lipid ratio of 1:10,000. Subsequently, the LUVs were surface-immobilized on a BioBSA/NAv pre-treated ibidi µ-dish and washed with NaCl- or KCl-buffer. 2 nM HiSiaP-AF647 were added to the sample. Additionally, 3 µM of sialic acid were added, if desired. During imaging, focus was always carefully adjusted to the TopFluor-PC signal in the LUVs, which was excited by a 405 nm laser. The focus was stabilized during the measurements by the definite focus system. For data acquisition, 1000 frames using 6% 638 nm laser excitation were acquired. The

exposure time was set to 10 ms and only the central 200 x 200 pixels of the camera chip were evaluated. Tracking of single P-domains was performed using the TrackMate plug-in for ImageJ/Fiji [83]. For spot detection, the LoG-based detector was chosen. The parameter 'estimated blob diameter' was set to 0.75 µm and 'sub-pixel localisation' was activated. A threshold of 1 was used for spot filtering. For tracking the 'Simple LAP Tracker' was chosen. Gap closing was allowed with a maximum closing distance of 1 µm and a maximum frame gap of two frames. The maximum linking distance was set to 1 µm. Each track is considered as a single interaction of the P-domain with the immobilized LUVs.

6.12.2 Single-molecule FRET calibration measurement

The DNA oligomers used here were commercially synthesized by Microsynth Seqlab GmbH, Göttingen, corresponding to those used in a multi-laboratory smFRET benchmark study by Hellenkamp *et al.*, 2018 [25]. Single-stranded DNA oligonucleotides had to be annealed to yield double stranded DNA. The oligonucleotides were reconstituted to a stock concentration of 100 µM. Equimolar working stocks were prepared in 1x annealing buffer (10 mM Tris-HCl, pH 7.5, 50 mM NaCl, 1 mM EDTA). For annealing, equal volumes of the two strands were mixed to give a final concentration of 5 µM per strand in 1x annealing buffer. Heating was performed in a pre-heated heat block at 95℃ for 5 min, after which the block was switched off and allowed to cool gradually to room temperature before transferring the samples to ice. Annealed oligonucleotides were stored as aliquots at -20℃. To image the sample, the annealed strands were added to a glass coverslip, coated with BioBSA and NAv, prepared as described before. NAv binding to the biotinylated DNA strand, resulted in immobilization of the DNA strands. Finally, the measurement was performed by using 35% laser power of the DPL 561 nm laser line (Hübner Photonics, Kassel) for excitation. The donor and the acceptor emission channel were imaged simultaneously by using the filtersets described above. The exposure time was set to 10 ms and 100 frames were acquired for each measurement. Evaluation was performed via the software iSMS [73]. The mode was set to single-wavelength excitation and $\alpha = 0$, $\delta = 0$ and $\gamma = 1$. Channel alignment was performed automatically but visually checked. Only overlays between donor and acceptor emission channel (A_D and D_D) were considered for evaluation. The raw FRET efficiency was calculated by the software and exported to Origin2021b (Originlab, Northhampton, MA), where the data was plotted as a histogram.

6.12.3 ALEX single molecule FRET measurements

LUVs were prepared containing 1.3 µM $Nb_{P_{closed}}$-AF647 and 1.3 µM HiSiaP-JF549, as 1.3 µM was calculated to be the concentration at which on average exactly one

molecule was present in the LUV lumen for the average LUV radius determined for detergent-mediated LUV formation via DLS (67 nm). 150 mM KCl/5 mM HEPES pH 7.2 was used as hydration buffer for the formation. Subsequently, LUVs were surface-immobilized onto an ibidi µ-dish and the extravesicular solution was exchanged to 50 mM NaCl/5 mM HEPES pH 7.2.

To establish alternating-laser excitation (ALEX), donor (561 nm) and acceptor (638 nm) excitation was alternated, each image had an exposure time of 50 ms and in total 20 frames were acquired for each measurement. The 638 nm excitation was performed at 3% laser power, while 561 nm excitation was set to 35%. Fluorescence emission was split spectrally using the Optosplit II, and donor and acceptor emission were detected simultaneously.

Evaluation of ALEX data was performed via iSMS. Therefore, the mode was set to alternating-laser excitation and $\alpha = 0.061$, $\delta = 0.117$ and $\gamma = 1$. Channel alignment was performed automatically but visually checked. Only overlays between D_D and A_A channel were considered for evaluation. Stoichiometry and corrected FRET efficiency were calculated by the software and the data was exported to Origin2021b (OriginLab, Northhampton, MA), where it was plotted as a heatmap with bin size of 0.1 for x- and y-axis.

6.13 Ensemble FRET measurements in solutions

To measure FRET for freely diffusing molecules, a solution containing donor- and acceptor-fluorophore was prepared. An ibidi-µ-dish was passivated via 1% BSA solved in PBS. After 10 minutes of incubation time, three washing steps were executed. After that, the sample solution could be added into the dish. Measurements were performed via the Zeiss LSM880. Care was taken that all solution measurements were taken in a Z-plane at 15 µm distance to the coverslip. 561 nm excitation was used while two separate emission channels were acquired: 650-680 nm (A_D) and 565-595 nm (D_D). The raw FRET efficiency E" could then be calculated with the mean values of the images acquired for A_D and D_D.

6.14 Ensemble FRET measurements in GUVs

Ensemble FRET measurements in GUVs were performed by preparing GUVs as described earlier. VcSiaP-AF555-AF647 was added into the swelling buffer (150 mM KCl/50 mM sucrose/5 mM HEPES pH 7.2) in a concentration of 60 nM. GUVs were prepared from *E. coli* PL/POPC/TopFluor PC (3:1:0.01). Then, GUVs were diluted 1:20 in 150 mM NaCl/5 mM HEPES/50 mM glucose pH 7.2 buffer to yield a complete

sample volume of 100 µL. For imaging, an ibidi culture-insert 3 well µ-dish was used. The surface was passivated via 1% BSA solved in PBS. After 10 minutes of incubation time, three washing steps were executed. Then, the GUV containing solution was added into the µ-dish and mounted onto the Zeiss LSM880. An Apochromat 63x/1.4 Oil immersion objective was used for imaging. Two emission channels were acquired for 2% 561 nm excitation: 650-680 nm (A_D) and 565-595 nm (D_D). The GaAsP detector with a gain of 750 was used for detection. Additionally, another channel was acquired to image the lipid marker TopFluor PC (0.5% 488 nm excitation, 495-520 nm emission). A 3x3 tile scan image was acquired with focus stabilization via the definite focus system. Neu5Ac and HiSiaP were added with 15 µM and 5 µM, respectively. Directly after, a timeseries-tilescan measurement was started, imaging all three previously described channels after each other.

Evaluation was performed individually for the GUV inside- and outside-solution. Therefore, the following macro was developed to segment the vesicle in- and outside and to calculate the raw FRET efficiency E'' of the extravesicular solution automatically (figure 62).

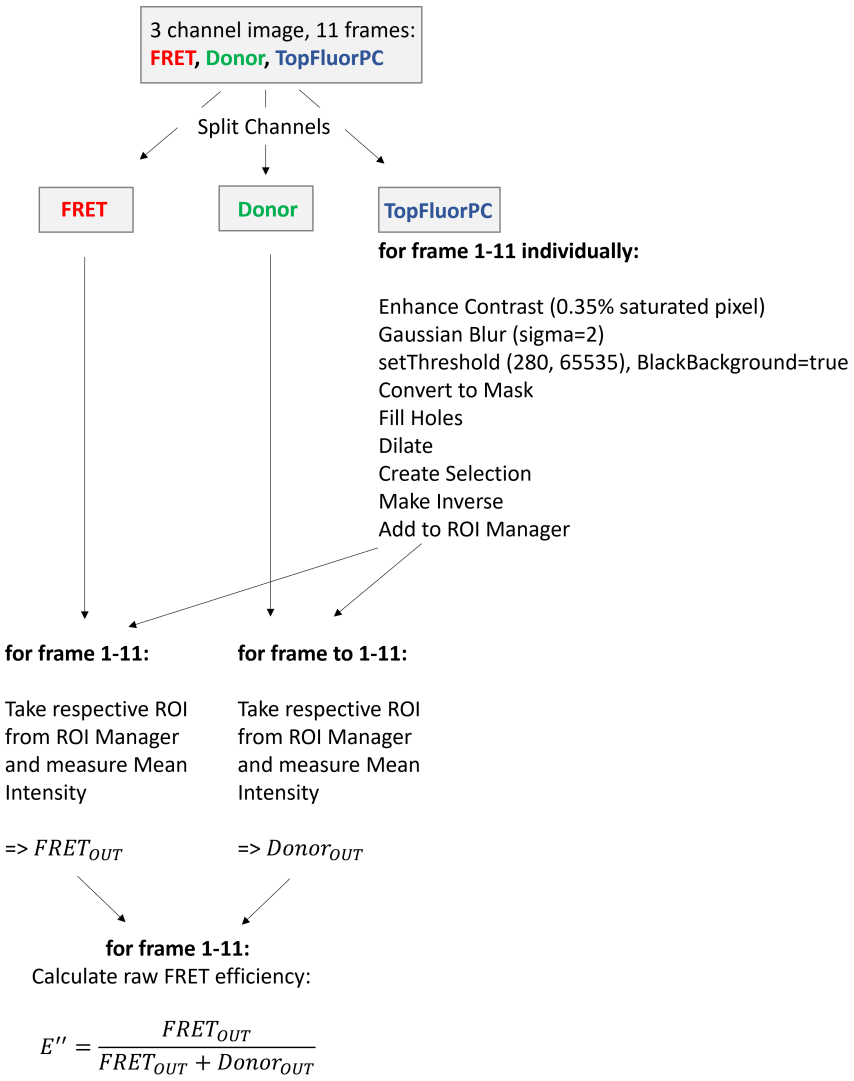


Figure 62: ImageJ Macro workflow. Schematic depiction of the macro used to segment GUVs based on their TopFluor PC channel into GUV_{OUT} and GUV_{IN}.

First, the Macro split all three channels and used the TopFluor PC channel for segmentation. It enhanced the contrast (0.35%, saturated pixel) and applied a Gaussian blur filter (sigma=2). After that a threshold was set and the image was converted to a mask. In the next step, holes were filled and the mask was dilated. After that a the mask was turned into a selection and then into an inverse of the selection. This selection was then added to the ROI manager and could be used to measure the average fluorescence intensity in the selected region for the donor- and the FRET-channel. These values could be used to calculate the raw FRET efficiency. This procedure was repeated for every time series frame individually. Raw FRET efficiency calculation for the solution inside the GUVs was performed by manually placing ROIs into the GUVs and then determining the raw FRET efficiency value of each GUV individually.

References

1. Ajmal, M. R. Protein Misfolding and Aggregation in Proteinopathies: Causes, Mechanism and Cellular Response. *Diseases.* **11,** 30 (2023).
2. Allen, S., Zaleski, A., Johnston, J. W., Gibson, B. W. & Apicella, M. A. Novel sialic acid transporter of Haemophilus influenzae. *Infect. Immun.* **73,** 5291–5300 (2005).
3. Althoff, T., Davies, K. M., Schulze, S., Joos, F. & Kühlbrandt, W. GRecon: a method for the lipid reconstitution of membrane proteins. *Angew. Chem. Int. Ed. Engl.* **51,** 8343–8347 (2012).
4. Angelova, M. I. & Dimitrov, D. S. Liposome electroformation. *Faraday Discuss. Chem. Soc.* **81,** 303–311 (1986).
5. Bally, M., Hope, M., Van Echteld, C. & Cullis, P. Uptake of safranine and other lipophilic cations into model membrane systems in response to a membrane potential. *Biochimica et Biophysica Acta (BBA) - Biomembranes* **812,** 66–76 (1985).
6. Benarroch, J. & Asally, M. The Microbiologist's Guide to Membrane Potential Dynamics. *Trends in Microbiology* **28,** 304–314 (2020).
7. Bothe, A., Zouni, A. & Müh, F. Refined definition of the critical micelle concentration and application to alkyl maltosides used in membrane protein research. *RSC Adv.* **13,** 9387–9401 (2023).
8. Cardozo, D. An intuitive approach to understanding the resting membrane potential. *Adv. Physiol. Educ.* **40,** 543–547 (2016).
9. Castellana, E. T. & Cremer, P. S. Solid supported lipid bilayers: From biophysical studies to sensor design. *Surf. Sci. Rep.* **61,** 429–444 (2006).
10. Chan, Y. H. & Boxer, S. G. Model membrane systems and their applications. *Curr. Opin. Chem. Biol.* **11,** 581–587 (2007).
11. Clary, L., Verderone, G., Santaella, C. & Vierling, P. Membrane permeability and stability of liposomes made from highly fluorinated double-chain phosphocholines derived from diaminopropanol, serine or ethanolamine. *Biochimica et Biophysica Acta (BBA) - Biomembranes* **1328,** 55–64 (1997).
12. Currie, M. J. *et al.* Structural and biophysical analysis of a *Haemophilus influenzae* tripartite ATP-independent periplasmic (TRAP) transporter. *eLife* **12,** RP92307 (2024).

13. Degrip, W. J., Vanoostrum, J. & Bovee-Geurts, P. H. Selective detergent-extraction from mixed detergent/lipid/protein micelles, using cyclodextrin inclusion compounds: a novel generic approach for the preparation of proteoliposomes. *Biochem. J.* **330,** 667–674 (1998).

14. Dezi, M., Cicco, A. D., Bassereau, P. & Lévy, D. Detergent-mediated incorporation of transmembrane proteins in giant unilamellar vesicles with controlled physiological contents. *Proc. Natl. Acad. Sci. U.S.A.* **110,** 7276–7281 (2013).

15. Englehart, K. & Dworkin, J. Bacillus subtilis MurJ and Amj Lipid II flippases are not essential for growth. *J. Bacteriol.* **207,** e00078–25 (2025).

16. Erickson, H. P. Size and Shape of Protein Molecules at the Nanometer Level Determined by Sedimentation, Gel Filtration, and Electron Microscopy. *Biol. Proced. Online* **11,** 32–51 (2009).

17. Eytan, G. D. Use of liposomes for reconstitution of biological functions. *Biochimica et Biophysica Acta (BBA) - Reviews on Biomembranes* **694,** 185–202 (1982).

18. Fish, K. N. Total internal reflection fluorescence (TIRF) microscopy. *Curr. Protoc. Cytom.,* DOI: 10.1002/0471142956.cy1218s50 (2009).

19. Förster, T. Energiewanderung und Fluoreszenz. *Naturwissenschaften* **33,** 166–175 (1946).

20. Garten, M., Aimon, S., Bassereau, P. & Toombes, G. E. Reconstitution of a Transmembrane Protein, the Voltage-gated Ion Channel, KvAP, into Giant Unilamellar Vesicles for Microscopy and Patch Clamp Studies. *J. Vis. Exp.* **95,** 52281 (2015).

21. Goyal, P. *et al.* Molecular determinants of Neu5Ac binding to a tripartite ATP independent periplasmic (TRAP) transporter. *eLife* **13,** RP98158 (2025).

22. Grein, F. *et al.* Ca2+-Daptomycin targets cell wall biosynthesis by forming a tripartite complex with undecaprenyl-coupled intermediates and membrane lipids. *Nat. Commun.* **11,** 1455 (2020).

23. Ha, T. *et al.* Probing the interaction between two single molecules: fluorescence resonance energy transfer between a single donor and a single acceptor. *Proc. Natl. Acad. Sci. U.S.A.* **93,** 6264–6268 (1996).

24. Hell, S. W. & Wichmann, J. Breaking the diffraction resolution limit by stimulated emission: stimulated-emission-depletion fluorescence microscopy. *Opt. Lett.* **19,** 780–782 (1994).

25. Hellenkamp, B. *et al.* Precision and accuracy of single-molecule FRET measurements—a multi-laboratory benchmark study. *Nat. Methods* **15,** 669–676 (2018).

26. Hohlbein, J., Craggs, T. D. & Cordes, T. Alternating-laser excitation: single-molecule FRET and beyond. *Chem. Soc. Rev.* **43 4,** 1156–1171 (2014).

27. Hope, M., Bally, M., Webb, G. & Cullis, P. Production of large unilamellar vesicles by a rapid extrusion procedure. Characterization of size distribution, trapped volume and ability to maintain a membrane potential. *Biochimica et Biophysica Acta (BBA) - Biomembranes* **812,** 55–65 (1985).

28. Horger, K. S., Estes, D. J., Capone, R. & Mayer, M. Films of Agarose Enable Rapid Formation of Giant Liposomes in Solutions of Physiologic Ionic Strength. *J. Am. Chem. Soc.* **131,** 1810–1819 (2009).

29. Huang, C. & Thompson, T. Preparation of homogeneous, single-walled phosphatidylcholine vesicles. *Methods in Enzymology* **32,** 485–489 (1974).

30. Huber, J. *et al.* Chemical genetic identification of peptidoglycan inhibitors potentiating carbapenem activity against methicillin-resistant Staphylococcus aureus. *Chem Biol.* **16,** 837–848 (2009).

31. Hvorup, R. N. *et al.* The multidrug/oligosaccharidyl-lipid/polysaccharide (MOP) exporter superfamily. *Eur. J. Biochem.* **270,** 799–813 (2003).

32. Kapanidis, A. N. *et al.* Fluorescence-aided molecule sorting: analysis of structure and interactions by alternating-laser excitation of single molecules. *Proc. Natl. Acad. Sci. U.S.A.* **101,** 8936–8941 (2004).

33. Kelly, D. J. & Thomas, G. H. The tripartite ATP-independent periplasmic (TRAP) transporters of bacteria and archaea. *FEMS Microbiology Reviews* **25,** 405–424 (2001).

34. Khatua, B., Roy, S. & Mandal, C. Sialic acids siglec interaction: a unique strategy to circumvent innate immune response by pathogens. *Indian. J. Med. Res.* **138,** 648–662 (2013).

35. Kragh-Hansen, U., le Maire, M. & Møller, J. V. The mechanism of detergent solubilization of liposomes and protein-containing membranes. *Biophys. J.* **75,** 2932–2946 (1998).

36. Kuhn, P. *et al.* A facile protocol for the immobilisation of vesicles, virus particles, bacteria, and yeast cells. *Integr. Biol.,* 1550–1555 (2012).

37. Kuk, A. C. Y., Hao, A. & Lee, S. Structure and Mechanism of the Lipid Flippase MurJ. *Annu. Rev. Biochem.* **91,** 705–729 (2022).

38. Kumar, S., Rubino, F. A., Mendoza, A. G. & Ruiz, N. The bacterial lipid II flippase MurJ functions by an alternating-access mechanism. *J. Biol. Chem.* **294,** 981–990 (2019).

39. Kwapiszewski, R. *et al.* Effect of a high surface-to-volume ratio on fluorescence-based assays. *Anal. Bioanal. Chem.* **403,** 151–155 (2012).

40. Leomil, F. S. C., Stephan, M., Pramanik, S., Riske, K. A. & Dimova, R. Bilayer Charge Asymmetry and Oil Residues Destabilize Membranes upon Poration. *Langmuir* **40,** 4719–4731 (2024).

41. Li, F. *et al.* Highlighting membrane protein structure and function: A celebration of the Protein Data Bank. *J Biol Chem.* **296,** 100557 (2021).

42. Li, P., Zhang, M. & Huang, Y. Structural characterization of the ABC transporter DppABCDF in Escherichia coli reveals insights into dipeptide acquisition. *PLoS Biol.* **23,** e3003026 (2025).

43. Li, Q., Wang, X., Ma, S., Zhang, Y. & Han, X. Electroformation of giant unilamellar vesicles in saline solution. *Colloids and Surfaces B: Biointerfaces* **147,** 368–375 (2016).

44. Lira, R. B., Robinson, T., Dimova, R. & Riske, K. A. Highly Efficient Protein-free Membrane Fusion: A Giant Vesicle Study. *Biophys. J.* **116,** 79–91 (2019).

45. Lira, R. B., Dimova, R. & Riske, K. A. Giant Unilamellar Vesicles Formed by Hybrid Films of Agarose and Lipids Display Altered Mechanical Properties. *Biophys. J.* **107,** 1609–1619 (2014).

46. Lira, R. B., Steinkühler, J., Knorr, R. L., Dimova, R. & Riske, K. A. Posing for a picture: vesicle immobilization in agarose gel. *Sci. Rep.* **6,** 25254 (2016).

47. Liu, Y. & Breukink, E. The Membrane Steps of Bacterial Cell Wall Synthesis as Antibiotic Targets. *Antibiotics* **5,** 28 (2016).

48. Lo, C. J., Leake, M. C. & Berry., R. M. Fluorescence measurement of intracellular sodium concentration in single Escherichia coli cells. *Biophys. J.* **90,** 357–365 (2006).

49. Lu, M., Radchenko, M., Symersky, J., Nie, R. & Guo, Y. Structural insights into H+-coupled multidrug extrusion by a MATE transporter. *Nat. Struct. Mol. Biol.* **20,** 1310–1317 (2013).

50. Massenburg, D. & Lentz, B. R. Poly(ethylene glycol)-induced fusion and rupture of dipalmitoylphosphatidylcholine large, unilamellar extruded vesicles. *Biochemistry* **32,** 9172–9180 (1993).

51. McIntyre, J. C. & Sleight, R. G. Fluorescence assay for phospholipid membrane asymmetry. *Biochemistry* **30,** 11819–11827 (1991).

52. McPhee, C. I., Zoriniants, G., Langbein, W. & Borri, P. Measuring the Lamellarity of Giant Lipid Vesicles with Differential Interference Contrast Microscopy. *Biophys. J.* **105,** 1414–1420 (2013).

53. Meeske, A. *et al.* SEDS proteins are a widespread family of bacterial cell wall polymerases. *Nature* **537,** 634–638 (2016).

54. Meurer, F., Do, H. T. & Held., G. Standard Gibbs energy of metabolic reactions: II. Glucose-6-phosphatase reaction and ATP hydrolysis. *Biophys. Chem.* **223,** 30–38 (2017).

55. Mishra, M. *et al.* Antibiotic Resistance Profile, Outer Membrane Proteins, Virulence Factors and Genome Sequence Analysis Reveal Clinical Isolates of Enterobacter Are Potential Pathogens Compared to Environmental Isolates. *Front. Cell Infect. Microbiol.* **10,** 54 (2020).

56. Mohammadi, T. *et al.* Identification of FtsW as a transporter of lipid-linked cell wall precursors across the membrane. *EMBO J.* **30,** 1425–1432 (2011).

57. Mohammadi, T. *et al.* Specificity of the transport of lipid II by FtsW in Escherichia coli. *Biol. Chem.* **289,** 14707–14718 (2014).

58. Morshed, A., Karawdeniya, B. I., Bandara, Y. M. N. D. Y., Kim, M. J. & Dutta, P. Mechanical characterization of vesicles and cells: A review. *Electrophoresis* **41,** 449–470 (2020).

59. Mott, J. E. *et al.* Resistance mapping and mode of action of a novel class of antibacterial anthranilic acids: evidence for disruption of cell wall biosynthesis. *J. Antimicrob. Chemother.* **62,** 720–729 (2008).

60. Mulligan, C., Leech, A. P., Kelly, D. J. & Thomas, G. The membrane proteins SiaQ and SiaM form an essential stoichiometric complex in the sialic acid tripartite ATP-independent periplasmic (TRAP) transporter SiaPQM (VC1777-1779) from Vibrio cholerae. *J. Biol. Chem.* **287,** 3598–3608 (2012).

61. Mulligan, C. *et al.* The substrate-binding protein imposes directionality on an electrochemical sodium gradient-driven TRAP transporter. *Proc. Natl. Acad. of Sci. U.S.A.* **106,** 1778–1783 (2009).

62. Nollert, P. Membrane protein crystallization in amphiphile phases: practical and theoretical considerations. *Prog. Biophys. Mol. Biol.* **88,** 339–357 (2005).

63. Oldham, M. I., Khare, D., Quiocho, F. A., Davidson, A. L. & Chen, J. Crystal structure of a catalytic intermediate of the maltose transporter. *Nature* **450,** 515–521 (2007).

64. Olson, F., Hunt, C., Szoka, F., Vail, W. & Papahadjopoulos, D. Preparation of liposomes of defined size distribution by extrusion through polycarbonate membranes. *Biochimica et Biophysica Acta (BBA) - Biomembranes* **557,** 9–23 (1979).

65. Omote, H., Hiasa, M., Matsumoto, T., Otsuka, M. & Moriyama, Y. The MATE proteins as fundamental transporters of metabolic and xenobiotic organic cations. *Trends in Pharmacological Sciences* **27,** 587–593 (2006).

66. Overington, J. P., Al-Lazikani, B. & Hopkins, A. L. How many drug targets are there? *Nature Reviews Drug Discovery* **5,** 993–996 (2006).

67. Parigoris, E. *et al.* Facile generation of giant unilamellar vesicles using polyacrylamide gels. *Scientific Reports* **10,** 4824 (2020).

68. Pautot, S., Frisken, B. & Weitz, D. A. Production of unilamellar vesicles using an inverted emulsion. *Langmuir* **19,** 2870–2879 (2003).

69. Peter, M. F. *et al.* Triggering Closure of a Sialic Acid TRAP Transporter Substrate Binding Protein through Binding of Natural or Artificial Substrates. *J. Mol. Biol.* **433,** 166756 (2021).

70. Peter, M. F. *et al.* Structural and mechanistic analysis of a tripartite ATP-independent periplasmic TRAP transporter. *Nat. Comm.* **13,** 2041–1723 (2022).

71. Peter, M. F. *et al.* Conformational coupling of the sialic acid TRAP transporter HiSiaQM with its substrate binding protein HiSiaP. *Nat. Commun.* **15,** 217 (2024).

72. Prestrelski, S. J., Tedeschi, N., Arakawa, T. & Carpenter, J. F. Dehydration-induced conformational transitions in proteins and their inhibition by stabilizers. *Biophys J.*. **65,** 661–671 (1993).

73. Preus, S., Sofie, L. N., Hildebrandt, L. L., Gudnason, D. & Birkedal, V. iSMS: single-molecule FRET microscopy software. *Nat. Methods* **12,** 593–594 (2015).

74. Rhoden, V. & Goldin, S. M. Formation of Unilamellar Lipid Vesicles of controllable dimensions by detergent dialysis. *Biochemistry* **18,** 4173–4176 (1979).

75. Rigaud, J.-L., Levy, D., Mosser, G. & Lambert, O. Detergent removal by non-polar polystyrene beads. *European Biophysics Journal* **27,** 305–319 (1998).

76. Rosa, L. T., Bianconi, M. E., Thomas, G. H. & Kelly, D. J. Tripartite ATP-Independent Periplasmic (TRAP) Transporters and Tripartite Tricarboxylate Transporters (TTT): From Uptake to Pathogenicity. *Front. Cell. Infect. Microbiol.* **8,** 33 (2018).

77. Rubino, F. A., Kumar, S., Ruiz, N., Walker, S. & Kahne, D. E. Membrane Potential Is Required for MurJ Function. *J. Am. Chem. Soc.* **140,** 4481–4484 (2018).

78. Ruiz, N. Bioinformatics identification of MurJ (MviN) as the peptidoglycan lipid II flippase in Escherichia coli. *Proc. Natl. Acad. Sci. U.S.A.* **105,** 15553–15557 (2008).

79. Ruiz, N. Lipid Flippases for Bacterial Peptidoglycan Biosynthesis. *Lipid Insights* **8s1,** 21–31 (2016).

80. Ruland, J. A. *et al.* Nuclear export of the pre-60S ribosomal subunit through single nuclear pores observed in real time. *Nat Commun.* **12,** 6211 (2021).

81. Sakuragi, T. & Nagata, S. Regulation of phospholipid distribution in the lipid bilayer by flippases and scramblases. *Nat. Rev. Mol. Cell Biol.* **24,** 576–596 (2023).

82. Sarkis, J. & Vié, V. Biomimetic Models to Investigate Membrane Biophysics Affecting Lipid–Protein Interaction. *Front. Bioeng. Biotechnol.* **8,** 270 (2020).

83. Schindelin, J. *et al.* Fiji: an open-source platform for biological-image analysis. *Nat. Methods* **9,** 676–682 (2012).

84. Schneberger, N. *et al.* Allosteric substrate release by a sialic acid TRAP transporter substrate binding protein. *Commun. Biol.* **7,** 1559 (2024).

85. Sham, L.-T. *et al.* MurJ is the flippase of lipid-linked precursors for peptidoglycan biogenesis. *Science* **345,** 220–222 (2014).

86. Silhavy, T. J., Kahne, D. & Walker, S. The Bacterial Cell Envelope. *Cold Spring Harb Perspect Biol.* **2,** a000414 (2010).

87. Sjodt, M. *et al.* Structural coordination of polymerization and crosslinking by a SEDS–bPBP peptidoglycan synthase complex. *Nat. Microbiol.* **5,** 813–820 (2020).

88. Stein, H., Spindler, S., Bonakdar, N., Wang, C. & Sabdoghar, V. Production of Isolated Giant Unilamellar Vesicles under High Salt Concentrations. *Front. Physiol.* **08,** DOI: 10.3389/fphys.2017.00063 (2017).

89. Stillwell, W. Membrane Transport. *An Introduction to Biological Membranes.,* 305–337 (2013).

90. Sudbrack, T. P., Archilha, N. L., Itri, R. & Riske, K. A. Observing the Solubilization of Lipid Bilayers by Detergents with Optical Microscopy of GUVs. *J. Phys. Chem. B* **115,** 269–277 (2011).

91. Taguchi, A. *et al.* FtsW is a peptidoglycan polymerase that is functional only in complex with its cognate penicillin-binding protein. *Nat. Microbiol.* **4,** 587–594 (2019).

92. Tanaka, Y. *et al.* Structural basis for the drug extrusion mechanism by a MATE multidrug transporter. *Nature* **496,** 247–251 (2013).

93. Tareste, D., Shen, J., Melia, T. J. & Rothman, J. E. SNAREpin/Munc18 promotes adhesion and fusion of large vesicles to giant membranes. *Proc. Natl. Acad. Sci. U.S.A.* **105,** 2380–2385 (2008).

94. Tiessen, A., Pérez-Rodriguez, P. & Delaye-Arredondo, L. J. Mathematical modeling and comparison of protein size distribution in different plant, animal, fungal and microbial species reveals a negative correlation between protein size and protein number, thus providing insight into the evolution of proteomes. *BMC Res. Notes.* **5,** 85 (2012).

95. Tinevez, J.-Y. *et al.* TrackMate: An open and extensible platform for single-particle tracking. *Methods* **115,** 80–90 (2017).

96. Tunuguntla, R. *et al.* Lipid Bilayer Composition Can Influence the Orientation of Proteorhodopsin in Artificial Membranes. *Biophys. J.* **105,** 1388–1396 (2013).

97. Valdez, M. A., Fernandez, E., Matsunaga, T., Erickson, R. P. & Trouard, T. P. Distribution and Diffusion of Macromolecule Delivery to the Brain via Focused Ultrasound using Magnetic Resonance and Multispectral Fluorescence Imaging. *Ultrasound Med. Biol.* **46,** 122–136 (2020).

98. Vermette, P., Meagher, L., Gagnon, E., Griesser, H. J. & Doillon, C. J. Immobilized liposome layers for drug delivery applications: inhibition of angiogenesis. *J. of Control. Release* **80,** 179–195 (2002).

99. Wallin, E. & vonHeijne, G. Genome-wide analysis of integral membrane proteins from eubacterial, archaean, and eukaryotic organisms. *Protein Sci.* **7,** 1029–1038 (1998).

100. Wolde-Kidan, A. *et al.* Particle Diffusivity and Free-Energy Profiles in Hydrogels from Time-Resolved Penetration Data. *Biophys. J.* **120,** 463–475 (2021).

101. Wolfe, A. J., Gugel, J. F., Chen, M. & Movileanu, L. Detergent Desorption of Membrane Proteins Exhibits Two Kinetic Phases. *J. Phys. Chem. Lett.* **9,** 1913–1919 (2018).

102. Yanagisawa, M., Iwamoto, M., Kato, A., Yoshikawa, K. & Oiki, S. Oriented Reconstitution of a Membrane Protein in a Giant Unilamellar Vesicle: Experimental Verification with the Potassium Channel KcsA. *J. Am. Chem. Soc.* **133,** 11774–11779 (2011).

103. Yang, N. J. & Hinner, M. J. Getting Across the Cell Membrane: An Overview for Small Molecules, Peptides, and Proteins. *Methods Mol Biol.* **1266,** 29–53 (2015).

104. Yin, H. & Flynn, A. D. Drugging Membrane Protein Interactions. *Annu. Rev. Biomed. Eng.* **18,** 51–76 (2016).

105. Zhang, Z., Yomo, D. & Gradinaru, C. Choosing the right fluorophore for single-molecule fluorescence studies in a lipid environment. *Biochimica et Biophysica Acta (BBA) - Biomembranes* **1859,** 1242–1253 (2017).

7 Appendix

(1) SDS PAGE of HiSiaQM-AF546

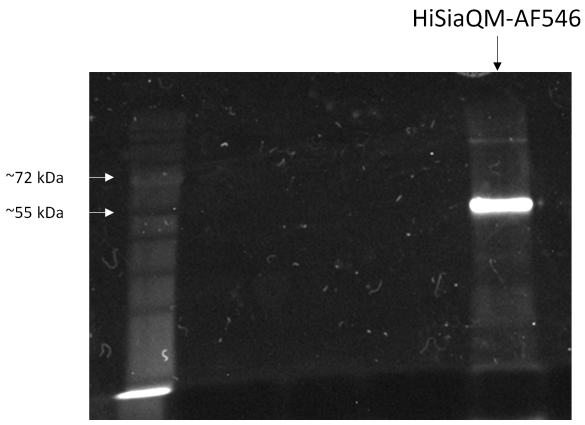


Figure 63: HiSiaQM-AF546. 12% SDS PAGE Gel, imaged under UV light. Page Ruler pre-stained ladder on the first lane, HiSiaQM-AF546 was added on the fifth lane.

(2) SDS PAGE of $\mathbf{Nb}_{HiSiaQM}$-AF647

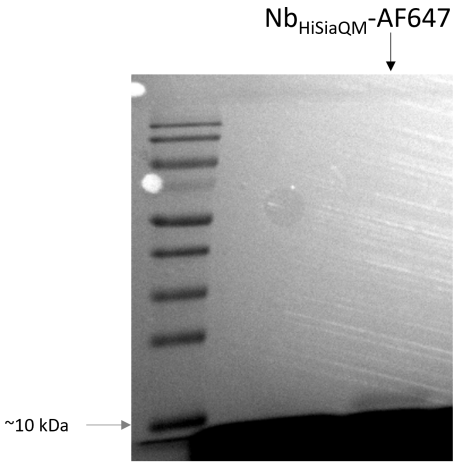


Figure 64: $\mathbf{Nb}_{HiSiaP}$-AF647. 12% SDS PAGE Gel, imaged under white light. Page Ruler pre-stained ladder on the first lane, Nb_{HiSiaP}-AF647 was added on the third lane.

(3) SDS PAGE Gel of MurJ-AF647

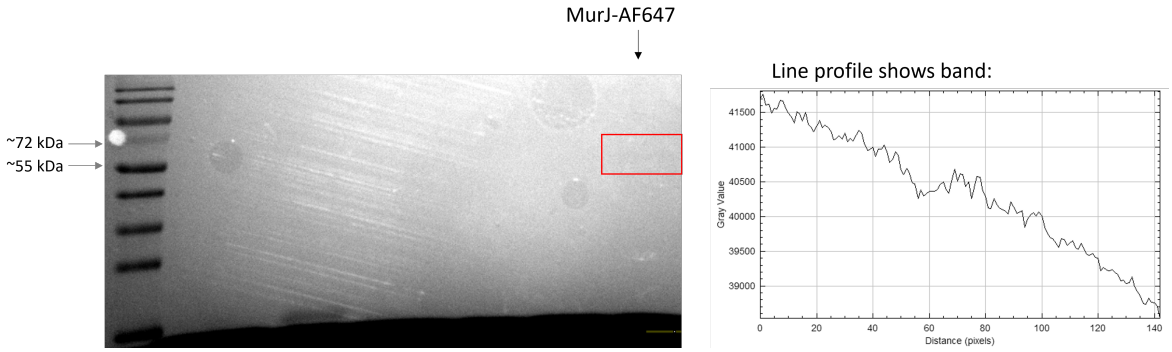


Figure 65: MurJ-AF647. 12% SDS PAGE Gel, imaged under white light. Page Ruler pre-stained ladder on the first lane, MurJ-AF647 was added on the seventh lane. Since the band was only very weak, a line profile vertically through a part of the lane indicates the band as a local minimum (on the right hand side).

(4) SDS PAGE Gel of FtSW-AF488 and RodA-AF488

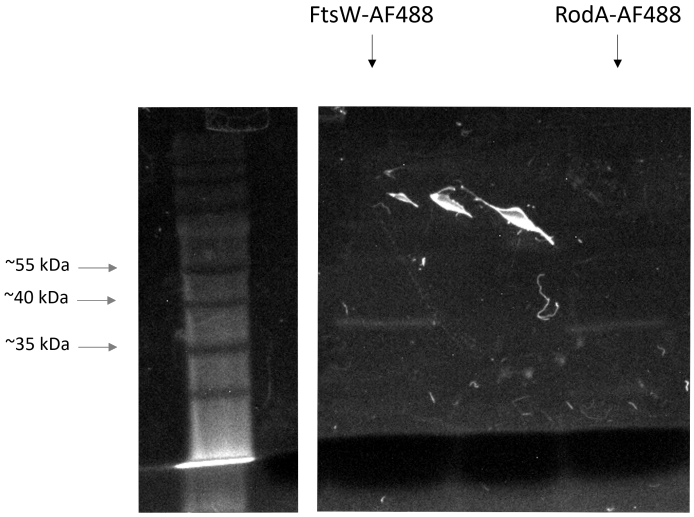


Figure 66: FtsW-AF488 and RodA-AF488. 12% SDS PAGE Gel, imaged under UV-light. Page Ruler pre-stained ladder on the first lane, FtsW-AF488 and RodA-AF488 were added as indicated.

(5) SDS PAGE Gel of HiSiaQM-NBD

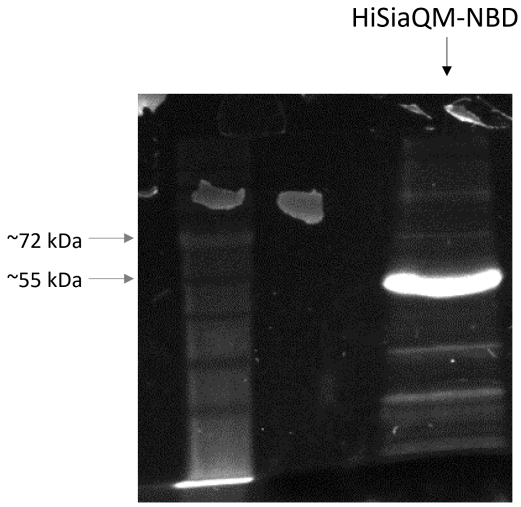


Figure 67: HiSiaQM-NBD. 12% SDS PAGE Gel, imaged under UV-light. Page Ruler pre-stained ladder on the first lane, HiSiaQM-NBD was added on the third lane.

(6) $Nb_{HiSiaQM}$ recognition of membrane-inserted HiSiaQM

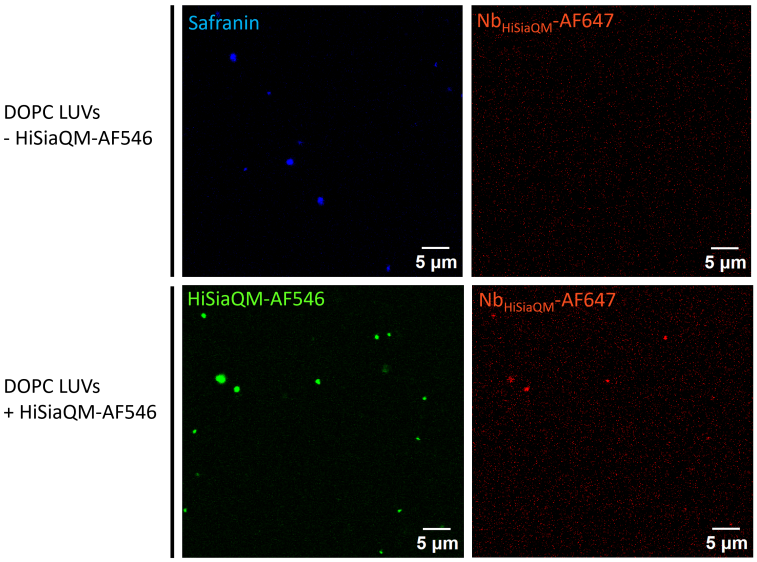


Figure 68: $Nb_{HiSiaQM}$ recognition of membrane-inserted HiSiaQM. The first row represents an agarose-embedded DOPC LUV sample with no HiSiaQM recostituted, instead the membrane-inserting dye safranin was applied. The second row shows a sample with HiSiaQM-AF546. While the first column shows either the channel of the safranin or the HiSiaQM fluorescence, the second channel shows the fluorescence intensity of a $Nb_{HiSiaQM}$-AF647, which was added to both samples.

(7) Correction factor determination for smFRET

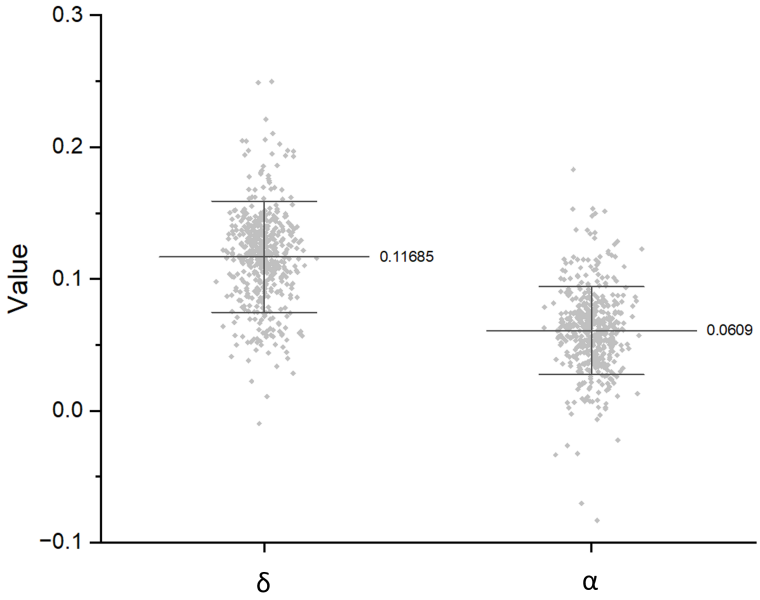


Figure 69: Correction factors for smFRET. Determination of the correction factors δ and α for iSMS, calculated via $\delta = \frac{A_D}{A_A}$ for acceptor-only samples and $\alpha = \frac{A_D}{D_D}$ for donor-only samples. For each correction factor 510 data points were measured. The mean value was chosen as value for the correction factor.

(8) Estimation of reconstituted HiSiaQM

To estimate the amount of protein that was reconstituted into the membrane, the GUV membrane fluorescence intensity was first measured against increasing concentrations of the fluorescent lipid NBD-PE (figure 70a-d) to later use this dependence to calculate the amount of HiSiaQM-NBD (SDS-PAGE in App. 5).

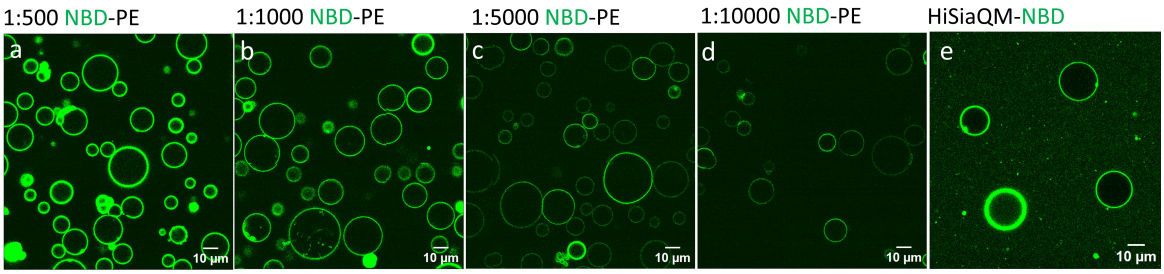


Figure 70: Membrane fluorescence intensity vs. NBD concentration. a-d: *E. coli* PL/POPC (3:1) GUVs with decreasing concentrations of NBD-PE. **e:** *E. coli* PL/POPC (3:1) GUVs containing HiSiaQM-NBD (protein:lipid 1:1000).

To measure the membrane fluorescence intensity as exactly as possible, a so called 'average radial profile' was measured via the Fiji PlugIn "Radial Profile Angle" from Paul Baggethun, 2002. In short, the PlugIn identified a GUV's center and measured several line profiles starting from the center with varying angles. The line profiles were

averaged and the maximum value of the average profile was chosen. This value is called the membrane fluorescence intensity in the following. A calibration curve, showing the dependence of the membrane fluorescence on the relative amount of fluorescent lipids, is shown in figure 71. A linear correlation was found. This relationship could then be used to estimate the amount of HiSiaQM-NBD from the measured membrane fluorescence (figure 70e).

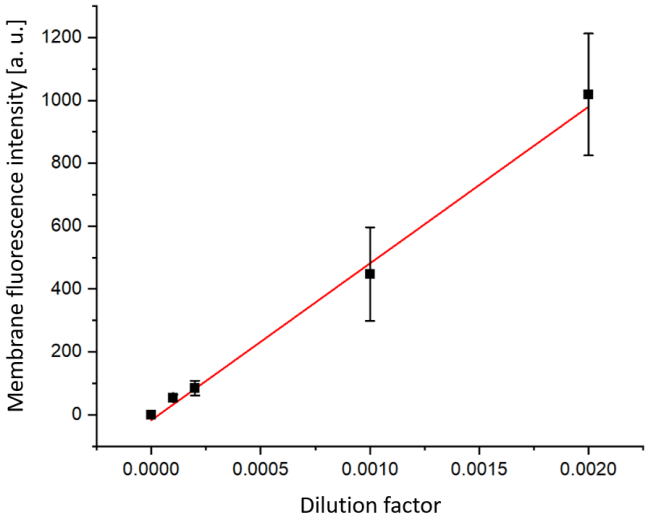


Figure 71: Calibration curve of membrane fluorescence intensity vs. NBD dilution. Background corrected membrane fluorescence intensity of *E. coli* PL/POPC/NBD-PE (3:1:x) GUVs in dependence of their relative NBD-PE amount. The data was fitted with a linear fit, shown in red.

The membrane fluorescence intensity of 50 GUVs after HiSiaQM-NBD (1:1000) reconstitution was determined to be 910 ± 520 a.u.. Insertion into the linear fit function resulted in a NBD:lipid factor of 1:540. Considering the degree of labeling of HiSiaQM-NBD of 4.1, which was measured via Nanodrop 2000c (Thermo Scientific, Schwerte), the average ratio of HiSiaQM-NBD to lipid was estimated to be about 1:2000. This suggests that approximately half of the added HiSiaQM proteins were inserted into the GUV membranes. However, it must be noted that a great heterogeneity in protein amount among GUVs was observed.

(9) Parameters of two-component Gaussian fit

	y_0	w_1	w_2	σ_1	σ_2	μ_1	μ_1
Intraprotein labeling	0	0.02	0.2	0.002	0.01	0.08	0.29
Intraprotein labeling + Neu5Ac	0	0.03	0.27	0.002	0.02	0.09	0.44
Interprotein labeling	0.002	0.03	0.1	0.006	0.01	0.07	0.19
Interprotein labeling + Neu5Ac	0	0.03	0.27	0.002	0.02	0.07	0.64

Table 8: Gaussian fit of smFRET histograms. Two-component Gaussian fit for smFRET sensor systems with and without Neu5Ac (figure 45).

(10) GUV diameter measurement

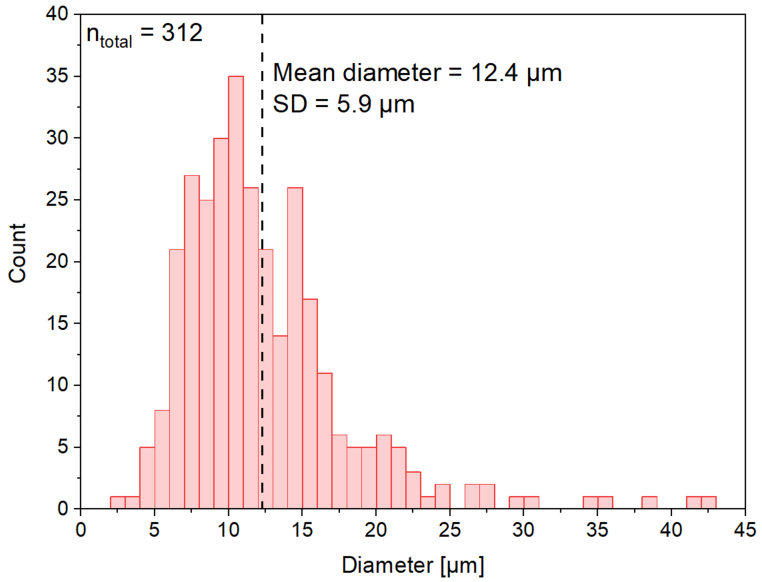


Figure 72: GUV diameter. GUV diameter was determined from Z-stack measurements of *E. coli* PL/POPC/TopFluorPC (3:1:0.01) GUVs. For each measured GUV, the equatorial plane was used for diameter measurement via Fiji/ImageJ [83].

List of Figures

1 Vesicle structure . . . 3
2 Vesicle formation methods . . . 4
3 Membrane protein reconstitution in GUVs . . . 6
4 Mechanisms of transporter proteins . . . 8
5 Cell wall biosynthesis . . . 9
6 Proposed model of MurJ flipping . . . 10
7 Proposed dual peptidoglycan synthesis pathway . . . 11
8 Structure of sialic acids . . . 12
9 Proposed import mechanism for HiSiaPQM . . . 13
10 Detergent-mediated swelling of proteo-GUVs . . . 18
11 GUV swelling on AA/BA substrate . . . 19
12 Membrane protein reconstitution in GUVs . . . 20
13 Reconstituted HiSiaQM is recognized by Nb . . . 20
14 Cargo encapsulation . . . 21
15 Membrane integrity . . . 22
16 NBD-quenching via sodium dithionite . . . 23
17 Lamellarity via radial profile analysis . . . 24
18 Calibration curve of safranin fluorescence . . . 25
19 Membrane potential in GUVs . . . 26
20 STED and confocal LUV images . . . 28
21 LUV immobilization . . . 29
22 Membrane protein reconstitution in LUVs . . . 30
23 Size measurement of LUVs via DLS . . . 30
24 LUV membrane Integrity . . . 31
25 Dithionite quenching of surface-immobilized LUVs . . . 32
26 Membrane potential establishment . . . 33
27 LUV-LUV fusion leading to lipid and lumen mixing . . . 34
28 Dual-color smFRET TIRF setup . . . 37
29 smFRET calibration using DNA samples . . . 39
30 Lipid II-NBD synthesis . . . 41
31 Time series of dithionite quenching of LUVs . . . 42
32 Flipping of lipid II-NBD . . . 43
33 Influence of MurJ inhibitors on flippase activity . . . 44
34 Protected lipid II-NBD fractions. . . . 45
35 TRAP-transporter mechanism. . . . 46
36 Neu5Ac detection by FRET via two labeling approaches . . . 46
37 Neu5Ac FRET sensor systems . . . 47

38 Affinity of VcSiaP for Neu5Ac 48
39 TRAP-transporter mechanism 48
40 HiSiaP-QM complex formation 49
41 HiSiaP-QM complex formation via TIRF microscopy 50
42 Interaction studies of HiSiaP-AF647 and surface-immobilized LUVs . . 51
43 TRAP-transporter import overview 52
44 Neu5Ac sensors in surface-immobilized LUVs 53
45 smFRET sensor systems recognize Neu5Ac 54
46 Poisson-distributed LUV occupancy 55
47 Donor- and acceptor-only ALEX smFRET 55
48 ALEX smFRET evaluation for artificial data set 56
49 Vesicle occupancy with Neu5Ac added before LUV formation 57
50 Neu5Ac import in LUVs, shows as heatmaps 58
51 Neu5Ac import in LUVs. 59
52 Channels of ensemble FRET measurement 60
53 Macro segmentation 60
54 Neu5Ac detection via ensemble FRET in GUVs 61
55 Mutant overview 62
56 End-point import success measurement 63
57 Time-resolved Neu5Ac import 64
58 Import progress. 66
59 Artificial vesicle with the established properties 69
60 Proposed MurJ cycle 71
61 Proposed TRAP transporter cycling model 80
62 Macro workflow 99
63 App. 1 108
64 App. 2 108
65 App. 3 109
66 App. 4 109
67 App. 5 110
68 App. 6 110
69 App. 7 111
70 App. 8.1 111
71 App. 8.2 112
72 App. 10 113

List of Tables

1 Spherical model systems 7
2 Comparison of different parameters in bacteria and GUVs 27
3 Used chemicals 83
4 Used instruments and optical devices 85
5 Used special laboratory consumables 86
6 Used software 86
7 Protein mutants 92
8 App. 9 113